

TWO-PHOTON POLYMERIZATION OF DEFECTS IN PHOTONIC CRYSTALS

BY

STEPHANIE PRUZINSKY

B.S., Rensselaer Polytechnic Institute, 2000

DISSERTATION

Submitted in partial fulfillment of the requirements
for the degree of Doctor of Philosophy in Materials Science and Engineering
in the Graduate College of the
University of Illinois at Urbana-Champaign, 2006

Urbana, Illinois

ABSTRACT

Three dimensional (3D) photonic bandgap (PBG) materials have been proposed as the basis of many devices (e.g. low-threshold lasers, low-loss waveguides, and on-chip circuitry), the majority of which rely on the incorporation of defects to provide functionality. While, self-assembled photonic crystals are the most widely explored fabrication route to 3D PBG materials, a critical limitation to their utility for PBG-based applications was the lack of an inherent method to controllably incorporate defect structures. We successfully demonstrated the use of two-photon polymerization (TPP) to generate such embedded features within colloidal crystals.

TPP is a high-resolution, 3D free-form fabrication technique that has been used to define a variety of structures, including microchannels, cantilevers, and photonic crystals. Here, TPP was adapted for use within colloidal crystals to embed pre-defined, 3D, high resolution features. A modulated beam rastering approach was employed and TPP response diagrams were developed to enable the reliable definition of TPP features. Also, preliminary work writing TPP features in 3D holographic photonic crystals was presented.

For applications requiring a complete PBG, it is necessary to convert colloidal photonic crystals to higher refractive index structures that exhibit complete PBGs. To this end, self-assembled photonic crystals with embedded TPP features were replicated in silicon. The TPP features and colloidal crystal served as a template for the final structure—a silicon-air inverse opal (which may exhibit a complete PBG) with embedded air defects. Embedded planar defects in silicon colloidal photonic crystals were optically characterized and high resolution embedded air defects in silicon-air inverse opals were demonstrated, representing a major step forward in providing a platform for the utility of colloidal photonic crystals for PBG-based applications.

ACKNOWLEDGEMENTS

The facilities and people that first attracted me to the University of Illinois at Urbana-Champaign on my graduate student recruiting visit, have far exceeded my initial expectations. This often exploratory research project would not have been possible without the amazing resources this campus has to offer.

In particular, I would like to thank my advisor, Professor Paul Braun, for his enthusiasm and encouragement throughout graduate school. Being part of the early development of a research group has been a valuable experience. I am grateful for the insight and advice Paul has shared with me and thank him for valuing my opinion. I especially appreciate the balance Paul found between advising me and allowing me to define my own path and develop as an independent researcher.

I would like to thank Professor Pierre Wiltzius for his valuable insight. His genuine enthusiasm and curiosity for science have made group meetings and collaborations enjoyable. I would like to thank Professor Jennifer Lewis, for her continued support and encouragement. She has been a wonderful mentor and resource throughout graduate school. Also, I would like to thank Professors John Rogers and Harley Johnson for their useful observations and suggestions.

I am grateful to Dr. Alex (Yun-Ju) Lee for making research an adventure—it was always exciting working with Alex. I am also thankful for the expertise of Dr. Florencio García-Santamaría, which greatly enhanced the content of Chapters 3 and 4. I appreciate the organic chemistry expertise of Dr. Huilin Tu, Dr. Alejandro Wolosiuk, and Robert Shimmin. It has also been a pleasure working with Christy (Ying-Chieh) Chen, Vinayak Ramanan, Erik Nelson, Wendy Chan, and the rest of the Braun and Wiltzius research groups.

I am especially grateful to Karl Garsha for his advice and assistance with confocal microscopy. I also appreciate the valuable expertise of the rest of the staff in the Imaging Technology Group, Microfabrication Facility, and Center for Microanalysis of Materials.

I gratefully acknowledge those that first exposed me to scientific research: Professor Minoru Tomozawa for making me aware of the National Science Foundation's Research Experience for Undergraduates program; Professor Thomas Russell for giving me the opportunity to work in his research group; and Dr. Elbert Huang for the mentoring he provided during that research experience. I am also very grateful for the inspiration, advice and encouragement during my undergraduate from Professor Linda Schadler.

I would especially like to thank my family for their continued support, encouragement, and assistance throughout the years. I am grateful to my best friend and husband, James Rinne, for his inquisitive nature, work ethic, and valuable perspective, both in research and in life. His friendship has made the last several years of graduate school truly memorable.

This thesis is based in part upon work supported by the U.S. Department of Energy, Division of Materials Sciences grant number DEFG02-91ER45439, through the Frederick Seitz Materials Research Laboratory at the University of Illinois at Urbana-Champaign, the U. S. Army Research Office grant number DAAD19-03-1-0227, and the National Science Foundation through a graduate fellowship and through grant number 00-71645. Research for this publication was carried out in the Center for Microanalysis of Materials, University of Illinois at Urbana-Champaign, which is partially supported by the U.S. Department of Energy under grant DEFG02-91-ER45439, and in the Imaging Technology Group at the Beckman Institute, University of Illinois at Urbana-Champaign. Also, I gratefully acknowledge Dr. L.-S. Tan (U.S. Air Force Research Laboratory) for providing the two-photon sensitive dyes used.

TABLE OF CONTENTS

LIST OF ABBREVIATIONS.....	viii
CHAPTER 1. INTRODUCTION	1
1.1 Opals	1
1.2 Photonic Crystals	2
1.3 Bragg Diffraction	3
1.4 Spectroscopy	4
1.4.1 <i>Simulated Spectroscopy</i>	6
1.4.2 <i>Experimental Spectroscopy</i>	7
1.4.3 <i>Impact of NA of Spectroscopy</i>	8
1.5 Photonic Bandgap Materials	11
1.6 Fabrication of 3D PBG Materials	13
1.7 PBG Applications	15
1.8 Defects in 2D Photonic Crystals	16
1.9 Defects in 3D Photonic Crystals	18
1.10 Defects in Colloidal Photonic Crystals	19
1.10.1 <i>Substitutional Doping</i>	21
1.10.2 <i>2D Embedded Defects via Multi-Step Procedures</i>	22
1.10.3 <i>3D Embedded Defects via Two-Photon Polymerization</i>	28
1.11 References	30
CHAPTER 2. TWO-PHOTON POLYMERIZATION	36
2.1 Motivation.....	36
2.2 Introduction to TPP.....	36
2.3 Point-by-Point Exposure.....	40
2.4 Modulated Beam Rastering.....	42
2.5 TPP Response Diagrams.....	47
2.5.1 <i>TPP Within and Outside of a Colloidal Crystal</i>	49
2.5.2 <i>Initiator Efficiency Comparison</i>	51
2.6 Microscopy of TPP Features.....	52
2.7 Spectroscopy from TPP Features.....	56
2.8 Conclusions.....	58
2.9 Experimental.....	59
2.9.1 <i>Confocal Instrumentation</i>	59
2.9.2 <i>Power Measurements</i>	60
2.9.3 <i>Materials</i>	61
2.9.4 <i>Colloidal Crystal Preparation</i>	62
2.9.5 <i>Microscopy and Spectroscopy of TPP Features</i>	64
2.10 References.....	65

CHAPTER 3. HIGH INDEX REPLICATION	69
3.1 Motivation.....	69
3.2 Calcination of Colloids	71
3.3 Colloidal Crystallization	72
3.4 Atomic Layer Deposition of Alumina	74
3.5 Two-Photon Polymerization	77
3.6 Chemical Vapor Deposition of Silicon	79
3.7 Reactive Ion Etching.....	81
3.8 Removal of Polymer (Optional).....	84
3.9 Wet Etch of Silica and Alumina	86
3.10 Conclusions.....	90
3.11 Experimental.....	91
3.12 References.....	91
CHAPTER 4. CHARACTERIZATION OF EMBEDDED DEFECTS	93
4.1 Microscopy of Defects in Silicon Inverse Opals	93
4.2 Spectroscopy from Embedded Planar Defects.....	95
4.3 IR Transmission Microscopy through Defects	99
4.4 Conclusions.....	100
4.5 References.....	101
CHAPTER 5. TPP IN HOLOGRAPHIC PHOTONIC CRYSTALS	102
5.1 Introduction to Holography.....	102
5.2 Holographic Photonic Crystals	103
5.3 Phase Mask Holographic Lithography.....	106
5.4 Defects in Holographic Photonic Crystals.....	107
5.5 Conclusions and Outlook.....	110
5.6 Experimental	110
5.7 References.....	110
CHAPTER 6. CONCLUSIONS	112
APPENDIX A. BRAGG DIFFRACTION	114
APPENDIX B. POLYMERIZATION THRESHOLD	116
AUTHOR’S BIOGRAPHY	120

LIST OF ABBREVIATIONS

2D	two-dimensional
3D	three-dimensional
AF-350	(tris[4-(7-benzothiazol-2-yl-9,9-diethylfluoren-2-yl)phenyl]amine)
ALD	atomic layer deposition
cPBG	complete photonic bandgap
CVD	chemical vapor deposition
e-beam	electron beam
EOM	electro-optic modulator
FCC	face-centered cubic
FIB	focused ion beam
FDTD	finite difference time domain
HF	hydrofluoric acid
IR	infrared
KKR	Korringa-Kohn-Rostoker
LSCM	laser scanning confocal microscope
NA	numerical aperture
PBG	photonic bandgap
PDMS	polydimethylsiloxane
RIE	reactive ion etching
ROI	region of interest
SEM	scanning electron microscope
SWA	scalar wave approximation
TGA	thermogravimetric analysis
TMM	transfer matrix method
TMPTA	trimethylolpropane triacrylate
TPE	two-photon excitation
TPP	two-photon polymerization

CHAPTER 1

INTRODUCTION

1.1 Opals

The iridescence of opals has mystified people for ages (Fig. 1.1a). Ancient Arabs believed that the gods bestowed opals with the brilliance of lightning and fire and then dropped them from the heavens as gifts.[1] More practical, early explanations attributed the opal's striking coloration to a myriad of internal cracks or to oil trapped within the stone.[1] It was not until the mid-1960's that it became clear the origin of their color was diffraction-based. In 1964, the first electron micrograph taken from a precious opal was published, revealing that opals consist of periodic arrays of silica microspheres, approximately 150-400 nm in diameter (Fig. 1.1b).[2] This provided the final proof that the iridescence of opals is attributable to diffraction, rather than absorption as for all other precious gems.[1]

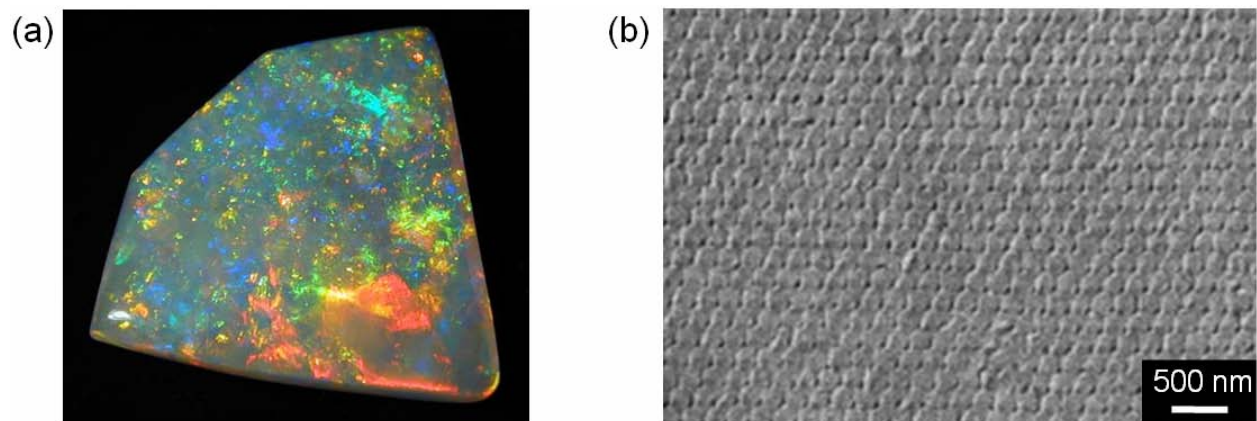


Figure 1.1 (a) Photograph of an opal gemstone[3 2006] and (b) the first published electron micrograph from a precious opal.[2]

Since then, the interest in opals has transitioned from a fascination over their striking color and their value as a gemstone, to the utilization of their optical diffraction in photonics

applications. This has been facilitated by the demonstration that synthetic opals, or colloidal crystals, can be self-assembled in the lab.[4] Their ease of fabrication and ability to modulate light has led to a host of applications within the emerging field of photonic crystals.

1.2 Photonic Crystals

Photonic crystals are materials that possess periodicity in their dielectric constant or refractive index (Fig. 1.2a).[5] Similar to an atomic crystal, a photonic crystal is composed of a periodic array of scatterers, which give rise to an interference pattern specific to the underlying microstructure (Fig. 1.2b). The characteristic length scales of photonic crystals are on the order of optical wavelengths—several thousand times larger than those of their atomic crystal counterparts. As such, photonic crystals diffract photons of much longer wavelengths, for example in the visible or infrared (Fig. 1.2b).

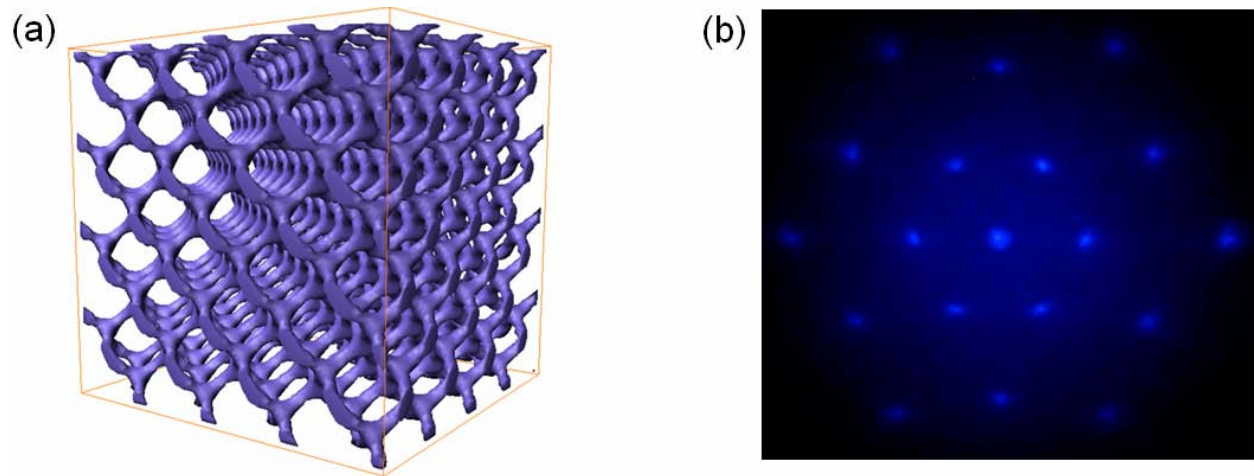


Figure 1.2 (a) Example of a three-dimensionally periodic, diamond-like photonic crystal. Image courtesy of James W. Rinne. (b) Diffraction pattern collected with an ultraviolet laser (351 nm) from a face-centered cubic array of polystyrene microspheres, approximately 1 μm in diameter. Photo courtesy of Dr. Florencio García Santamaría.

The diffraction wavelength and strength depend, in part, on the microdomain geometry, filling fraction, and periodicity of the structure. However, it is typically the refractive index contrast between the periodic domains that is used to place a rough classification on the modulation strength of a structure. This is convenient as certain fabrication procedures and theoretical approximations are only appropriate for low index contrast photonic crystals, while high index contrast photonic crystals have their own unique set of characteristics, fabrication requirements, and applications. It should be noted that there is no accepted rigorous or sharp distinction to define what a low or high index contrast photonic crystal is, though the distinction is useful and often made, nonetheless.

1.3 Bragg Diffraction

For low index contrast photonic crystals, diffraction can often be described by Bragg's law,[6] originally applied to atomic crystals. Due to the non-unity refractive index of materials at optical wavelengths, Bragg's law is often re-written as (Fig. 1.3, Appendix A)

$$m\lambda_B = 2d_{hkl} \left(n_{eff}^2 - \sin^2 \varphi \right)^{1/2} \quad (1.1)$$

where m is the diffracted order, λ_B is the wavelength of light in free space that is diffracted, d_{hkl} is the spacing between the planes giving rise to the diffraction, φ is the angle of the incident light with respect to the sample normal, and n_{eff} is the effective refractive index of the photonic crystal, often expressed as the square root of the average dielectric constant

$$n_{eff} = \left[\sum_i \left(n_i^2 \Phi_i \right) \right]^{1/2} \quad (1.2)$$

where n_i and Φ_i are the refractive index and volume fraction for each component, i , of the photonic crystal, respectively.

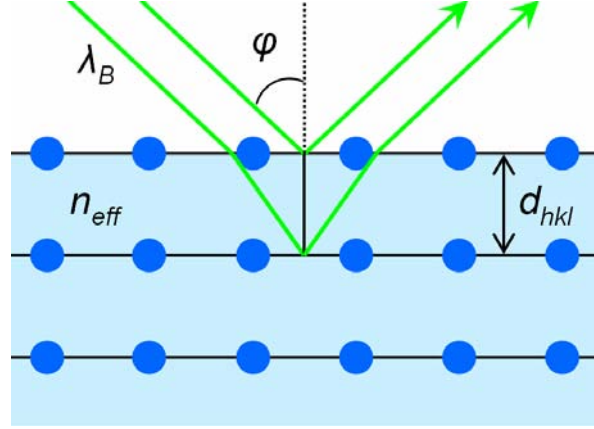


Figure 1.3 Schematic of Bragg diffraction for low index contrast photonic crystals.

The optical properties of synthetic opals, or colloidal crystals, have been widely studied and it is often found that the modified Bragg equation agrees well with experimentally measured diffraction results.[6] This equation often appears in its simplified form for colloidal crystals,

$$\lambda_B = \frac{2\sqrt{6}}{3} n_{eff} D \quad (1.3)$$

where first order diffraction is assumed and it is taken that $d_{hkl} = d_{111}$ and $\varphi = 0$. This is valid as colloidal crystals typically form with their close-packed or (111) planes parallel to the substrate and most experiments are normal incidence measurements. Also for convenience, d_{111} is often expressed in terms of the colloid diameter, D , where $d_{111} = \sqrt{6}/3 D$.

1.4 Spectroscopy

Normal incidence spectroscopy is often used to interrogate the optical properties of photonic crystals. A peak in reflection and corresponding dip in transmission is typically observed at the diffraction wavelength (Fig. 1.4a). This reflectance peak is flanked by fringes, arising from interference between the top and bottom interfaces of the photonic crystal.

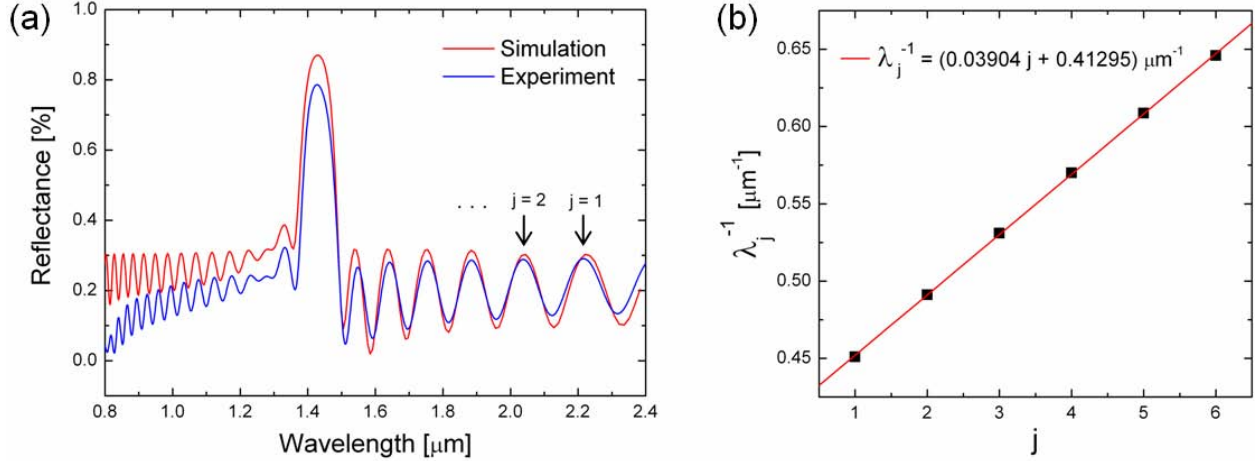


Figure 1.4 (a) Simulated (red) and experimental (blue) spectra from a silica colloidal crystal (particle diameter ~ 650 nm).[7] Simulated spectrum (red) was calculated using an available layered KKR package.[8,9] (b) Interference fringe calculation for experimental spectra in part a. The thickness calculated from the slope is $9.369 \mu\text{m}$, corresponding to a crystal ~ 18 layers thick, close to the 17 layers counted from this vertically deposited sample. Data from Dr. F. García-Santamaría.

The spacing between these fringes can be used to determine the thickness of a photonic crystal, t . [10] To do so, typically the reflectance maxima of the interference fringes are assigned an integer index, j , starting at the highest wavelength fringe ($j=1$), and proceeding to consecutive peaks in descending wavelength order ($j=2,3,\dots$) (Fig. 1.4a). Then, the reciprocal of the wavelength of the interference fringes reflectance maxima are plotted versus their indices (Fig. 1.4b). This plot is then fit to the first order, linear equation

$$\lambda_j^{-1} = \left(\frac{1}{2n_{\text{eff}}t} \right) j + b \quad (1.4)$$

where it is assumed that n_{eff} is lower than the index of the substrate.[11] In fitting this equation, the y-intercept, b , is obtained as well as the slope, $1/(2n_{\text{eff}}t)$, from which the photonic crystal thickness, t , can be extracted. The number of layers of a photonic crystal is simply t/d_{hkl} . The

thickness calculated from the interference fringes is typically in close agreement with that measured in a cross-sectional scanning electron micrograph (SEM) or by counting the number of layers on vertically deposited samples.[10] For thick photonic crystals, the spacing of the fringes may be smaller than the spectrometer resolution, in which case there is a flat background on either side of the reflectance peak.

1.4.1 Simulated Spectroscopy

Simulated reflection and transmission spectra can be calculated with a number of methods including, for example, the scalar wave approximation (SWA),[12,13] layered-Korringa-Kohn-Rostoker (KKR) approach,[9] transfer matrix method (TMM),[14,15] or finite difference time domain (FDTD)[16,17] technique. These methods can account for the finite number of layers in a photonic crystal and often substrate effects. Further, several computational packages have been developed and shared, making simulations more accessible to experimentalists and facilitating comparison between theory and experiment.[8,13,18-20]

Of the aforementioned methods to calculate spectra, SWA is the most basic, limited in that it neglects the vectorial nature of electromagnetic fields and only considers the diffraction response in one specific direction.[12] For example, in SWA a three-dimensionally periodic photonic crystal is modeled as a one-dimensional dielectric stack in order to quickly solve for the diffraction response. Despite this gross approximation, SWA is appealing as a fast, easy method to calculate spectra with reasonable accuracy from simple, low index contrast samples.[13]

The layered KKR technique accounts for the full vectorial nature of the electromagnetic fields, however this approach expands the fields via a finite number of spherical harmonics.[9] This affords good convergence for low-index contrast, non-interpenetrating arrays of spherical

scatterers, for example closepacked colloidal photonic crystals, where simulated spectroscopy agrees very well with experiment (Fig. 1.4a).[8,9]

TMM[14,15] and FDTD[16,17] are real space, finite difference approaches where either Maxwell's equations or the wave equation are discretized in the frequency or time domains, respectively. In FDTD, for example, the propagation of light within a photonic crystal is solved at all points in space for discrete time steps. Here, either the electric or magnetic field is calculated for a particular time step, and that is used to determine the other field for the subsequent time step. In a step-by-step fashion, the propagation of light through photonic crystals can be visualized and quantified.[16,17] Of the techniques discussed, TMM and FDTD are the most flexible and robust, able to accommodate high index contrast photonic crystals with or without engineered defects.

1.4.2 *Experimental Spectroscopy*

It is often advantageous to collect diffraction spectra from small sampling regions of a photonic crystal, which can be conveniently accomplished by coupling a reflectance optical microscope to a spectrometer (Fig. 1.5a). Such a microspectrometer enables collection spot sizes on the order of several to tens of microns, enabling for example, studies from single-crystalline domains in colloidal photonic crystals[21,22] and colloidal crystal templated hydrogels.[23-26] Since the incident light is focused onto the sample, the photonic crystal is probed with a cone of light with a nonzero numerical aperture, NA , defined as

$$NA = \sin \varphi_{\max} \quad (1.5)$$

where φ_{\max} is the maximum half-angle of the cone of light (Fig. 1.5a). It is evident from the Bragg equation (1.1), that the angle of the incident light directly impacts the diffraction

wavelength (Fig. 1.5b). Therefore, probing the sample with a cone of light ($NA>0$), as is typically done experimentally, should elicit a different diffraction response than if only probed at normal incidence ($\varphi=0$), which is normally the case for theoretical spectra.

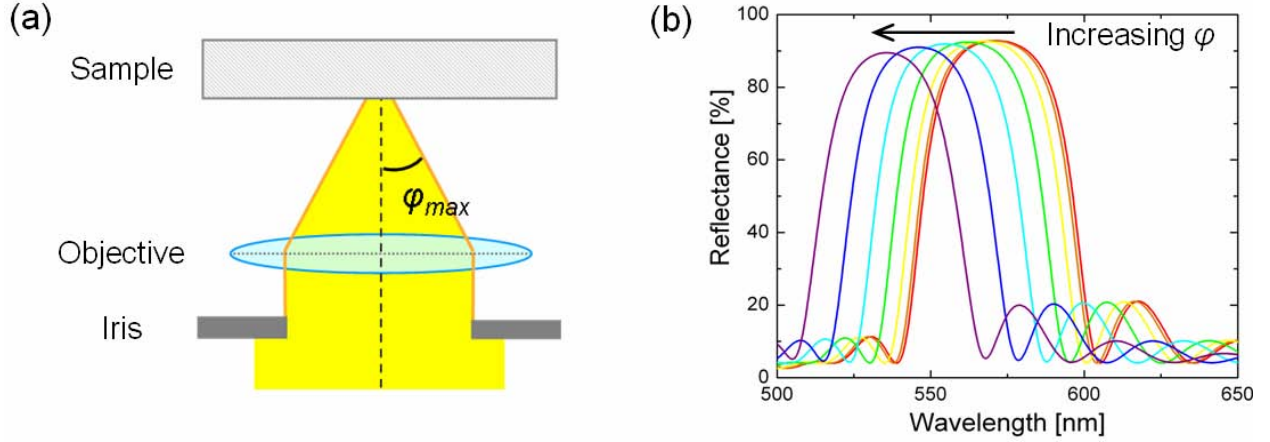


Figure 1.5 (a) Schematic illustrating the cone of light used to experimentally collect spectroscopy. (b) Spectroscopy simulated via layered KKR for a colloidal crystal, self-assembled from polystyrene microspheres, approximately 244 nm in diameter. Spectra are calculated for incident angles, φ , from 0 to 30°, at 5° increments, for $NA=0$. [27]

1.4.3 Impact of NA on Spectroscopy

Significant components of this section were published as Y.-J. Lee, S. A Pruzinsky, P. V. Braun, “Diffraction Response of Colloidal Crystals: Effect of Numerical Aperture” *Optics Letters* **2005**, *30*, 153-155.

The validity of comparing theoretical spectra, typically calculated for $\varphi=0$, with experimental results collected using a non-zero NA will be examined.[27] This was accomplished via a combined experimental and theoretical study of the impact of NA on spectroscopy from a low index contrast photonic crystal.[27] Here, the model system was a polystyrene colloidal crystal. Spectra were experimentally collected using a microspectrometer,

where the NA could be specified by adjusting a calibrated iris diaphragm mounted below the objective (Fig. 1.5a). To obtain simulated spectra that effectively represent a cone of light, it was necessary to first compute the spectra for individual angles within the cone ($0 \leq \varphi \leq \varphi_{max}$) and then weight those appropriately. The weighting scheme, determined experimentally, was to multiply the spectra for each φ up to φ_{max} by their normalized solid angle, and then sum them to give an effective spectrum for a particular NA . The resulting theoretical reflectance spectra (Fig. 1.6a) exhibited qualitatively similar peak shapes and NA dependence to the experimentally collected data (Fig. 1.6b).

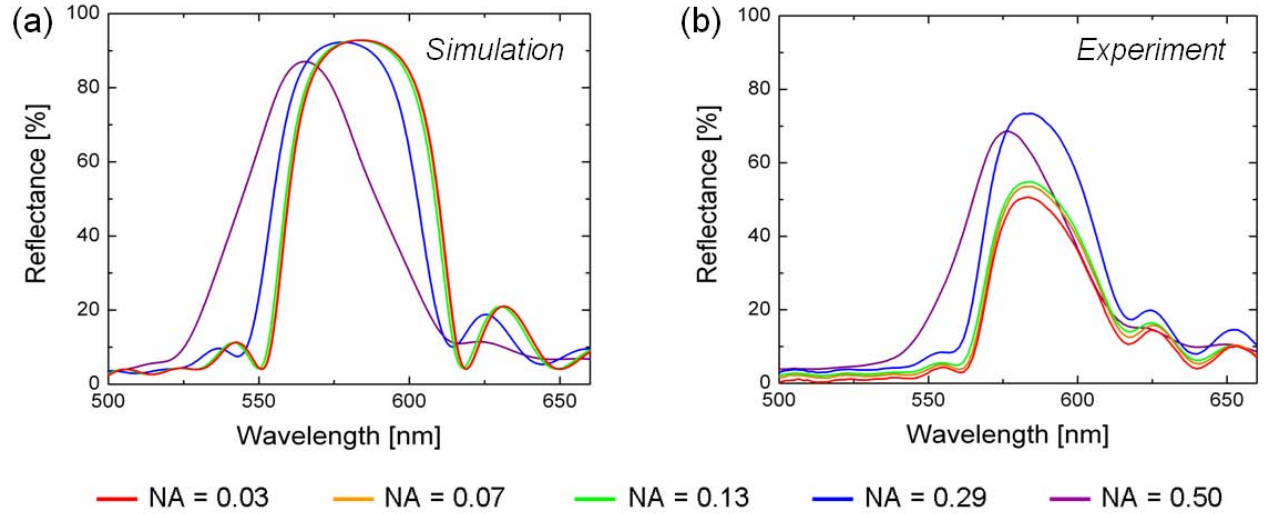


Figure 1.6 (a) Simulated and (b) experimentally collected spectra as a function of NA from a polystyrene colloidal crystal (colloid diameter approximately 244 nm).[27] Spectra were simulated using a layered KKR technique.[8,9]

To further enable the comparison between the experimental and theoretical results, the diffraction peak parameters were extracted from the spectra and plotted as a function of NA (Fig. 1.7). There is good qualitative agreement in the general shape of the trend for both the diffraction wavelength and normalized full width at half maximum versus NA for experiment and theory.

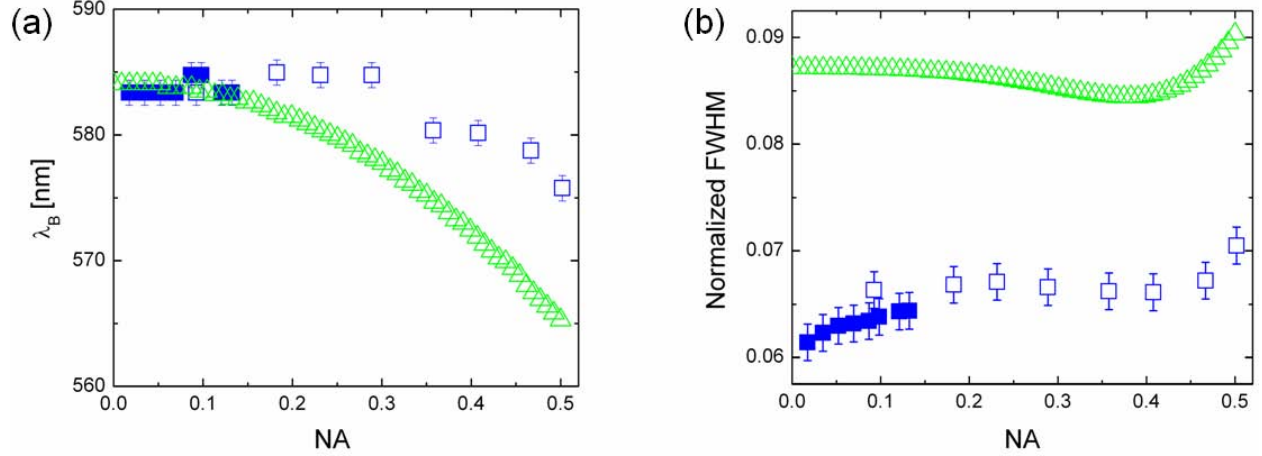


Figure 1.7 (a) Diffraction wavelength and (b) normalized full width half maximum as a function of NA for spectra calculated via KKR (green triangles) or experimentally collected (blue squares—open and closed denote different objectives).

The quantitative discrepancies between the experimental and theoretical peak parameters may be attributed to factors such as defects in the colloidal crystal, drying cracks, and limitations in the computational method or experimental collection. Theoretical methods like KKR assume perfect crystalline order, while real samples fabricated via self-assembly contain point and line defects, stacking faults, and drying cracks. Further, though the simulations capture the qualitative experimental trends rather well, it is possible that the approximation in KKR of a photonic crystal as a dielectric stack with spherical scattering[9] prevents quantitative agreement. Finally, the disorder in self-assembled photonic crystals has recently been reported to cause diffracted light to propagate in a range of angles around the expected direction of specular reflection.[28] Since our illumination and collection NA are the same, some of the reflected light may not be collected, which could be another possible reason for the observed quantitative discrepancies.

In any case, the good qualitative agreement between theoretical and experimental trends as well as the relative insensitivity of the Bragg diffraction response for low NA , suggests that it

may be acceptable to compare spectroscopy collected with low NA to normal incidence calculations for low index contrast photonic crystals. As such, microspectroscopy is an attractive technique that affords high spatial resolution and a good signal-to-noise ratio for the characterization of low index contrast photonic crystals.

1.5 Photonic Bandgap Materials

As the index contrast of photonic crystals increases, it becomes less valid to approximate these structures as periodic scatterers in media with homogenous refractive indices. Instead, it becomes necessary to accurately account for the spatial distribution of the dielectric constant, $\epsilon(\mathbf{r})$. Approximations, like Bragg's law, are no longer valid and a full vectorial solution of Maxwell equations is needed to obtain the dispersion relation in a high index contrast photonic crystal

$$\begin{aligned}
\nabla \cdot \mathbf{H}(\mathbf{r}, t) &= 0 \\
\nabla \cdot \epsilon(\mathbf{r}) \mathbf{E}(\mathbf{r}, t) &= 0 \\
\nabla \times \mathbf{E}(\mathbf{r}, t) + \frac{1}{c} \frac{\partial \mathbf{H}(\mathbf{r}, t)}{\partial t} &= 0 \\
\nabla \times \mathbf{H}(\mathbf{r}, t) - \frac{\epsilon(\mathbf{r})}{c} \frac{\partial \mathbf{E}(\mathbf{r}, t)}{\partial t} &= 0
\end{aligned} \tag{1.6}$$

where linear, lossless materials are assumed. Here, respectively, \mathbf{E} and \mathbf{H} are the macroscopic electric and magnetic fields, \mathbf{r} and t account for the positional and time-dependence of the fields, and c is the speed of light in vacuum.

Often for photonic crystals, the dispersion relation is plotted for a path along the irreducible Brillouin zone and this plot is referred to as a photonic band diagram (Fig. 1.8a). The bands represent modes or states for which light can exist within the material. Photonic crystals possessing appropriate domain geometries, filling fractions, and dielectric contrast may exhibit a

photonic bandgap (PBG). A PBG is a range of frequencies which cannot exist or propagate in the material as the density of states for these frequencies is zero (Fig. 1.8b). This concept was first proposed in 1975 by Bykov,[29] but remained relatively unknown until the seminal work by Yablonovitch[30] and John.[31] In a rough analogy to semiconductors, which possess an electronic band gap, a PBG material prohibits the propagation of photons with energies in the PBG.

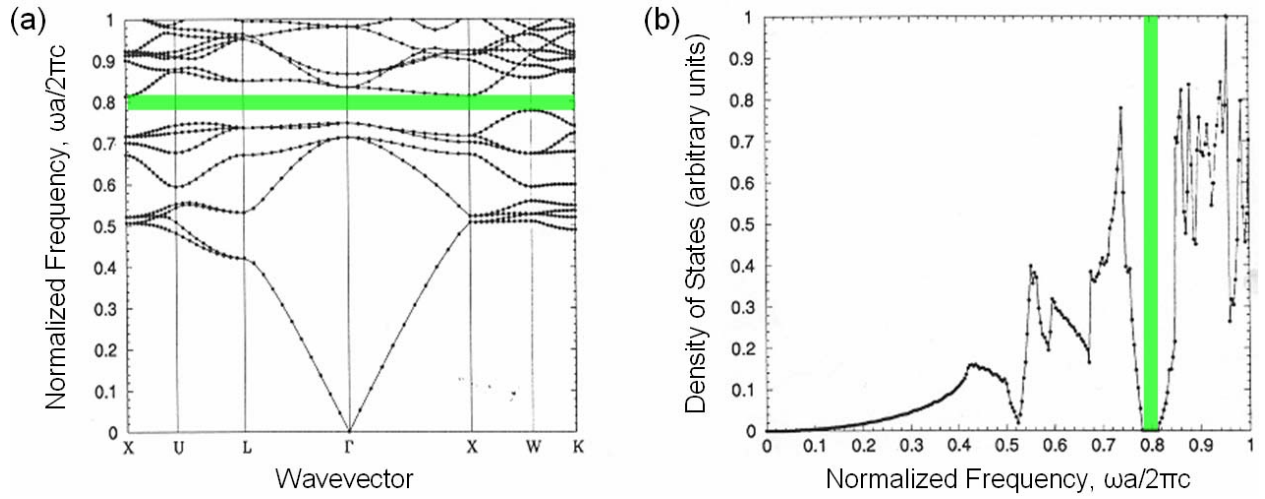


Figure 1.8 (a) Photonic band diagram and (b) plot of the density of states for a close-packed, face-centered cubic array of air spheres in silicon ($\epsilon=12$). Green shading highlights the complete PBG.[32]

Typically, photonic crystals and PBG materials are classified according to the dimensionality of their periodicity, since this determines the dimensionality of the PBG they can possess (Fig. 1.9). While the fabrication and modeling of one and two dimensional (2D) photonic crystals is much simpler, to rigorously prevent the propagation of bandgap frequencies in all directions, a three-dimensional (3D) photonic crystal with an omnidirectional, or complete (cPBG) is required.

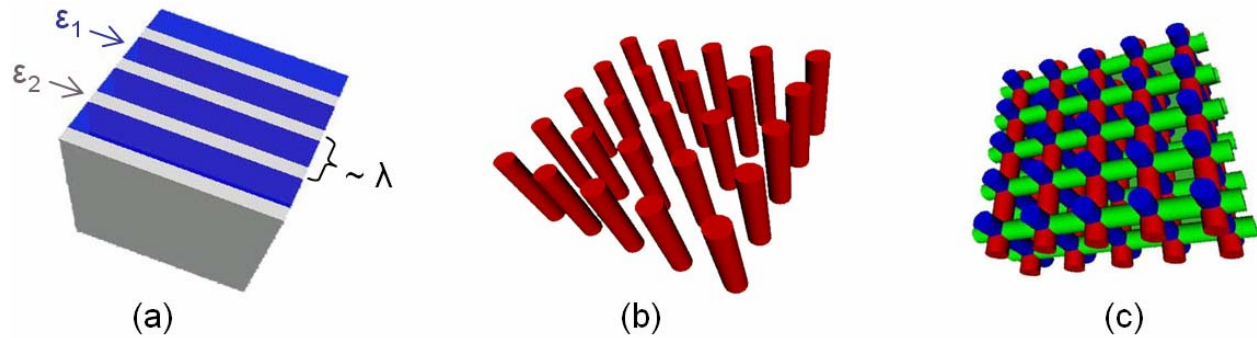


Figure 1.9 Schematic examples (a) one, (b) two, and (c) 3D photonic crystals. Figure reproduced with modifications.[33]

1.6 Fabrication of 3D PBG Materials

Significant components of sections 1.6-1.10 were published as P. V. Braun, S. A. Pruzinsky-Rinne, F. García-Santamaría “Introducing Defects in 3D Photonic Crystals: State of the Art” *Advanced Materials* **2006**, *In Press*.

cPBG materials have been fabricated and well characterized for operation at microwave and radio frequencies, however, operation in the visible and infrared (IR), requires the characteristic length scales of these structures to be scaled down by several orders of magnitude, necessitating 3D fabrication techniques capable of defining structures with submicron to micron scale periodicity and nanometer scale resolution. Additionally, cPBG structures must be fabricated from optically transparent materials with a high dielectric constant. In the optical regime, there is a limited set of materials satisfying these conditions, largely ruling out organic and metallic materials, most oxides, and many semiconductor-based structures. Because of the materials restrictions and stringent 3D fabrication requirements, there is a small, but growing, number of PBG materials that have been constructed in the visible or IR. Techniques employed in the fabrication of 3D photonic crystals include conventional lithography (Fig. 1.10a),[34,35]

self-assembly (Fig. 1.10b),[4] direct writing (Fig. 1.10c),[36] holographic lithography (Fig. 1.10d),[37] glancing angle deposition,[38] electrochemical etching,[39] and micromanipulation.[40] A comprehensive review on PBG fabrication methods can be found in reference [5]. Development of efficient, practical techniques amenable to the fabrication of 3D PBG materials operating in the visible to IR remains a vibrant area of research, with new approaches regularly introduced in the literature.

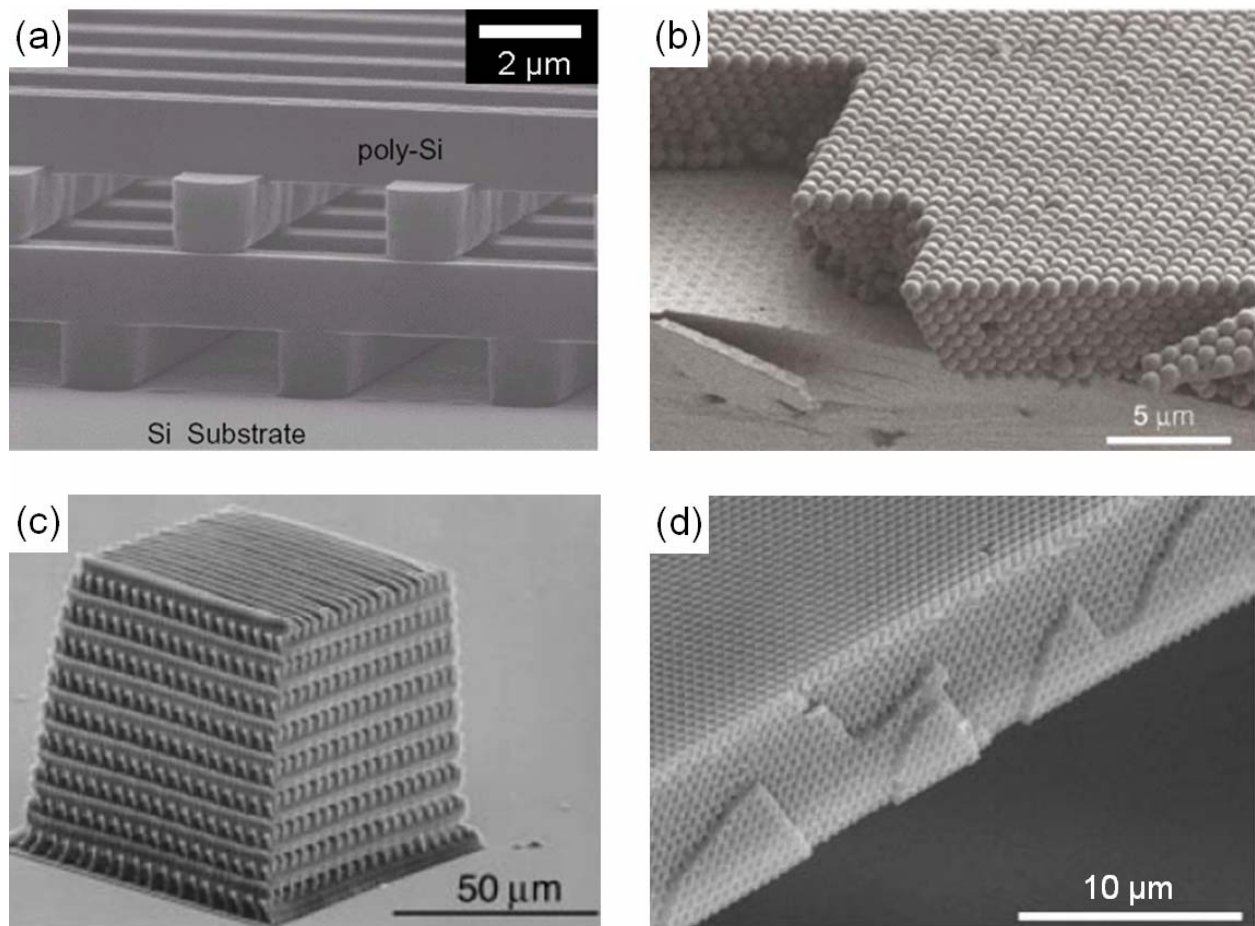


Figure 1.10 SEM images of 3D photonic crystals fabricated via (a) layer-by-layer conventional lithography,[34] (b) colloidal self-assembly,[41] (c) direct laser writing,[36] and (d) holographic lithography.[37]

1.7 PBG Applications

Many applications have been identified for photonic crystals and PBG materials, including low-threshold lasers,[30] low-loss waveguides,[42-44] on-chip optical circuitry,[45] and fiber optics.[46,47] The majority of these applications not only require a PBG material, but also the precise, controlled incorporation of pre-engineered defects (Fig. 1.11, 1.12). These defects disrupt the periodicity of the crystal, creating optical states for the otherwise forbidden bandgap frequencies. Therefore, light coupling to these states can be localized within the defect regions and manipulated by engineering the defect geometry and placement. For example, a complicated 3D defect with sharp bend radius ($\sim\lambda$) may be engineered to guide light along its complex path without loss if defined in a cPBG material.[35] Similarly, point defects may be defined within PBG materials to create embedded optical cavities. Such a cavity containing an emitting material could be used to inhibit spontaneous emission.

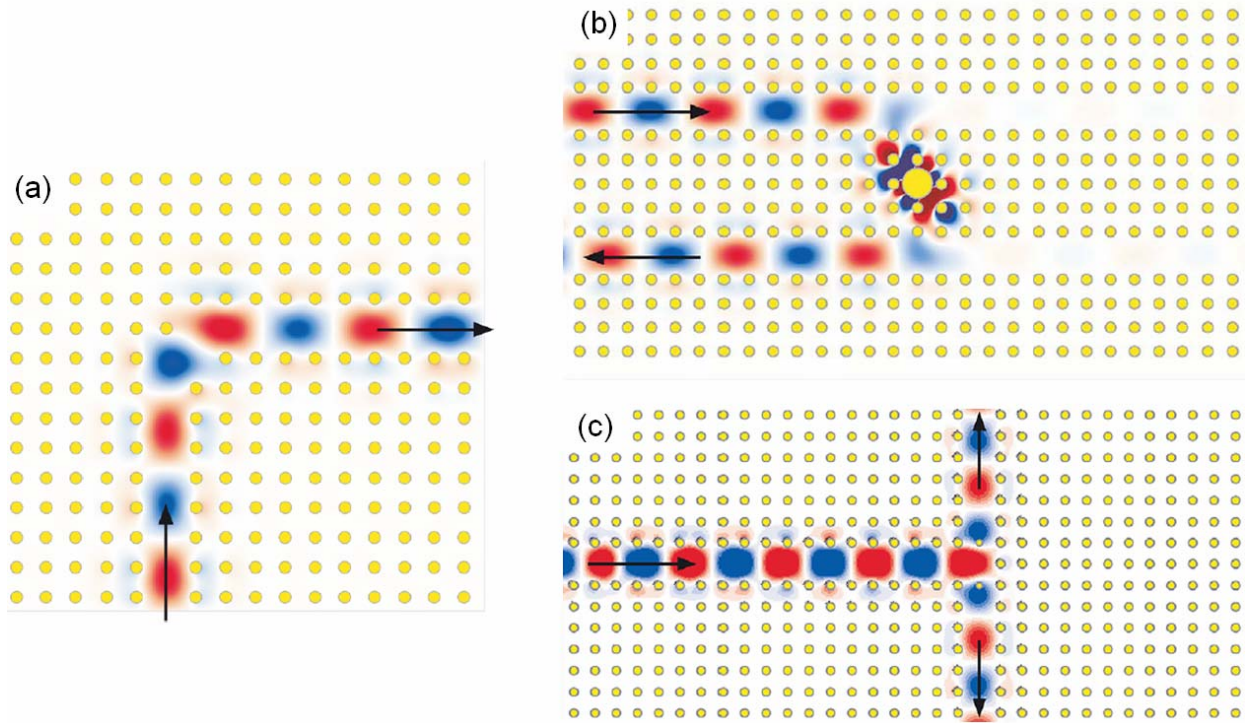


Figure 1.11 Computer simulations of light propagating through an appropriately engineered (a) bend, (b) add-drop filter, and (c) T-splitter in a 2D photonic crystal.[48]

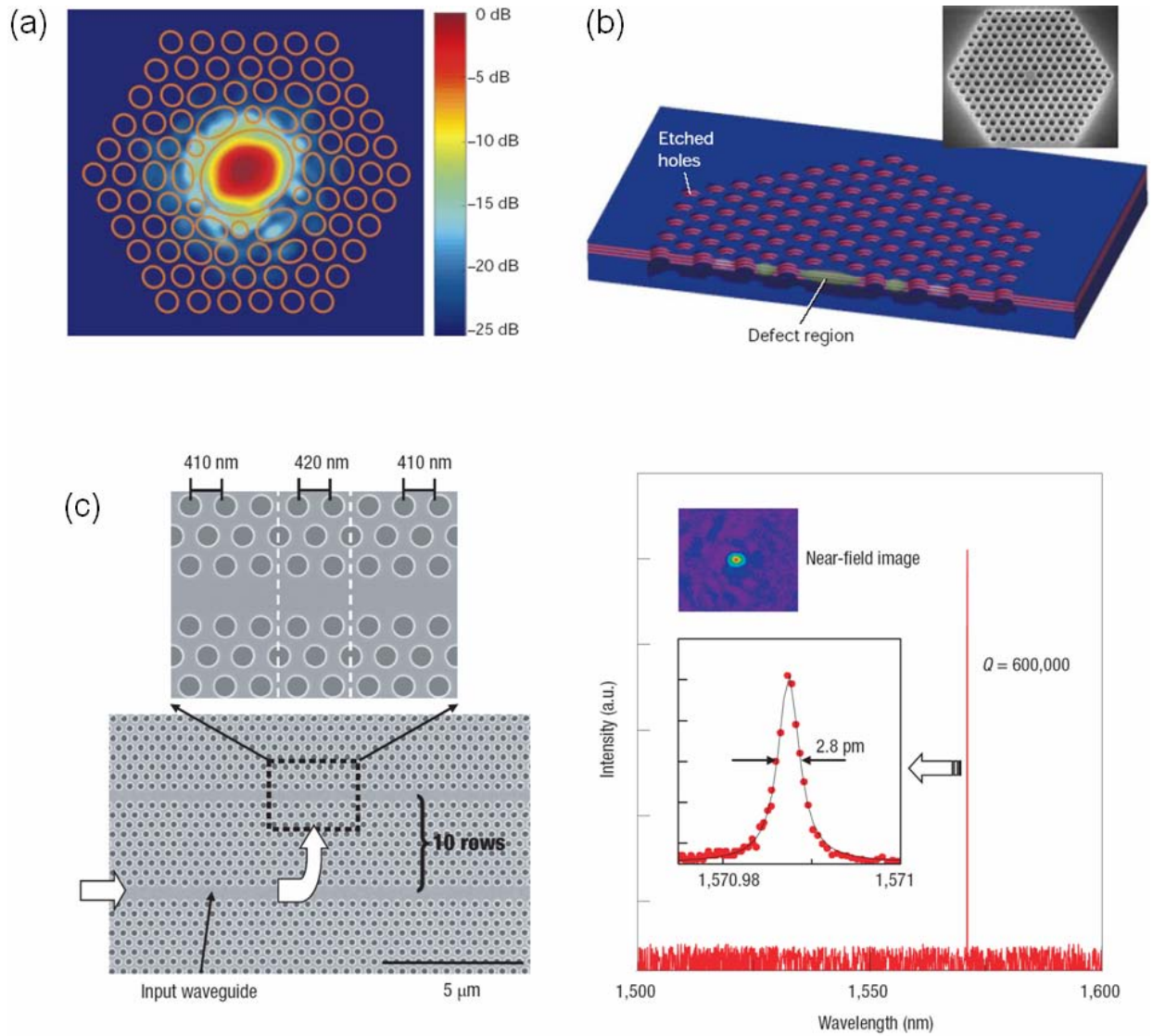


Figure 1.12 (a) Light propagating through a photonic crystal fiber.[49] (b) Schematic and SEM image from a 2D photonic crystal laser.[50] (c) SEM micrograph and spectroscopy from a 2D photonic crystal microcavity with an extremely high quality factor of 600,000.[51]

1.8 Defects in 2D Photonic Crystals

Initially 2D photonic crystals did not generate as much excitement as their 3D counterparts since they cannot rigorously confine light in all dimensions. However, due to the substantial fabrication and modeling advantages in 2D, the experimental and theoretical work on

defect-containing 2D photonic crystals is significantly advanced over that on 3D photonic crystals. The confinement of light to within the plane of a 2D photonic crystal is achieved by sandwiching the 2D photonic crystal between Bragg reflectors,[52] 3D photonic crystals,[53] or lower index materials, including air, to utilize total internal reflection.[54]

2D photonic crystals that operate at optical wavelengths, have a periodicity of ~ 100 nm to $1\text{ }\mu\text{m}$ with feature tolerances in the nanometer range. Typical 2D photonic crystals consist of triangular arrays of air cylinders in a dielectric material, as this geometry can yield a 2D PBG for any polarization, provided the dielectric has a refractive index over 2.7 (Fig. 1.13).[55] With state of the art lithography,[52,56] followed by reactive ion or electrochemical etching, high resolution 2D photonic crystals can be defined in high refractive index materials, including silicon and III-V semiconductors.

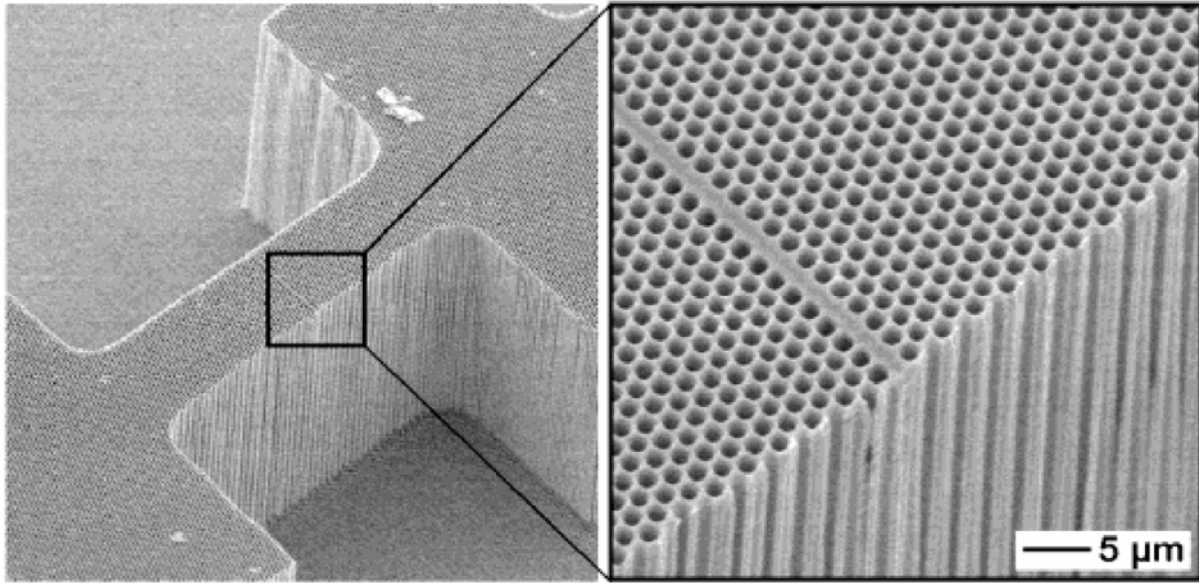


Figure 1.13 SEM micrograph of a macroporous silicon 2D photonic crystal containing a line defect. The pore pitch is $1.5\text{ }\mu\text{m}$ and the photonic crystal is $100\text{ }\mu\text{m}$ deep.[57]

The addition of defects to these structures is carried out simultaneously with the fabrication of the 2D photonic crystal, affording excellent registration between the defects and

lattice. By removing a line of cylinders from the initial design, linear waveguides can be introduced into a 2D PBG material (Fig. 1.13).[57,58] Point defects, formed by removing or reshaping air cylinders, serve as resonant cavities that can trap photons of certain frequencies.[58] Through proper engineering, very high quality factor cavities (up to 600,000) have been reported (Fig. 1.12c).[51] Further, various defect designs have been proposed and, in some cases, realized for low-loss waveguides containing sharp bends (Fig. 1.12a),[44] channel drop filters,[59,60] and T-shaped branches.[61] By introducing active materials (e.g. quantum wells or dots) in the design of the photonic crystal, the possibility of using point defects as resonant cavities for lasing action has also been demonstrated (Fig. 1.12b).[62-64]

1.9. Defects in 3D Photonic Crystals

Although 2D photonic crystals containing exquisitely designed defects have exhibited powerful optical properties, it remains true that complete confinement of light can only be achieved by extending the PBG into the third dimension. From a fabrication and materials standpoint however, as already mentioned, 3D systems containing defined defect structures present a difficult set of challenges. For a cPBG at optical wavelengths, a high resolution 3D fabrication technique and high dielectric constant materials are required, significantly limiting both possible materials and processing routes. Further, for many PBG-based applications, the controlled incorporation of aperiodic defects poses an additional fabrication requirement. Still, processing routes to cPBG materials with embedded defects operating in the visible and infrared have been demonstrated.

For 3D photonic crystals, defects are typically categorized as intrinsic or extrinsic. Intrinsic defect formation is straightforward, as it does not require any special processing aside

from that needed to form the photonic crystal itself (e.g. conventional lithography and direct writing). On the other hand, some photonic crystal fabrication techniques lack an inherent means for the incorporation of defects (e.g. holographic lithography and self-assembly). Therefore it is necessary to employ an appropriate external fabrication technique to introduce aperiodic extrinsic defects before or after formation of the photonic crystal. The lack of any method to controllably incorporate defects within self-assembled and holographic photonic crystals was a major criticism of these fabrication routes five years ago. Since then, however, substantial strides have been made in the development of novel processes for the incorporation of point, linear, planar, and 3D defects within self-assembled photonic crystals. Further, some techniques are also amenable to defect fabrication in holographic photonic crystals. These efforts have now enabled colloidal and holographic photonic crystals to be considered viable options for PBG-based applications.

1.10 Defects in Colloidal Photonic Crystals

Self-assembled colloidal crystals have been widely studied as routes to photonic crystals and PBG materials, in substantial part due to their ease of fabrication and low cost, but also due to their excellent optical properties. Typical colloidal photonic crystals consist of 3D face-centered cubic (FCC) arrays, self-assembled from highly monodisperse silica or polystyrene microspheres with diameters ranging from ~ 200 nm to $2\text{ }\mu\text{m}$.^[65] Countless colloidal crystallization techniques have been published, including gravitational sedimentation (Fig. 1.14a), formation in a flow cell,^[66,67] controlled evaporation (Fig. 1.14b),^[10,41,68] patterned sedimentation,^[69] sonication-assisted packing,^[70] and others.^[71] Most early research focused on improving colloidal crystal quality and inverting them in high refractive index materials.^[72]

This is necessary because only a high refractive index contrast *inverse*-face-centered cubic geometry can possess a cPBG.[73]

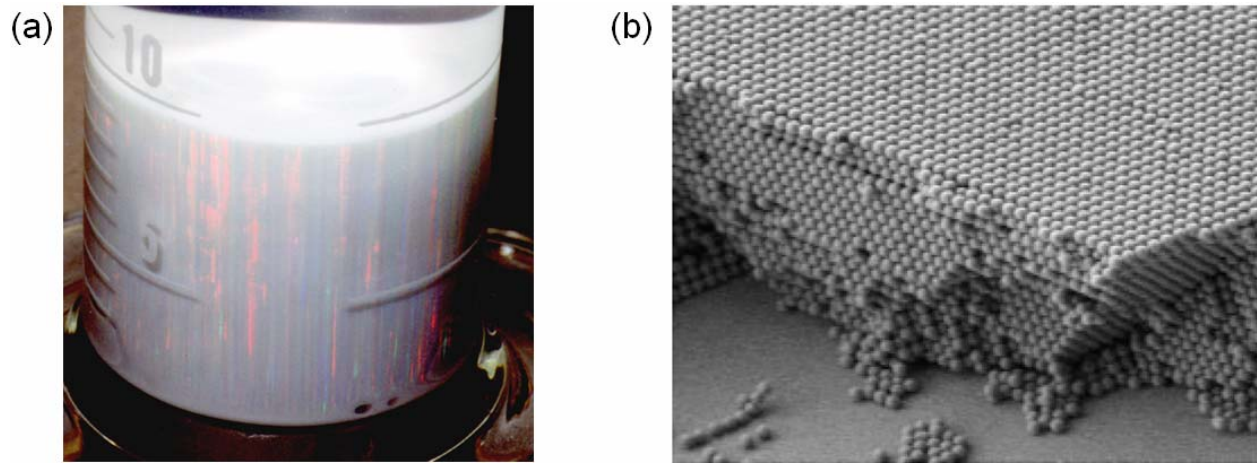


Figure 1.14 (a) Photograph of a silica colloidal sediment exhibiting iridescence upon crystallization in the bottom of a graduated cylinder. Photo of sample prepared in the Lewis group. (b) Scanning electron micrograph from a colloidal crystal deposited from 1 μm silica spheres using a controlled drying technique.[41]

As previously mentioned, to utilize colloidal crystals for most cPBG applications, it is additionally necessary to incorporate designed defects within them. Since the controlled addition of well-defined intrinsic defects is not compatible with the self-assembly process, the viability of self-assembled photonic crystals for many PBG-based applications relies on a compatible external defect fabrication technique. Here, defect fabrication techniques applied for use in colloidal photonic crystals will be discussed in terms of their potential resolution, accuracy of registration with the underlying photonic crystal lattice, flexibility in defining complicated embedded 3D structures, and their potential to incorporate materials that might impart additional functionality. Where available, optical characterization and theoretical modeling of these defects will also be discussed.

1.10.1 Substitutional Doping

Although well-defined defects in colloidal crystals may have the greatest long term potential, significant strides in understanding the impact of defects can be determined through the random placement of defects. The first intentional incorporation of optical defect states in a colloidal crystal was accomplished intrinsically via substitutional doping. Watson *et al.* doped colloidal suspensions with microspheres of different sizes or dielectric constants, and used this mixture to grow colloidal crystals with substitutional impurities.[74] Near-IR transmission spectroscopy was used to probe the optical properties of the wet crystals doped with both donor and acceptor impurities. Defect modes as well as a significant widening of the optical stop band were observed (Fig. 1.15). Spectra simulated using the transfer matrix method[14] qualitatively agreed with experimental results, though a quantitative comparison was not possible.

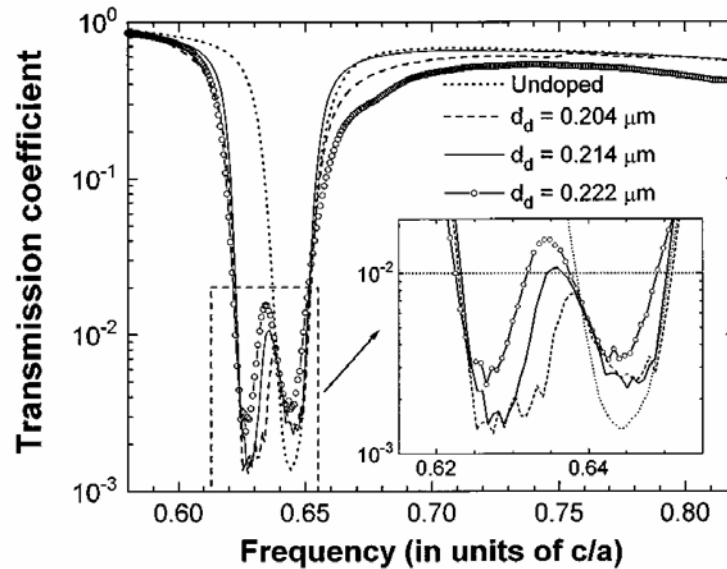


Figure 1.15 Near-IR transmission spectra for colloidal crystals containing intrinsic polystyrene donor impurities (10% number fraction) expressed in normalized frequency units (c/a), where c is the frequency of light and a is the FCC lattice constant. The host colloid diameter is 173 nm, the dopant colloids have diameters of 204, 214, and 222 nm. The dotted curve is collected from an undoped colloidal crystal, the other curves are from doped colloidal crystals.[74]

Another doping study by Xia *et al.* and later by Lopez *et al.* observed a reduction in attenuation of transmittance within the optical stop band with increasing impurity concentration in dried colloidal crystals, however distinguishable defect modes within the gap were not observed.[75,76] Substitutional doping does not afford control of defect placement and can therefore only be used to create randomly distributed point defects. For the fabrication of more complex defect structures, required for many advanced functionalities, an external fabrication technique is necessary.

1.10.2 2D Embedded Defects via Multi-Step Procedures

Several multi-step procedures have been developed for the fabrication of extrinsic point, linear, and planar defects within self-assembled photonic crystals. These approaches generally incorporate a 2D plane of defects sandwiched between two colloidal crystals. The procedure begins with the growth of a colloidal crystal, followed by the deposition of an intermediate layer and perhaps 2D lithographic patterning of this layer, and is concluded with the growth of an overlying colloidal crystal. Additional steps may include filling the interstitial space of the colloidal crystal and template removal. In this fashion, embedded features of limited dimensionality can be incorporated within self-assembled photonic crystals.

Through electron beam (e-beam) and nano-imprint lithography extrinsic point defects can be defined in or on colloidal crystals (Fig. 1.16). E-beam lithography was used to individually expose an array of spheres on the top layer of a colloidal crystal and it was proposed that an additional colloidal crystal could be grown before development to embed the defects.[77] Nano-imprint lithography was used to introduce a plane of point defects between two colloidal multilayers.[78] Alignment of defects with the colloidal crystal lattice was not possible and

multiple additional processing steps were required to embed the layer of defects, however, since nano-imprint lithography is a parallel, less time-consuming process than e-beam lithography, it may still find application. It will be interesting to compare the optical properties of a 2D embedded layer of extrinsic point defects with those from randomly three-dimensionally distributed intrinsic point defects introduced via substitutional doping (Section 1.10.1)

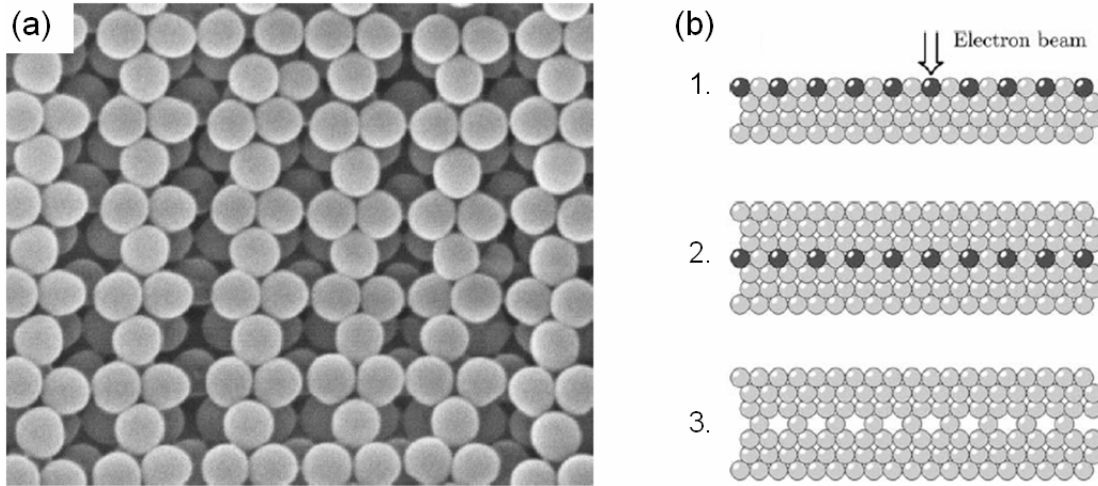


Figure 1.16 (a) SEM image presenting a rectangular lattice of point defects defined on the surface of a poly(methyl methacrylate) colloidal crystal (lattice parameter is 498 nm). (b) Proposed process for embedding defects: 1. e-beam exposure, 2. growth of second colloidal crystal, 3. development of exposed regions.[77]

Clearly, it is straightforward to extend e-beam and nano-imprint techniques to define linear and other 2D defects in colloidal crystals.[78-81] A similar approach to define embedded linear extrinsic defects is to use conventional photolithography to pattern a photoresist deposited on a colloidal crystal (Fig. 1.17). Following the assembly of another crystal on this structure and removal of the photoresist, buried linear air defects have been incorporated within colloidal crystals.[82,83] While these linear defects have been suggested for use as waveguides, optics have only been measured normal to their long axis.[82] There is a report that measures

transmission through “opal-clad” waveguides however in that case the waveguide is not completely surrounded by the colloidal crystal.[84]

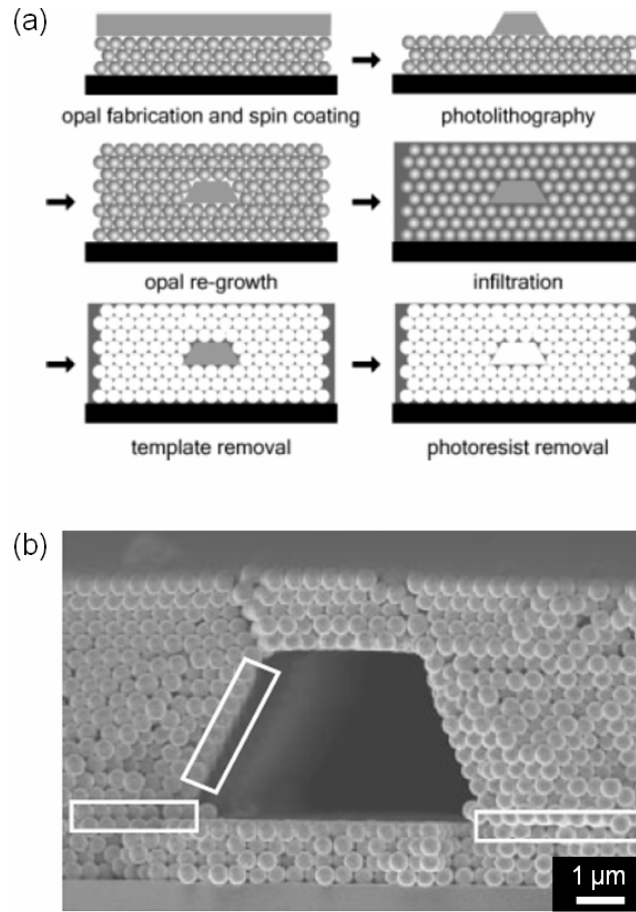


Figure 1.17 (a) Schematic procedure for incorporating line defects within colloidal crystals. (b) SEM of an air-core line defect, embedded in a silica colloidal crystal. Boxes highlight the high quality registration between the defect, original colloidal crystal, and that grown via a second deposition.[83] Similar results were concurrently obtained by Ozin *et al.*[82]

Another technique used to define extrinsic linear defects in colloidal crystal based photonic crystals is laser microannealing, which was used to write micron-scale defects on the surface of silicon inverse opals by inducing a localized phase transition from amorphous Si:H to nanocrystalline Si:H,[85] resulting in a lowering of the refractive index in the microannealed

region from 4.00 to 3.85 (3.75 %) (Fig. 1.18). If the degree of crystallinity in the annealed region can be improved to yield a larger refractive index change, and an approach developed to form an additional silicon inverse opal on top of the defined defect, laser microannealing may enable the definition of useful defects in silicon inverse opals.

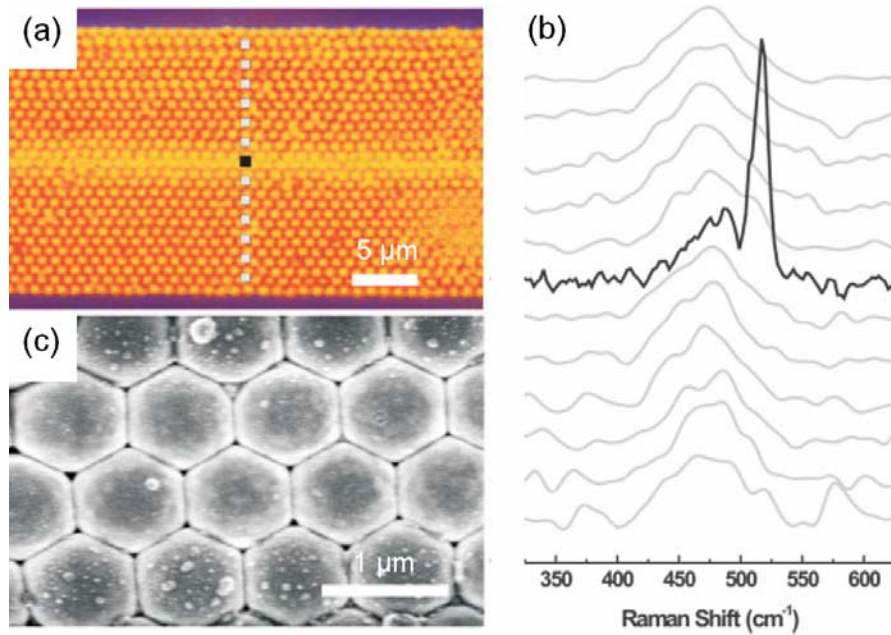


Figure 1.18 (a) Optical and (b) SEM micrographs showing a laser micro-annealed line of nanocrystalline Si:H in an amorphous Si:H inverse opal. The vertical line of squares in (a) denote the regions from which the Raman spectra in (c) were collected.[85]

Colvin *et al.* constructed colloidal superlattices with engineered midgap states via multiple depositions of colloidal layers with alternating colloid sizes.[86,87] Qualitative correspondence between normal incidence spectroscopy data and scalar wave approximation simulations supported the presence of superlattice effects (Fig. 1.19).[87] Similarly, Persoons *et al.* incorporated the first 2D embedded planar defect within a colloidal crystal using a multi-step colloidal growth process.[88,89] This structure consisted of two colloidal multilayers sandwiching an embedded monolayer of larger spheres. The colloidal multilayers were grown

via vertical deposition, while a Langmuir-Blodgett technique was used to uniformly deposit the monolayer of larger spheres. Transmission measurements were used to confirm the presence of a defect mode within the pseudogap and establish the impact of monolayer thickness on the position of the defect mode.[88,89]

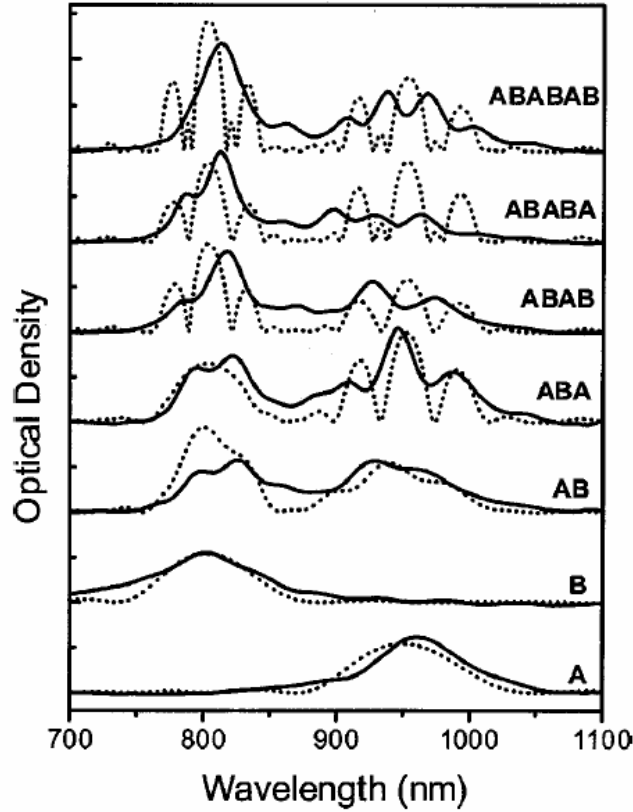


Figure 1.19 Experimental (solid) and simulated (dashed) spectroscopy from a series of colloidal crystal superlattices deposited by alternating layers of microspheres (A spheres are 451 nm and B spheres are 381 nm). Spectra were simulated using SWA and an overall multiplicative scaling was applied for each curve to facilitate comparison between experiment and theory.[87]

A multiple step procedure for incorporating an extrinsic embedded planar defect consisting of a layer of silica between two silica-air inverse opals is shown in Figure 1.20.[90,91] The impact of the silica defect layer thickness on position of the defect mode within the pseudogap was studied experimentally[90-92] and via scalar wave approximation

calculations.[91] The overall shape of the spectra agreed qualitatively, however a discrepancy was noted in the reflectance intensities and all theoretical spectra were scaled by an arbitrary factor to enable comparison.[91] Active planar embedded defects were incorporated into a colloidal crystal via the growth or transfer printing of a polyelectrolyte multilayer on a colloidal crystal followed by the subsequent growth of a second colloidal crystal.[93] The polyelectrolyte multilayer swells in response to a chemical, optical, or thermal stimulus which gives rise to a small but detectable shift in the position of the defect mode within the pseudogap.[93-95]

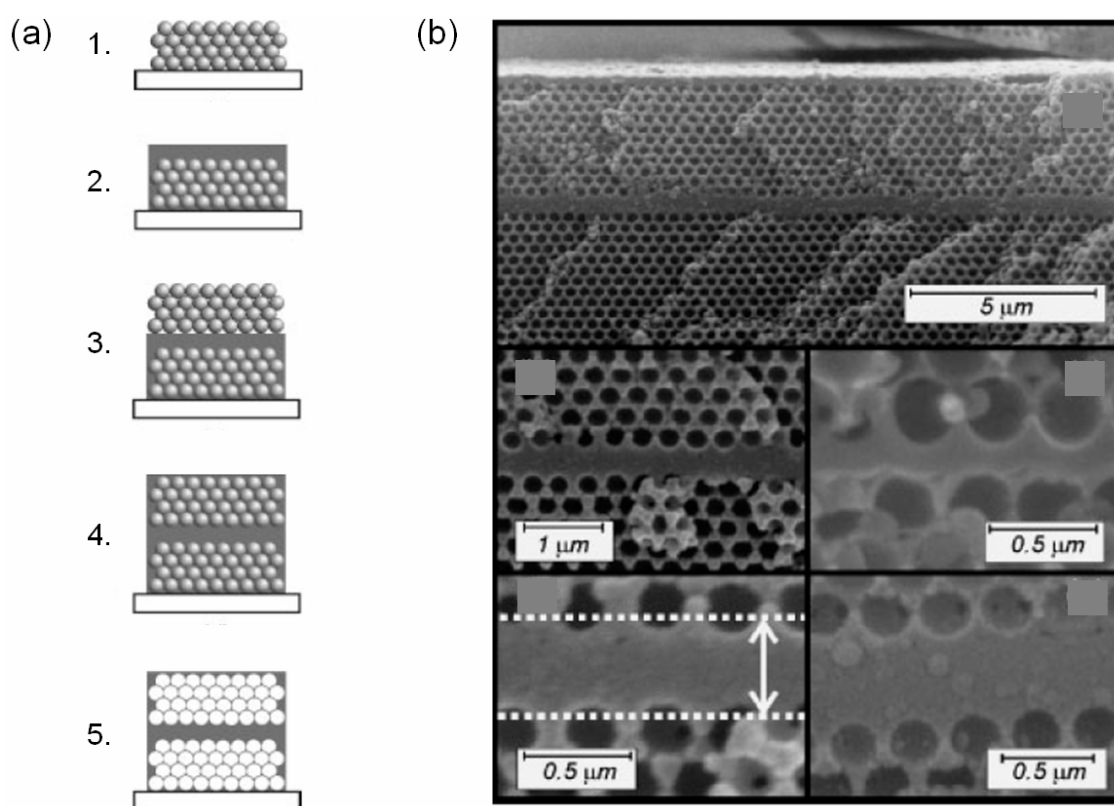


Figure 1.20 (a) Schematic procedure for embedding planar defects in colloidal photonic crystals: 1. formation of polystyrene colloidal crystal, 2. infiltration of colloidal crystal with silica and growth of excess layer, 3. deposition of second polystyrene colloidal crystal, 4. infiltration of second colloidal crystal with silica, 5. removal of polystyrene. (b) SEM demonstrating the incorporation of silica planar defects with defined thicknesses within silica inverse opals. Sphere diameter is 375 ± 15 nm.[91] Similar results were concurrently obtained by Lopez *et al.*[90]

1.10.3 3D Embedded Defects via Two-Photon Polymerization

Although a number of approaches have been proposed for forming defects of limited dimensionality, to impart advanced functionalities, it is necessary to be able to controllably incorporate complex pre-engineered defects with 3D spatial control. We demonstrated first method for incorporating well-defined 3D defects within colloidal crystals.[96]

This attractive technique employs two-photon polymerization (TPP) (for description, see Section 2.2) to fabricate high-resolution 3D embedded polymer features within colloidal crystals.[97] After infiltrating the colloidal crystal with a two-photon polymerizable resin, a localized excitation volume is scanned throughout the material to expose the desired regions, defining high resolution 3D embedded features (Fig. 1.21). TPP can also be used to define features in photonic crystals formed by holography (see Chapter 5).[98]

TPP is an appealing method for writing defects within self-assembled or holographic photonic crystals for a number of reasons. TPP is a flexible technique capable of writing isolated, embedded, 3D features throughout the bulk of a crystal (on the order of 150 μm deep). Further, TPP affords high resolution, with the smallest reported polymerizable volume element being an ellipsoid of ~ 100 nm by ~ 300 nm.[99] When done in conjunction with *in situ* fluorescence confocal imaging, it is possible to pinpoint the location of the TPP features with respect to the photonic crystal lattice.[98]

An important consideration for any cPBG application is the ability to convert the photonic crystal to a high refractive index structure which exhibits a cPBG. Generally, this is accomplished for colloidal photonic crystals through infiltration with a high index material such as Si at an elevated temperature, followed by removal of the silica, resulting in an inverse opal structure. Here, both the TPP features and colloidal crystal serve as a template for the final

structure, resulting in a silicon-air inverse opal which may possess a cPBG containing embedded air defects (see Chapters 3 and 4 for further details).[100]

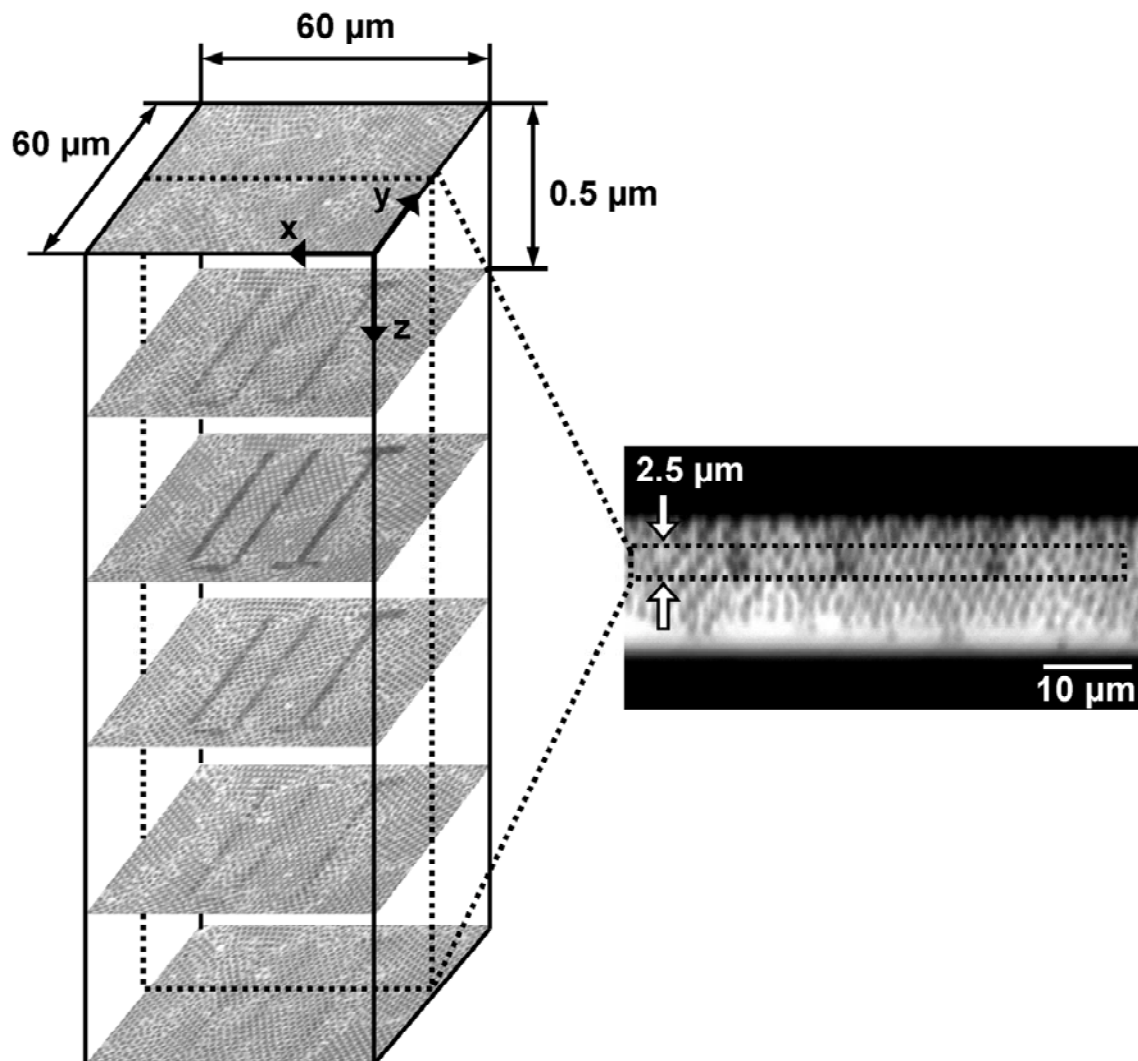


Figure 1.21 Fluorescence confocal micrographs of a feature formed through TPP in a colloidal crystal taken after rinsing to remove unreacted monomer and backfilling with a fluorescent dye solution. On the left are serial cross-sections collected at 0.5 μm increments and on the right is a vertical cross-sectional image of the isolated, embedded feature fabricated within the colloidal template through multi-photon polymerization.

TPP in colloidal crystals is a very flexible fabrication approach for the formation of complex structures, however guidance for the design of optically interesting defects in colloidal photonic crystals is limited. The most notable effort to date on theory and computation of waveguide structures in colloidal crystals was recently published by Fan *et al.*, where it was proposed that coupled cavities will be much more efficient for the guiding of light in an inverse opal based photonic crystal than simple tube-like defects.[101] Coupled cavities contain a much larger fraction of the light in the air voids, while simple tube-like guides concentrate most of the light in the walls of the tube, where scattering and other loss mechanisms are much more likely to operate.

1.11 References

1. A. W. Eckert, *The World of Opals*; John Wiley & Sons, Inc.: New York, NY, **1997**.
2. J. V. Sanders, *Nature* **1964**, *204*, 1151.
3. <http://www.shed.com/aom/cuts/xtalpics/x4133d.jpg>, April 19, 2006.
4. V. N. Astratov, V. N. Bogomolov, A. A. Kaplyanskii, A. V. Prokofiev, L. A. Samoilovich, S. M. Samoilovich, Y. A. Vlasov, *Nuovo Cimento D* **1995**, *17*, 1349.
5. C. Lopez, *Adv. Mater.* **2003**, *15*, 1679.
6. P. A. Hiltner, I. M. Krieger, *J. Phys. Chem.* **1969**, *73*, 2386.
7. F. Garcia-Santamaria, Universidad Autonoma de Madrid, **2003**.
8. KKR simulations were performed using the MULTTEM program.
9. N. Stefanou, V. Yannopapas, A. Modinos, *Comput. Phys. Commun.* **1998**, *113*, 49.
10. P. Jiang, J. F. Bertone, K. S. Hwang, V. L. Colvin, *Chem. Mater.* **1999**, *11*, 2132.
11. M. Born, E. Wolf, *Principles of Optics*; Pergamon Press, **1986**.
12. S. Satpathy, Z. Zhang, M. R. Salehpour, *Phys. Rev. Lett.* **1990**, *64*, 1239.

13. D. M. Mittleman, J. F. Bertone, P. Jiang, K. S. Hwang, V. L. Colvin, *J. Chem. Phys.* **1999**, *111*, 345.
14. J. B. Pendry, A. Mackinnon, *Phys. Rev. Lett.* **1992**, *69*, 2772.
15. P. M. Bell, J. B. Pendry, L. M. Moreno, A. J. Ward, *Comput. Phys. Commun.* **1995**, *85*, 306.
16. C. T. Chan, Q. L. Yu, K. M. Ho, *Phys. Rev. B* **1995**, *51*, 16635.
17. K. Sakoda, J. Kawamata, *Opt. Express* **1998**, *3*, 12.
18. Band diagrams were calculated using MIT Photonic Bands.
19. D. Roundy, M. Ibanescu, P. Bermel, A. Farjadpour, J. D. Joannopoulos, and S. G. Johnson, The Meep FDTD package, <http://ab-initio.mit.edu/meep/>.
20. S. G. Johnson, J. D. Joannopoulos, *Opt. Express* **2001**, *8*, 173.
21. Y. A. Vlasov, M. Deutsch, D. J. Norris, *Appl. Phys. Lett.* **2000**, *76*, 1627.
22. J. F. Galisteo-Lopez, E. Palacios-Lidon, E. Castillo-Martinez, C. Lopez, *Phys. Rev. B* **2003**, *68*, 5109.
23. J. H. Holtz, S. A. Asher, *Nature* **1997**, *389*, 829.
24. J. H. Holtz, J. S. W. Holtz, C. H. Munro, S. A. Asher, *Anal. Chem.* **1998**, *70*, 780.
25. Y.-J. Lee, P. V. Braun, *Adv. Mater.* **2003**, *15*, 563.
26. Y. J. Lee, S. A. Pruzinsky, P. V. Braun, *Langmuir* **2004**, *20*, 3096.
27. Y. J. Lee, S. A. Pruzinsky, P. V. Braun, *Opt. Lett.* **2005**, *30*, 153.
28. A. F. Koenderink, W. L. Vos, *Phys. Rev. Lett.* **2003**, *91*.
29. V. P. Bykov, *Sov. J. Quant. Electron.* **1975**, *4*, 861.
30. E. Yablonovitch, *Phys. Rev. Lett.* **1987**, *58*, 2059.
31. S. John, *Phys. Rev. Lett.* **1987**, *58*, 2486.
32. K. Busch, S. John, *Phys. Rev. E* **1998**, *58*, 3896.
33. <http://www.elec.gla.ac.uk/groups/opto/photoniccrystal/Welcome.html>, February 2003.
34. S.-Y. Lin, J. G. Fleming, D. L. Hetherington, B. K. Smith, R. Biswas, K. M. Ho, M. M. Sigalas, W. Zubrzycki, S. R. Kurth, J. Bur, *Nature* **1998**, *394*, 251.

35. S. Noda, K. Tomoda, N. Yamamoto, A. Chutinan, *Science* **2000**, 289, 604.
36. B. H. Cumpston, S. P. Ananthavel, S. Barlow, D. L. Dyer, J. E. Ehrlich, L. L. Erskine, A. A. Heikal, S. M. Kuebler, I. Y. S. Lee, D. McCord-Maughon, J. Q. Qin, H. Rockel, M. Rumi, X. L. Wu, S. R. Marder, J. W. Perry, *Nature* **1999**, 398, 51.
37. M. Campbell, D. N. Sharp, M. T. Harrison, R. G. Denning, A. J. Turberfield, *Nature* **2000**, 404, 53.
38. S. R. Kennedy, M. J. Brett, O. Toader, S. John, *Nano Lett.* **2002**, 2, 59.
39. G. Mertens, R. B. Wehrspohn, H. S. Kitzerow, S. Matthias, C. Jamois, U. Gosele, *Appl. Phys. Lett.* **2005**, 87.
40. F. García-Santamaría, H. T. Miyazaki, A. Urquia, M. Ibisate, M. Belmonte, N. Shinya, F. Meseguer, C. Lopez, *Adv. Mater.* **2002**, 14, 1144.
41. Y. A. Vlasov, X. Z. Bo, J. C. Sturm, D. J. Norris, *Nature* **2001**, 414, 289.
42. R. D. Meade, A. Devenyi, J. D. Joannopoulos, O. L. Alerhand, D. A. Smith, K. Kash, *J. Appl. Phys.* **1994**, 75, 4753.
43. S. H. Fan, J. N. Winn, A. Devenyi, J. C. Chen, R. D. Meade, J. D. Joannopoulos, *J. Opt. Soc. Am. B* **1995**, 12, 1267.
44. A. Mekis, J. C. Chen, I. Kurland, S. H. Fan, P. R. Villeneuve, J. D. Joannopoulos, *Phys. Rev. Lett.* **1996**, 77, 3787.
45. S. John, T. Quang, *Phys. Rev. Lett.* **1997**, 78, 1888.
46. Y. Fink, J. N. Winn, S. H. Fan, C. P. Chen, J. Michel, J. D. Joannopoulos, E. L. Thomas, *Science* **1998**, 282, 1679.
47. P. Russell, *Science* **2003**, 299, 358.
48. S. G. Johnson, J. D. Joannopoulos, **2003**, 51, 5823.
49. J. C. Knight, *Nature* **2003**, 424, 848.
50. K. J. Vahala, *Nature* **2003**, 424, 839.
51. B. S. Song, S. Noda, T. Asano, Y. Akahane, *Nature Mater.* **2005**, 4, 207.
52. J. R. Wendt, G. A. Vawter, P. L. Gourley, T. M. Brennan, B. E. Hammons, *J. Vac. Sci. Technol. B* **1993**, 11, 2637.
53. A. Chutinan, S. John, O. Toader, *Phys. Rev. Lett.* **2003**, 90.
54. T. F. Krauss, R. M. DeLaRue, S. Brand, *Nature* **1996**, 383, 699.

55. R. D. Meade, K. D. Brommer, A. M. Rappe, J. D. Joannopoulos, *Appl. Phys. Lett.* **1992**, *61*, 495.
56. Y. N. Xia, G. M. Whitesides, *Annu. Rev. Mater. Sci.* **1998**, *28*, 153.
57. A. Birner, R. B. Wehrspohn, U. M. Gosele, K. Busch, *Adv. Mater.* **2001**, *13*, 377.
58. S. Noda, A. Chutinan, M. Imada, *Nature* **2000**, *407*, 608.
59. S. H. Fan, P. R. Villeneuve, J. D. Joannopoulos, H. A. Haus, *Opt. Express* **1998**, *3*, 4.
60. H. Takano, B. S. Song, T. Asano, S. Noda, *Appl. Phys. Lett.* **2005**, *86*.
61. S. H. Fan, S. G. Johnson, J. D. Joannopoulos, C. Manolatou, H. A. Haus, *J. Opt. Soc. Am. B* **2001**, *18*, 162.
62. O. Painter, R. K. Lee, A. Scherer, A. Yariv, J. D. O'Brien, P. D. Dapkus, I. Kim, *Science* **1999**, *284*, 1819.
63. M. Fujita, S. Takahashi, Y. Tanaka, T. Asano, S. Noda, *Science* **2005**, *308*, 1296.
64. T. Yoshie, A. Scherer, J. Hendrickson, G. Khitrova, H. M. Gibbs, G. Rupper, C. Ell, O. B. Shchekin, D. G. Deppe, *Nature* **2004**, *432*, 200.
65. A. P. Philipse, *J. Mater. Sci. Lett.* **1989**, *8*, 1371.
66. S. A. Asher, Crystalline Colloidal Narrow Band Radiation Filter, US Patent 4627689, **1986**.
67. S. A. Asher, J. Holtz, L. Liu, Z. J. Wu, *J. Am. Chem. Soc.* **1994**, *116*, 4997.
68. A. S. Dimitrov, K. Nagayama, *Langmuir* **1996**, *12*, 1303.
69. P. V. Braun, R. W. Zehner, C. A. White, M. K. Weldon, C. Kloc, S. S. Patel, P. Wiltzius, *Adv. Mater.* **2001**, *13*, 721.
70. Y. Lu, Y. D. Yin, B. Gates, Y. N. Xia, *Langmuir* **2001**, *17*, 6344.
71. Y. N. Xia, B. Gates, Y. D. Yin, Y. Lu, *Adv. Mater.* **2000**, *12*, 693.
72. O. D. Velev, T. A. Jede, R. F. Lobo, A. M. Lenhoff, *Nature* **1997**, *389*, 447.
73. H. S. Sozuer, J. W. Haus, R. Inguva, *Phys. Rev. B* **1992**, *45*, 13962.
74. R. D. Pradhan, Tarhan, II, G. H. Watson, *Phys. Rev. B* **1996**, *54*, 13721.
75. B. Gates, Y. Xia, *Appl. Phys. Lett.* **2001**, *78*, 3178.
76. E. Palacios-Lidon, B. H. Juarez, E. Castillo-Martinez, C. Lopez, *J. Appl. Phys.* **2005**, *97*.

77. F. Jonsson, C. M. S. Torres, J. Seekamp, M. Schniedergers, A. Tiedemann, J. H. Ye, R. Zentel, *Microelectron. Eng.* **2005**, 78-79, 429.
78. Q. F. Yan, A. Chen, S. J. Chua, X. S. Zhao, *Adv. Mater.* **2005**, 17, 2849.
79. P. Ferrand, M. Egen, R. Zentel, J. Seekamp, S. G. Romanov, C. M. S. Torres, *Appl. Phys. Lett.* **2003**, 83, 5289.
80. P. Ferrand, J. Seekamp, M. Egen, R. Zentel, S. G. Romanov, C. M. S. Torres, *Microelectron. Eng.* **2004**, 73-74, 362.
81. B. H. Juarez, D. Golmayo, P. A. Postigo, C. Lopez, *Adv. Mater.* **2004**, 16, 1732.
82. E. Vekris, V. Kitaev, G. von Freymann, D. D. Perovic, J. S. Aitchison, G. A. Ozin, *Adv. Mater.* **2005**, 17, 1269.
83. Q. F. Yan, Z. C. Zhou, X. S. Zhao, S. J. Chua, *Adv. Mater.* **2005**, 17, 1917.
84. K. H. Baek, A. Gopinath, *IEEE Photonic Tech. L.* **2005**, 17, 351.
85. N. Tetreault, H. Miguez, S. M. Yang, V. Kitaev, G. A. Ozin, *Adv. Mater.* **2003**, 15, 1167.
86. P. Jiang, G. N. Ostojic, R. Narat, D. M. Mittleman, V. L. Colvin, *Adv. Mater.* **2001**, 13, 389.
87. R. Rengarajan, P. Jiang, D. C. Larrabee, V. L. Colvin, D. M. Mittleman, *Phys. Rev. B* **2001**, 6420.
88. K. Wostyn, Y. X. Zhao, G. de Schaetzen, L. Hellemans, N. Matsuda, K. Clays, A. Persoons, *Langmuir* **2003**, 19, 4465.
89. Y. X. Zhao, K. Wostyn, G. de Schaetzen, K. Clays, L. Hellemans, A. Persoons, M. Szekeres, R. A. Schoonheydt, *Appl. Phys. Lett.* **2003**, 82, 3764.
90. E. Palacios-Lidon, J. F. Galisteo-Lopez, B. H. Juarez, C. Lopez, *Adv. Mater.* **2004**, 16, 341.
91. N. Tetreault, A. Mihi, H. Miguez, I. Rodriguez, G. A. Ozin, F. Meseguer, V. Kitaev, *Adv. Mater.* **2004**, 16, 346.
92. B. Z. Wang, W. Zhao, A. Chen, S. J. Chua, *J. Crystal Growth* **2006**, 288, 200.
93. N. Tetreault, A. C. Arsenault, A. Mihi, S. Wong, V. Kitaev, I. Manners, H. Miguez, G. A. Ozin, *Adv. Mater.* **2005**, 17, 1912.
94. F. Fleischhaker, A. C. Arsenault, V. Kitaev, F. C. Peiris, G. von Freymann, I. Manners, R. Zentel, G. A. Ozin, *J. Am. Chem. Soc.* **2005**, 127, 9318.

95. F. Fleischhaker, A. C. Arsenault, Z. Wang, V. Kitaev, F. C. Peiris, G. von Freymann, I. Manners, R. Zentel, G. A. Ozin, *Adv. Mater.* **2005**, *17*, 2455.
96. W. M. Lee, S. A. Pruzinsky, P. V. Braun, *Adv. Mater.* **2002**, *14*, 271.
97. S. A. Pruzinsky, P. V. Braun, *Adv. Funct. Mater.* **2005**, *15*, 1995.
98. J. Scrimgeour, D. N. Sharp, C. F. Blanford, O. M. Roche, R. G. Denning, A. J. Turberfield, *Adv. Mater.* **2006**, *In Press*.
99. K. Takada, H. B. Sun, S. Kawata, *Appl. Phys. Lett.* **2005**, *86*, 71122.
100. Y. H. Jun, C. A. Leatherdale, D. J. Norris, *Adv. Mater.* **2005**, *17*, 1908.
101. V. Lousse, S. H. Fan, *Opt. Express* **2006**, *14*, 866.

CHAPTER 2

TWO-PHOTON POLYMERIZATION

Significant components of this chapter were published as S. A. Pruzinsky, P. V. Braun, “Fabrication and Characterization of Two-Photon Polymerized Features in Colloidal Crystals” *Advanced Functional Materials* **2005**, *15*, 1995-2004.

2.1 Motivation

At the time this thesis began, a major criticism of self-assembled and holographic routes to 3D photonic crystals was the inability to controllably incorporate aperiodic defects within these structures. Without this ability, these classes of photonic crystals are not viable options for the majority of PBG-based applications. The first goal of this thesis work was to identify and demonstrate a flexible and robust technique for the definition of defects within self-assembled and holographic photonic crystals. To this end, we employed two-photon polymerization, which enables the definition of arbitrarily complex, 3D, high resolution features, while affording in-situ imaging and therefore good registration of defects with the underlying photonic crystal lattice.[1,2] This chapter will focus on the development of TPP in colloidal photonic crystals, while Chapter 5 will cover preliminary demonstrations of TPP in holographic photonic crystals. High index replication and characterization of colloidal crystals with embedded defects will be covered in Chapters 3 and 4, respectively.

2.2 Introduction to TPP

TPP begins with the two-photon excitation of a dye molecule which then directly or indirectly initiates polymerization. Two-photon excitation (TPE) was first predicted in 1931 by

Göppert-Mayer who theorized that a dye molecule could essentially simultaneously absorb two photons to be excited via a virtual state into a high energy state (Fig. 2.1).[3] Due to the very small cross-section (on the order of $10^{-50} \text{ cm}^4 \text{ s photon}^{-1}$) of this nonlinear process, it is extremely inefficient and a very intense source is required to realize significant TPE. Accordingly, it was not until just after the invention of the laser in 1960,[4-6] that the first experimental observation of TPE was reported.[7] Around 1990, the advent of appropriate scanning microscopy technologies and mode-locked lasers with sub-picosecond pulsewidths and repetition rates on the order of 100 MHz[8] enabled the first demonstrations of two-photon fluorescence microscopy[9] and two-photon polymerization.[10]

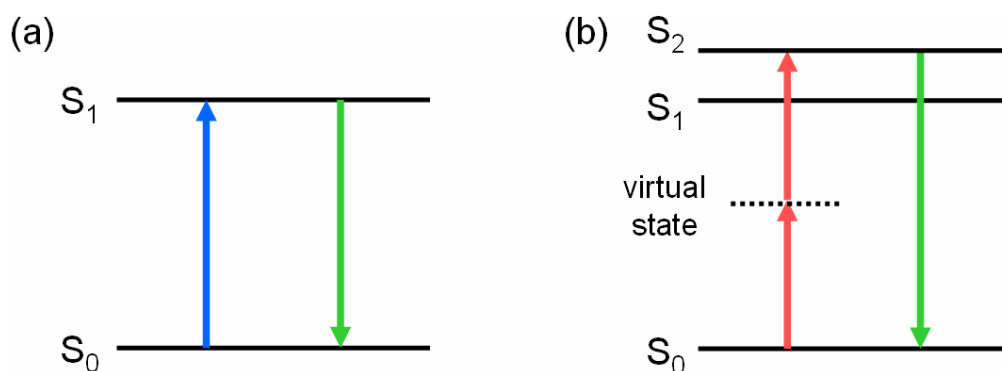


Figure 2.1 Schematic of (a) single- and (b) two-photon excitation processes. Here, the absorption of a single photon ($h\nu$) or two photons ($\frac{1}{2} h\nu$ each) can excite a dye molecule into a high energy state. This energy can be re-emitted as a fluorescent photon, which is red-shifted in the case of single-photon excitation or blue-shifted for TPE.

The nonlinear absorption as a function of intensity in TPE gives rise to a dramatic difference in the number of molecules excited as a function of distance from the center of the focal point of a tightly focused laser beam. Therefore, a significant number of molecules are only excited in a very small volume around the focal point, with dimensions on the order of the resolution limit (Fig. 2.2).

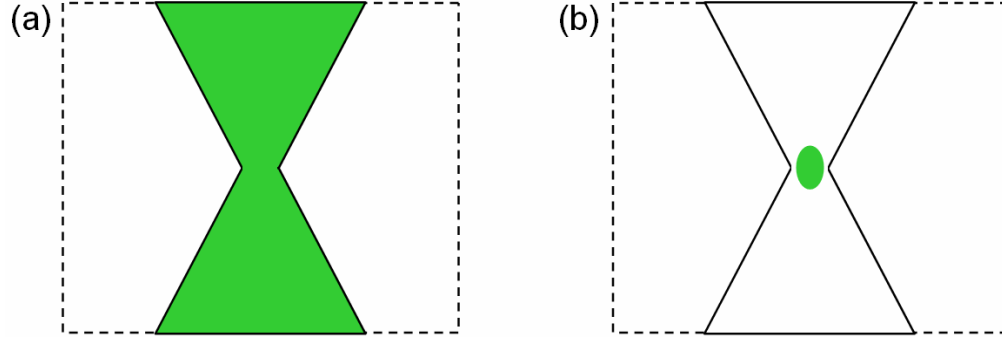


Figure 2.2 Cross-sectional schematic of the beam profile (solid line) of a tightly focused laser beam as it passes through a sample. Typical excitation volume (green shaded regions) in non-thresholded (a) single- and (b) two-photon excitation processes.

If a two-photon excited molecule exhibits strong up-converted fluorescence or initiates polymerization, there is potential to utilize this localized excitation for high resolution, 3D fluorescence imaging[9] or feature fabrication.[10] This is achieved by scanning the focal point of a tightly-focused laser beam throughout a sample which has negligible linear absorption at the wavelength of the two-photon excitation. This concept was first outlined in 1978,[11] but again, there was a technological lag before the first experimental realization in 1990,[9] which was facilitated by the advent of mode-locked lasers with sub-picosecond pulsewidths and repetition rates on the order of 100 MHz.[8] This improves the TPE efficiency by several orders of magnitude, as the probability, n_a , that a dye molecule absorbs two photons per pulse is approximated as

$$n_a = \frac{p_0^2 \delta}{\tau_p f_p^2} \left(\frac{NA^2}{2hc\lambda} \right)^2 \quad (2.1)$$

where p_0 is the average power, δ is the two-photon absorption cross-section, τ_p is the pulse width, f_p is the pulse repetition rate, and NA is the numerical aperture of the incident beam.[9]

Two-photon fluorescence imaging enables the non-destructive, 3D interrogation of samples (Fig. 2.3). It is competitive with confocal microscopy for many biological specimens as it uses near infrared wavelengths, where these samples are typically transparent. Further the localized excitation enables imaging within highly scattering specimens.



Figure 2.3 Overlay of two- (red and green) and three-photon (blue) fluorescence images of a *C.elegans* embryo.[12]

The diffraction-limited TPE volume has also been utilized to initiate polymerization in order to fabricate high resolution three dimensional structures (Fig. 2.4). Due to the presence of a polymerization threshold in these systems, sub-diffraction limited feature generation is possible,[13] with lateral dimensions as small as 100 nm, reported.[14] Two-photon polymerization (TPP) has been used to define a variety of high resolution 3D free-form structures, including: microchannels,[15-17] cantilevers,[18-20] microgears,[13,21] submicron oscillators,[22] atomic force microscopy tips,[23] and photonic crystals.[19,24-33] Additionally, we, and now more recently others, have demonstrated TPP writing of embedded features within self-assembled photonic crystals.[1,34] TPP is additionally interesting because it can be used to define features within holographic photonic crystals (see Chapter 5).[35,36]

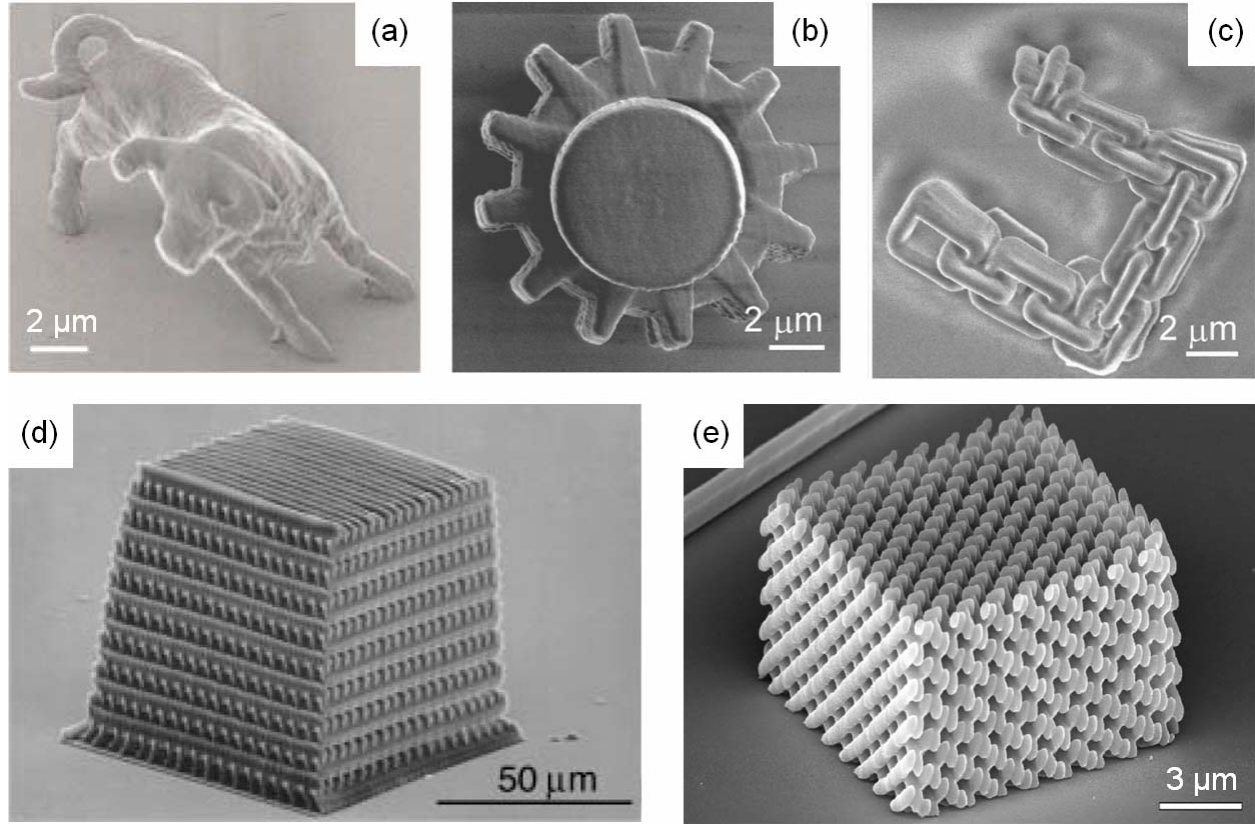


Figure 2.4 SEM micrographs of (a) micro-bull,[37] (b) micro-gear,[13] (c) micro-chain,[13] (d) layer-by-layer photonic crystal structure,[19] and (e) slanted pore photonic crystal[31] fabricated via TPP.

2.3 Point-by Point Exposure

Point-by-point exposure is often employed for the TPP of voxels (volume elements), either overlapping to create a 3D structure or isolated to reveal individual resolution elements (Fig. 2.5a).[13] A polymerization threshold is apparent in Figure 2.5a. At low power voxels are not formed, while with increasing power, voxels of increasing dimensions are polymerized (Fig. 2.5b). Finally, at high power, damage is clearly apparent. The onset is distinct and experimentally reproducible, so it can easily be avoided. Such damage[18,19,21,26,33,38-40] and boiling[21,26,41] are regularly observed in TPP systems.

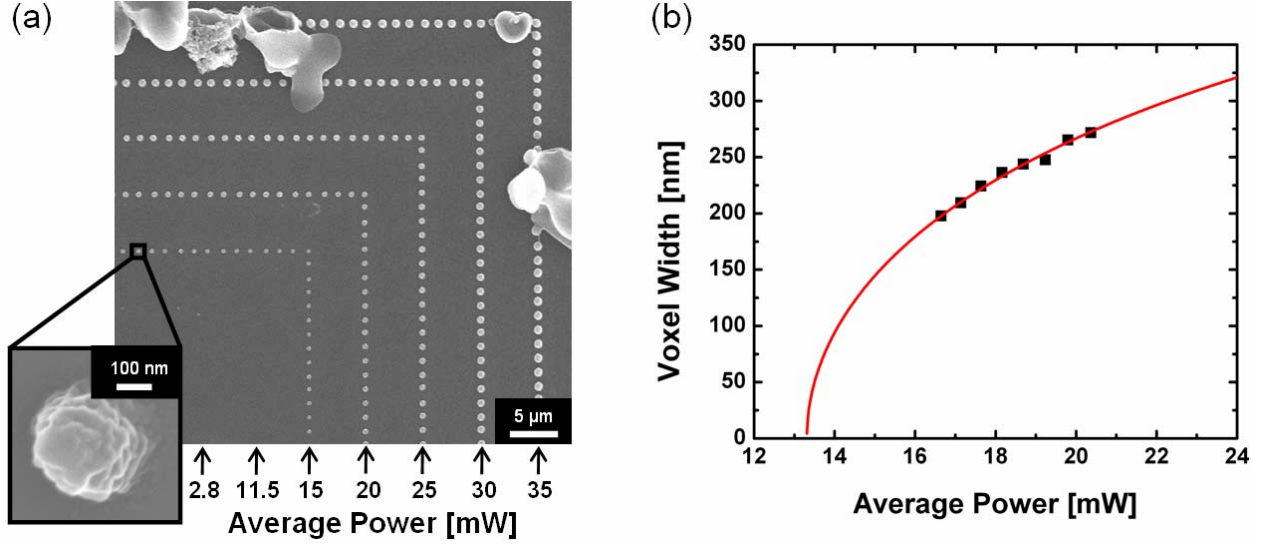


Figure 2.5 (a) SEM of TPP voxels written with point-by-point exposures at various incident powers. The damage that extends into the row of voxels written with 30 mW is from the 35 mW exposures. Confocal micrographs taken directly after polymerization confirm this; such damaged regions often fall over upon drying after rinsing to remove excess monomer. (b) Voxel width as a function of incident power for a similar set of point-by-point exposures. Care was taken to ensure that greater than half of each voxel was protruding from the substrate to obtain valid diameter measurements. The black squares represent the averages of measurements from approximately five voxels per average power. The solid line corresponds to the best fit for the data using equation 2.2.

The TPP threshold has been previously identified as the local absorbed energy density below which polymer will not form.[42] Using the same approach as Martineau *et al.*,[42] an expression was derived for the dependence of lateral feature width, W , on the time-averaged incident power, $\langle P(t) \rangle$, for a fixed exposure time of 1 ms (see Appendix 2),

$$W = \omega_0 \sqrt{2 \ln \left(\frac{\langle P(t) \rangle}{\langle P(t) \rangle_{\min}} \right)} \quad (2.2)$$

where ω_0 is the lateral width of the Gaussian intensity distribution in the focal plane and $\langle P(t) \rangle_{\min}$ is the minimum power required for TPP, corresponding to infinitesimally small feature generation. Thus, experimentally identifying $\langle P(t) \rangle_{\min}$ as the power at which polymer is first observed will result in an overestimation. It is more desirable to determine $\langle P(t) \rangle_{\min}$ by fitting a plot of the feature width versus the average power with equation 2.2 as shown in Figure 2.5b.[42] $\langle P(t) \rangle_{\min}$ and ω_0 were determined in this fashion to be 9.1 mW and 393 nm, respectively. The absorbed energy density of the polymerization threshold, E_{th} , for our system was then determined to be $3.07 \text{ nJ } \mu\text{m}^{-3}$, using an equation derived by the same approach as Martineau *et al.*[42] (see Appendix 2),

$$E_{th} = \tau_{\text{exp}} N_i \frac{\sigma_{TPA}}{\hbar\omega} \frac{4}{\pi^2 \omega_0^4} \frac{g_p}{\tau_p F} \langle P(t) \rangle_{\min}^2 \quad (2.3)$$

where τ_{exp} is the exposure time (1 ms), N_i is the number density of the initiator ($5.082 \times 10^{17} \text{ cm}^{-3}$), σ_{TPA} is the two-photon cross-section of the initiator ($1.523 \times 10^{-48} \text{ cm}^4 \text{ s photon}^{-1}$),[43] $\hbar\omega$ is the energy per photon ($2.548 \times 10^{-19} \text{ J photon}^{-1}$), g_p is a dimensionless quantity to account for the pulse shape (0.588),[44] τ_p is the temporal pulsewidth (100 fs), and F is the repetition rate of the laser (82 MHz).

2.4 Modulated Beam Rastering

While point-by-point exposures are very useful for writing individual volume elements, the utility of TPP is in the ability to fabricate high resolution 3D structures. These structures can be realized by writing a series of overlapping voxels point-by-point, however generally it is more desirable to continuously translate either the beam or sample. Continuous writing enables faster formation of features and affords potentially higher edge resolutions for thin lines. Typically

scanned writing is either accomplished on a custom-built system incorporating a galvanometer mirror scanning system and/or a translation stage or with a conventional laser scanning confocal microscope (LSCM) equipped for multi-photon polymerization.[1,10,15,45-47] Advantages of using a LSCM include the commercial availability as well as the capability to obtain high resolution images of TPP features during or directly after polymerization.

Previous LSCM implementations that employed a scanning mirror system had the drawback of being restricted to the definition of lines and boxes.[15,46] The modulated beam rastering approach we introduced involved coupling a standard multi-photon LSCM with an electro-optic modulator (EOM) (Fig. 2.6).[1] The LSCM is operated in the standard fashion where a galvanometer mirror scanning system is employed to raster a laser throughout a particular scan volume. During the scan, the EOM modulates the laser beam between a high and low setting, enabling the selective polymerization of a particular region of interest (ROI) within the scan volume. We operate at scan speeds up to 19 cm s^{-1} , thus it is important that the response time of the EOM ($\sim 12 \text{ ns}$) be fast enough not to impact feature resolution. The beam translates less than 2.3 nm in 12 ns , thus the EOM response time does not limit edge resolution.

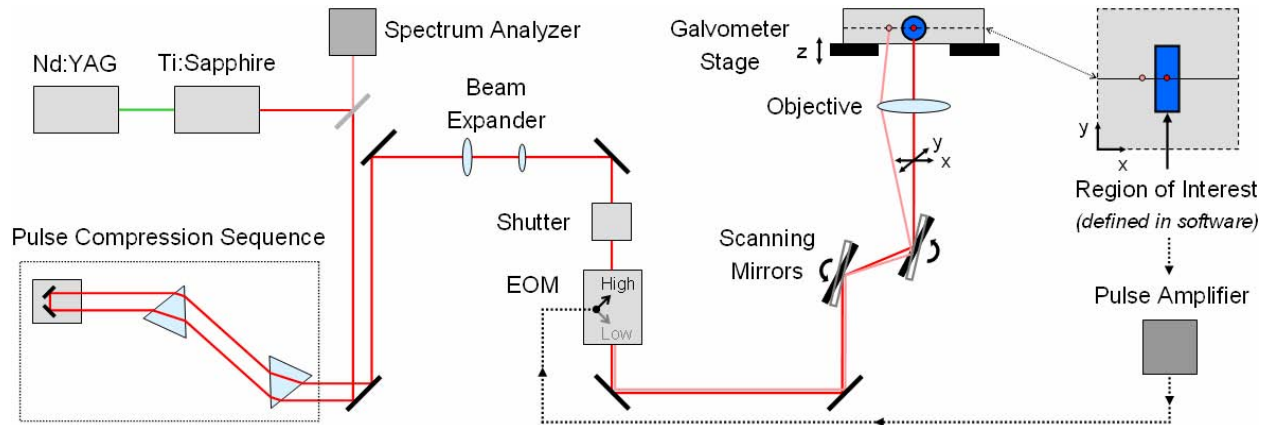


Figure 2.6 Schematic of multi-photon LSCM setup used for TPP and imaging.

In our system, the laser beam is scanned throughout a particular volume by rastering the beam in the lateral dimensions using a two-point scanning mirror system and by translating the sample in the transverse dimension using a galvometer stage (Fig. 2.6). ROIs are defined in the microscope software and communicated to the EOM during the raster scanning. The EOM attenuates the power of the beam significantly when scanning outside the ROI (Fig. 2.7, solid line), while allowing for control of the power through the gain setting when scanning within the ROI (Fig. 2.7, squares).

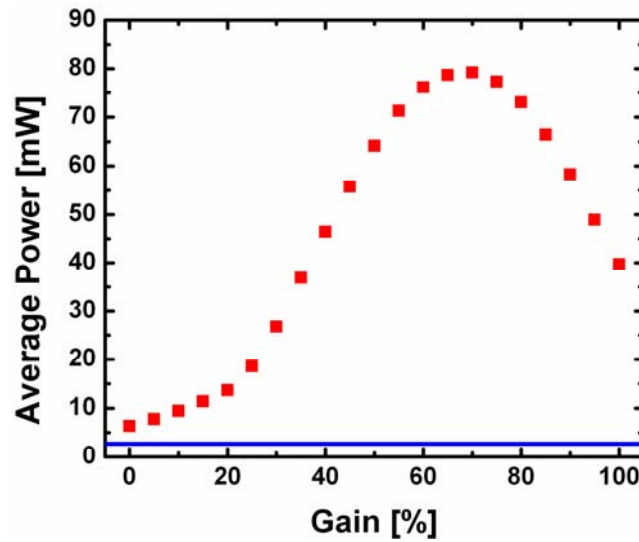


Figure 2.7 Typical average power measured at the objective as a function of percent gain, plotted for operation at both the high (red squares) and low (solid blue line) settings on the EOM.

The ROI consists of geometric shapes defined in either a horizontal or vertical slice which is then scanned through the transverse dimension in order to write a 2D feature. Horizontal (vertical) features with dimensions up to $\sim 238 \times 238 \mu\text{m}^2$ ($\sim 125 \times 125 \mu\text{m}^2$) are polymerized in ~ 2.6 s per slice, enabling features with a thickness of about $10 \mu\text{m}$ to be written in two minutes. The features in Figure 2.8 were polymerized with the modulated beam rastering technique using a circular ROI defined in a horizontal slice which was scanned through the

transverse dimension. A combination of 2D ROIs written in multiple slices can be used to generate 3D features with simple uniform 2D cross-sections. This implementation is not useful for writing arbitrarily complex 3D structures, however for many scientifically interesting studies, features with simple cross-sections are sufficient.

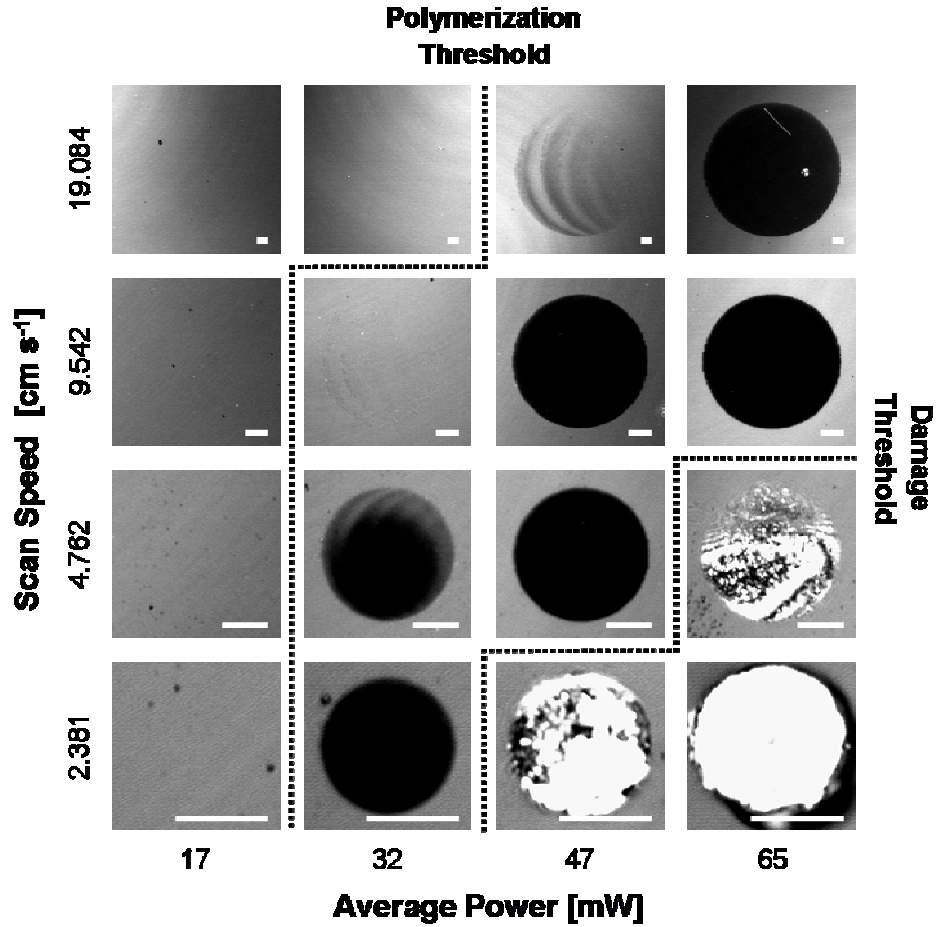


Figure 2.8 Reflectance confocal micrographs of 10 μm thick TPP features written with a circular ROI in the modulated beam rastering mode for different scan speeds and average powers. We operate just below the damage threshold to define TPP features. All scale bars are 5 μm . [2]

A significant advantage of performing TPP on a confocal microscope is the ability to image the TPP features during or directly after their definition. For example, the images in Figure 2.8 are reflectance confocal micrographs taken from the interface of the monomer or

polymer with the substrate using 633 nm radiation. This wavelength is not absorbed by the initiator, monomer, or polymer, and therefore does not influence the polymerization. The image contrast is from the different reflectivities of the interfaces in the system due to refractive index disparities. Since the polymer has a closer refractive index to the coverglass substrate than the monomer, the TPP features appear dark. Damage shows up bright due to the large refractive index contrast between the bubbles created during damage and the surrounding media. The concurrent imaging capability is useful in the identification of damage, enabling premature abortion of scans to prevent damage from spreading to other regions of the sample, which is useful since we operate just below the damage threshold to write dense features (Fig. 2.8).

Since the beam is rastered throughout the same scan area regardless of the defined ROI(s), it is optimal to operate where the scan size is minimally larger than the defined feature to afford faster writing times or maximum resolution. It is possible to increase the resolution by maintaining the same number of lines per scan while decreasing the overall scan area. This is because the primary limit to feature resolution is aliasing imposed by the software,[48] whereby the edges of the ROI are defined on a discrete grid, with the grid size approximately equal to the scan dimension over the number of lines per scan (Fig. 2.9).

To obtain the maximum edge resolution it is optimal to operate where the scan dimension is just larger than the feature being written. In this fashion, ROIs with edge resolutions approximately 1/2000 the overall ROI dimension can be defined in the software, with the minimum grid element size being about 3.6 nm (corresponding to the minimum possible scan size, $7.44 \times 7.44 \mu\text{m}^2$, and maximum number of lines per scan, 2048). The minimum resolution element is significantly larger, on the order of 100 nm, thus, aliasing generally does not limit resolution assuming the proper scan size and number of lines per scan are used.

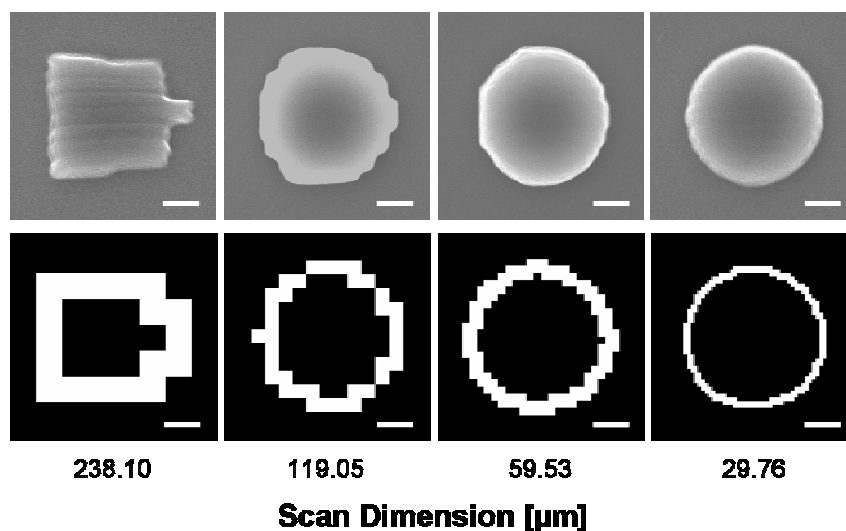


Figure 2.9 Scanning electron micrographs (top) of features written with different overall lateral scan dimensions. All of the features were specified to be 3.75 μm diameter circles, however software aliasing limits the feature resolution by defining the edges of the ROIs (bottom) on a grid with a pitch approximately equal to the overall scan dimension over the number of lines per scan (512 was used here). Scale bars are 1 μm.[2]

2.5 TPP Response Diagrams

Typically a series of graphs of voxel or line width as a function of exposure conditions (for example, Fig. 2.5b) can be used to map the TPP response,[13,28,37,39,41,42,47,49] however this is not suitable for operation in modulated beam rastering. Here, the subsequent lines and possibly scans overlap the same volume within a radical lifetime, (typical values range ~0.1 to 10 s).[50] Therefore, a practical alternative was employed, and we developed a TPP response diagram to map the polymerization response for modulated beam rastering as a function of the relevant parameters. This was accomplished by constructing a grid of points (in scan speed and power squared) and identifying each point by its response (no feature, polymerization, or damage) (Fig. 2.10). Conditions that result in one or more bubbles during the scan are identified as above the damage threshold, with distinction made based on whether damage

exhibits runaway. The resulting TPP response diagram enables the visualization of the polymerization window affording the reliable operation below the damage threshold during feature definition. The utility in understanding the TPP behavior in terms of both scan speed and power becomes apparent when considering the details of the modulated beam rastering setup. The scan dimension optimally scales with the TPP feature size to realize the best resolution (Fig. 2.9). Here the scan frequency is kept constant, so the scan speed scales directly with the scan dimension. So as the feature size (scan dimension) is changed, one moves vertically within the TPP response diagram (Fig. 2.10), possibly passing through the polymerization window. Therefore it is necessary to adjust the power as the feature size is changed in order to elicit the same polymerization response (Fig. 2.8), making TPP response diagrams very useful in the reliable definition of high resolution features.

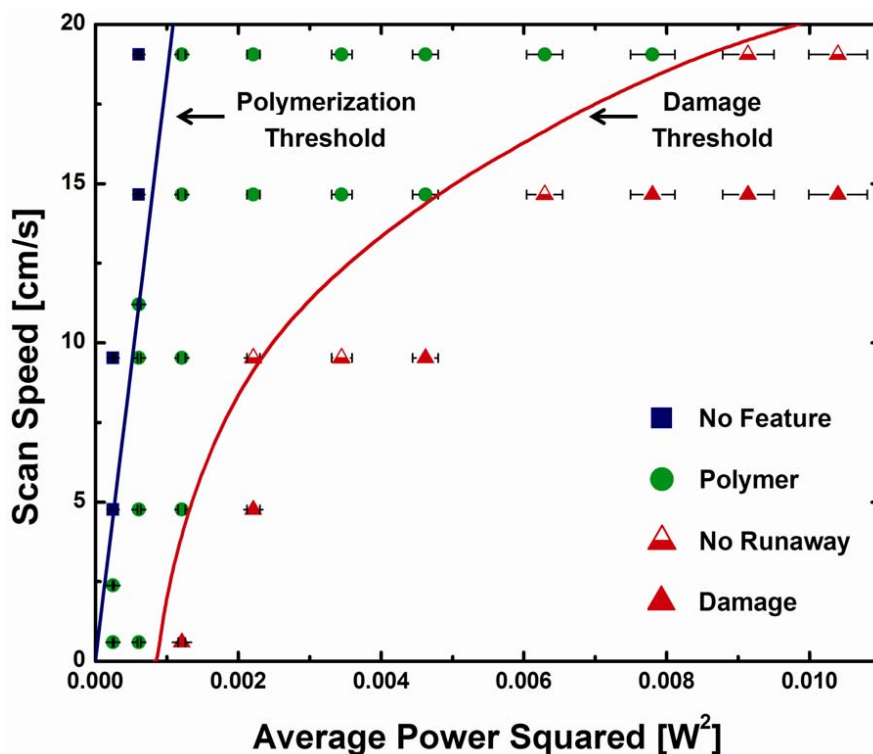


Figure 2.10 TPP response diagram for 0.1 wt.-% AF-350 in TMPTA. The TPP threshold was calculated to fit the data; the damage threshold was drawn to guide the eye.[2]

2.5.1 TPP Within and Outside of a Colloidal Crystal

TPP response diagrams afford the visualization of the polymerization window enabling the comparison between TPP conditions, for example, the operation within as compared to outside of a colloidal crystal. The behavior in a colloidal crystal is of interest as TPP may be a valuable technique to write optically interesting features within self-assembled photonic crystals.[1,34] Therefore, it is possible to compare the TPP response diagram (Fig. 2.10) for 0.1 wt.-% AF-350 in TMPTA (Fig. 2.11) with that for the same solution in a colloidal crystal.

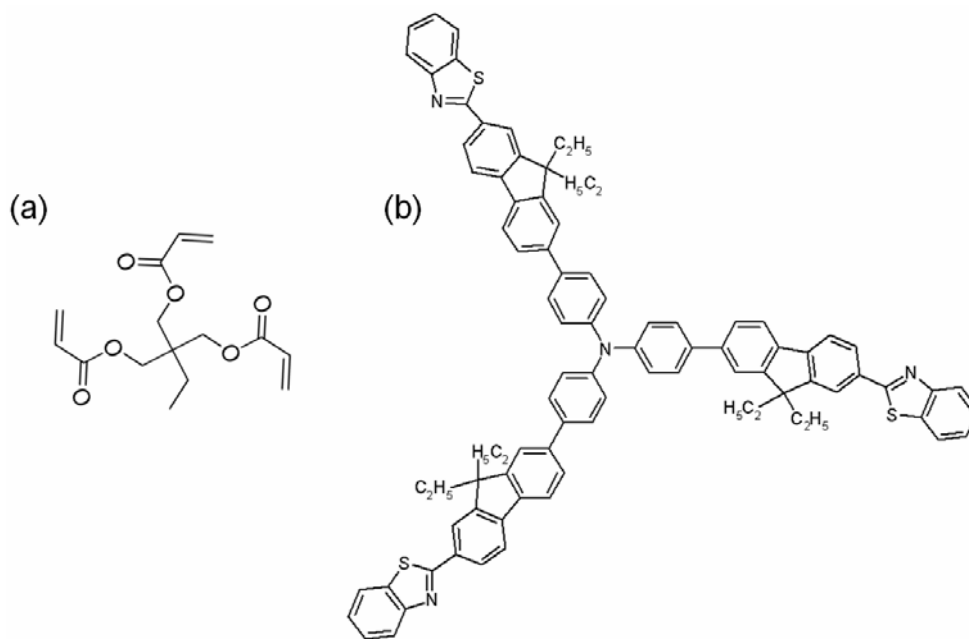


Figure 2.11 (a) Monomer, TMPTA (trimethylolpropane triacrylate) and (b) initiator, AF-350 (tris[4-(7-benzothiazol-2-yl-9,9-diethylfluoren-2-yl)phenyl]amine).[43]

In this fashion, it was determined that the TPP response within a colloidal crystal (Fig. 2.12) is very similar to that of the same solution in bulk (Fig. 2.10). The polymerization thresholds are nearly the same and the damage thresholds are similar. Discrepancies may be partially attributable to the greater uncertainty in damage identification in a colloidal crystal. Although the refractive indices of the monomer and colloids are within ~5%, some scattering is

present, which contributes to background noise in the images taken within a colloidal crystal. Severe damage is still very easily recognized and there is sufficient contrast to distinguish the polymerized regions from the monomer. However, small spots of damage are not as easily distinguished from the background, so it is possible that some of the points close to the damage threshold have been misidentified. It is also possible that the different thermal conductivity of the colloidal crystal versus the monomer could contribute to a difference in the damage response. The overall similarity of the TPP response within and outside of a colloidal crystal indicates that the colloidal crystal does not greatly impact the polymerization response, which is convenient because it allows the initial study of TPP systems outside colloidal crystals, where imaging is simpler.

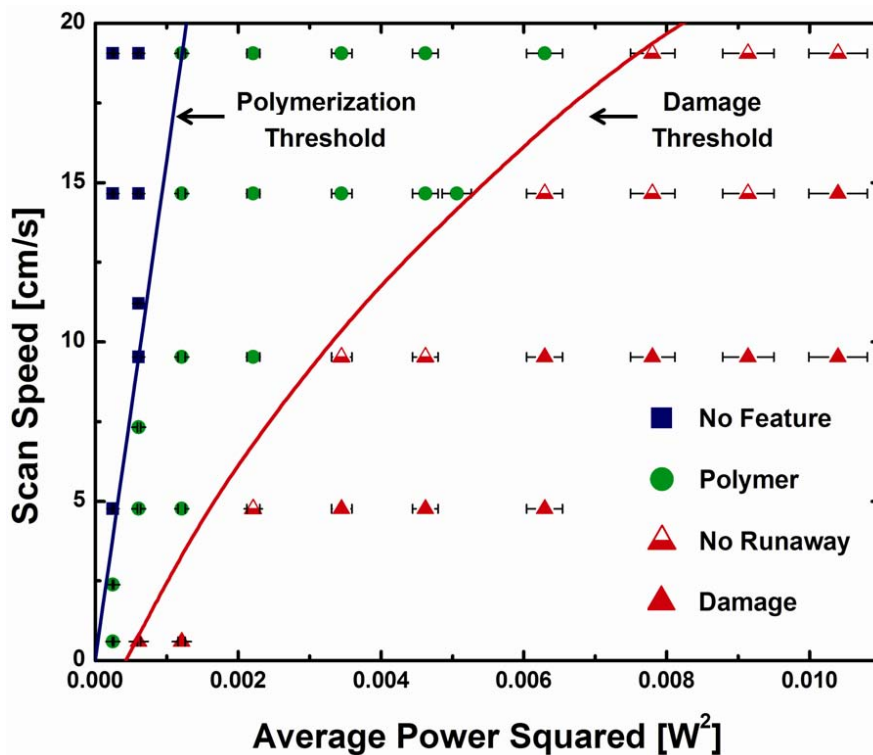


Figure 2.12 TPP response diagram for 0.1 wt.-% AF-350 in TMPTA in a colloidal crystal. The polymerization threshold was calculated to best fit the data, while the damage threshold was drawn to guide the eye.[2]

2.5.2 Initiator Efficiency Comparison

Response diagrams were also used to demonstrate that AF-350 is a much more efficient initiator than our previous initiator system, a literature recipe for a three-photon polymerizable resin based on the same monomer, TMPTA.[15] Further, it is interesting how similar this response diagram (Fig. 2.13a) is to that for the neat monomer, TMPTA, (Fig. 2.13b) where damage occurs even in the absence of a TPP initiator. Surprisingly, feature generation is occasionally possible even in the inefficient system, though there is not a clear polymerization window. Sometimes damage does not deviate significantly outside the boundaries of the ROI, occasionally enabling feature generation, however the reproducibility is extremely low (Fig. 2.14). The high frequency of damage observed with this system was originally attributed to the lack of control over scan parameters and may not have always been identified due to limitations in previous in situ imaging ability. However, it is clearly important to obtain an efficient system such as AF-350 in TMPTA with a relatively large TPP window in order to reproducibly define high resolution features within and outside of colloidal crystals.

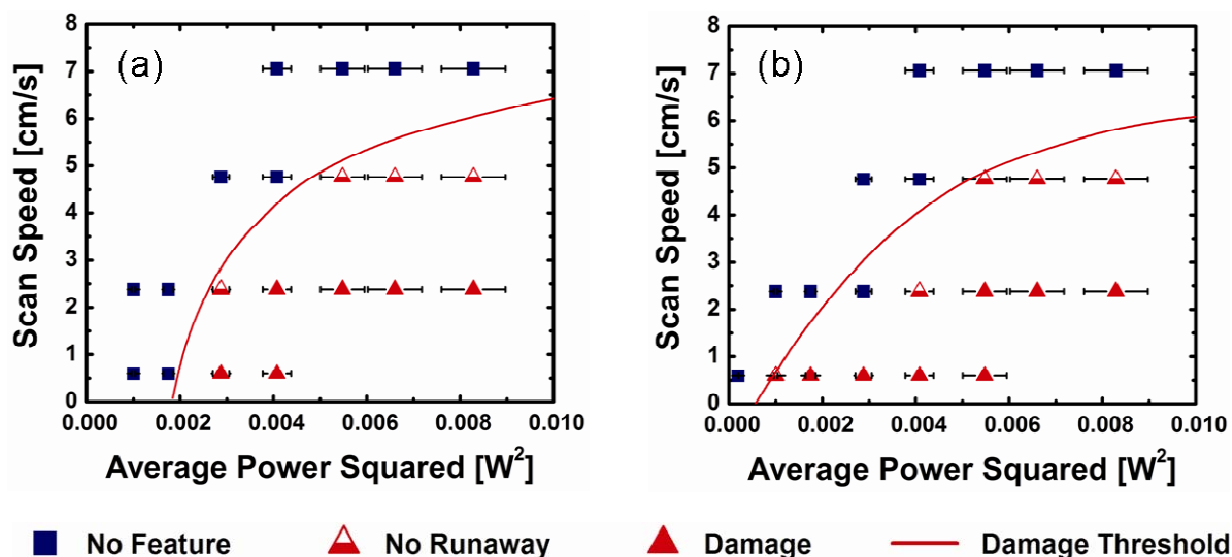


Figure 2.13 Multi-photon polymerization response diagrams for (a) inefficient initiator system and (b) TMPTA monomer. Damage thresholds were drawn to guide the eye.[2]

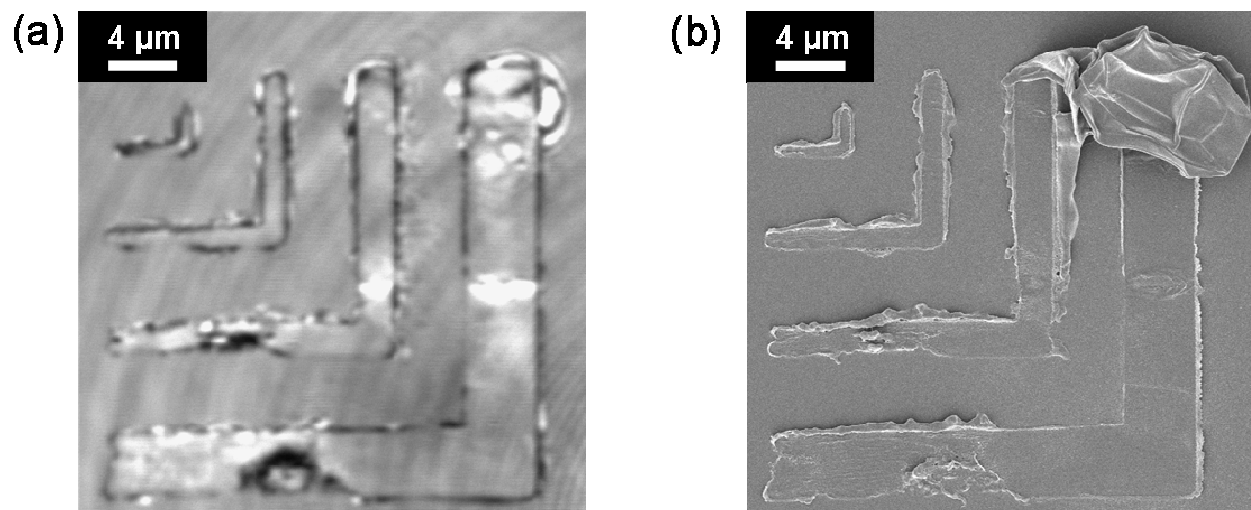


Figure 2.14 (a) Reflectance confocal micrograph and (b) scanning electron micrograph of a typical attempt to define features with the inefficient multi-photon polymerization system. Striations apparent in the confocal micrograph result from a slight interference in the optics.

2.6 Microscopy of TPP Features

SEM enables the verification of high resolution TPP feature definition both within and outside of colloidal crystals (Fig. 2.15) and the identification of diffuse damage, which can be difficult to observe in colloidal crystals via confocal microscopy. Because the response diagrams map out the reproducible TPP response, it is not necessary to perform SEM on every sample once it is confirmed that high resolution features are consistently achieved for operation within the polymerization window. This is appealing as it is necessary to remove the colloids to directly image the TPP features, preventing further use of the sample.

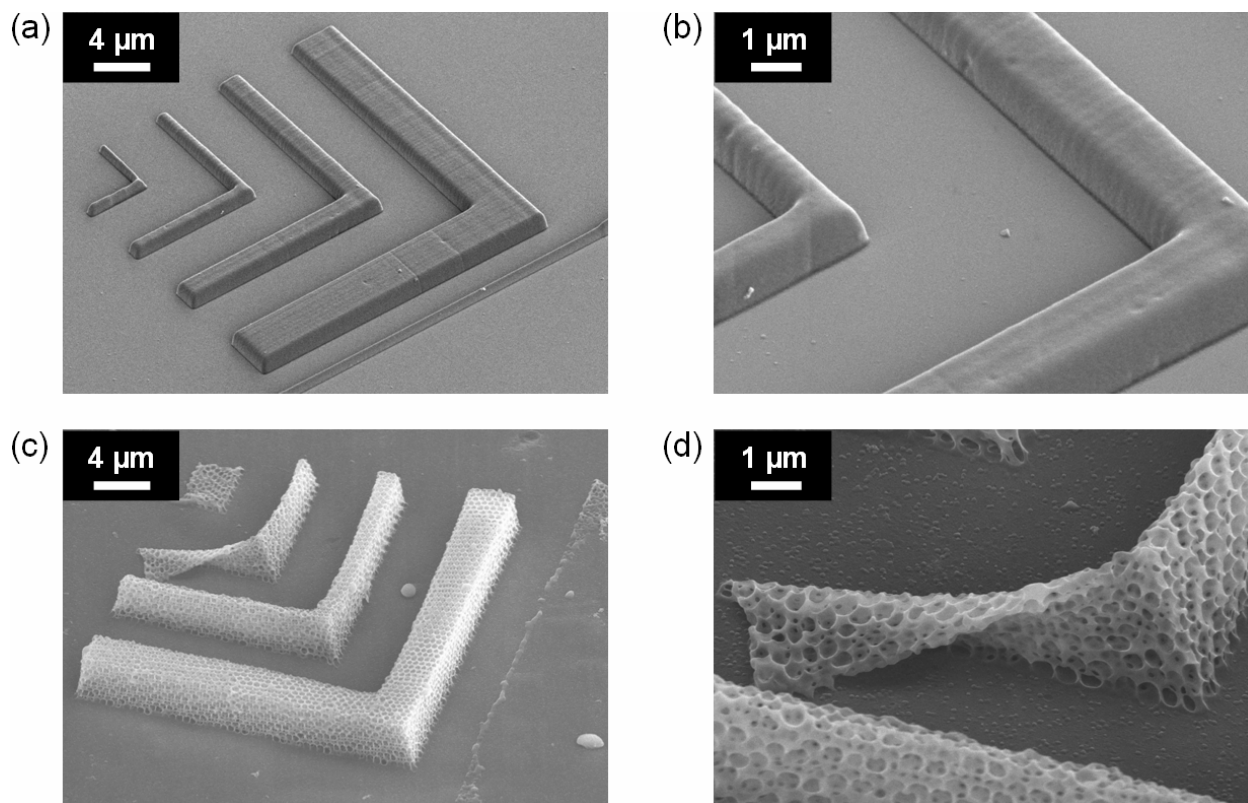


Figure 2.15 SEM images of TPP features written (a) in bulk AF-350:TMPTA on a coverslip and (b) within a colloidal crystal after removal of the silica via an aqueous hydrofluoric acid etch.

The colloidal crystal provides a support network for features which might not otherwise remain free-standing, thus SEM is not appropriate for accurate 3D representations of some structures. For example, in Figure 2.15 c and d, some portions of the thin features fall over upon removal of the colloidal crystal. Fluorescence confocal microscopy enables the non-destructive imaging of non-self-supporting 3D TPP features written within colloidal crystals (Fig. 2.16). This was initially accomplished by removing unpolymerized monomer and backfilling with a dye solution, followed by imaging on the same microscope used to write the features (Fig. 2.17). However, the addition of an appropriate dye in the monomer solution can enable in situ fluorescence imaging within an undeveloped TPP resin (Fig. 2.18).[36,51] This facilitates 3D

alignment of defects with respect to the photonic crystal lattice, which will be important for the definition of functional features.

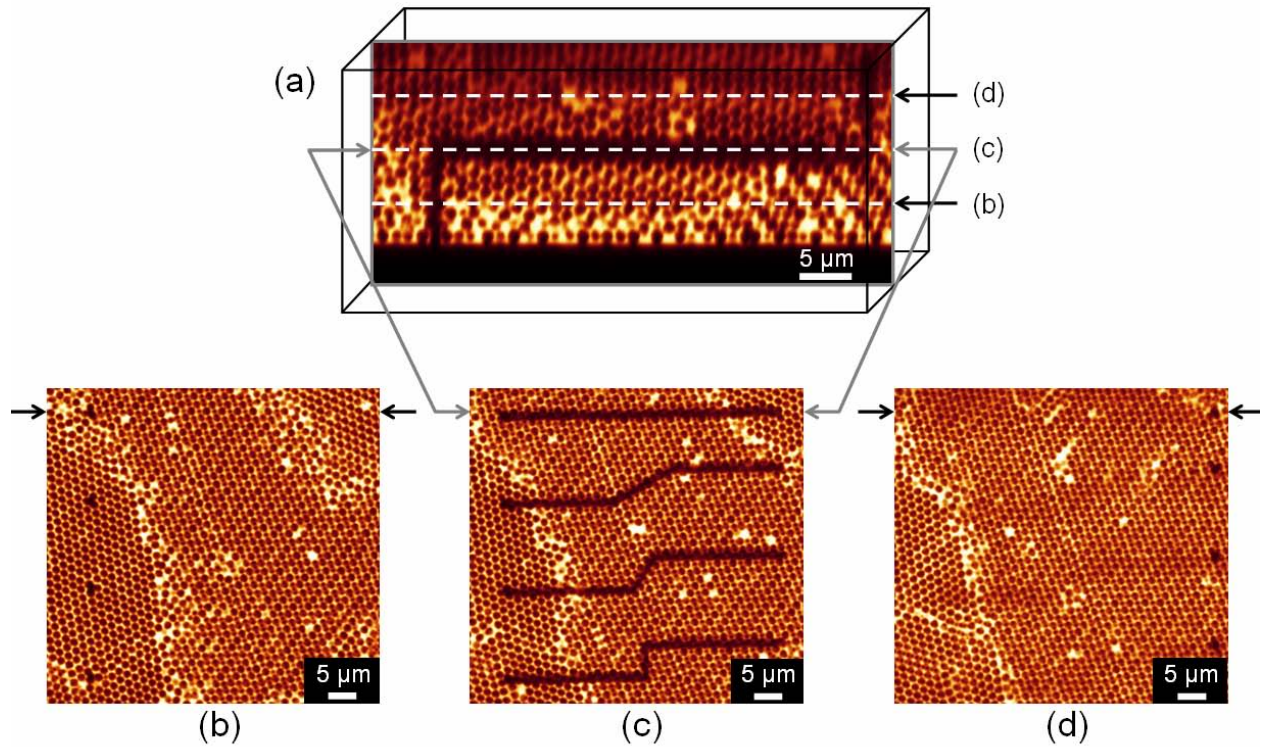


Figure 2.16 Fluorescence confocal micrographs of cross-sections from 3D TPP features written within a colloidal crystal. Four features were defined—one is a 2D double-bend structure and three are 3D triple-bend structures with varying bend angles in the horizontal plane. (a) Vertical cross-section through the 2D double bend structure. The arrows indicate the location of the horizontal cross-sections presented in (b-d). The lower images are horizontal cross-sections through the: (b) vertical components of the four features extending $\sim 10\ \mu\text{m}$ from the substrate into the crystal, (c) horizontal components containing 0° , 30° , 60° , or 90° bends, and (d) vertical components extending $\sim 10\ \mu\text{m}$ further into the colloidal crystal. The arrows in b-d indicate the location of the vertical cross-section (a).[2]

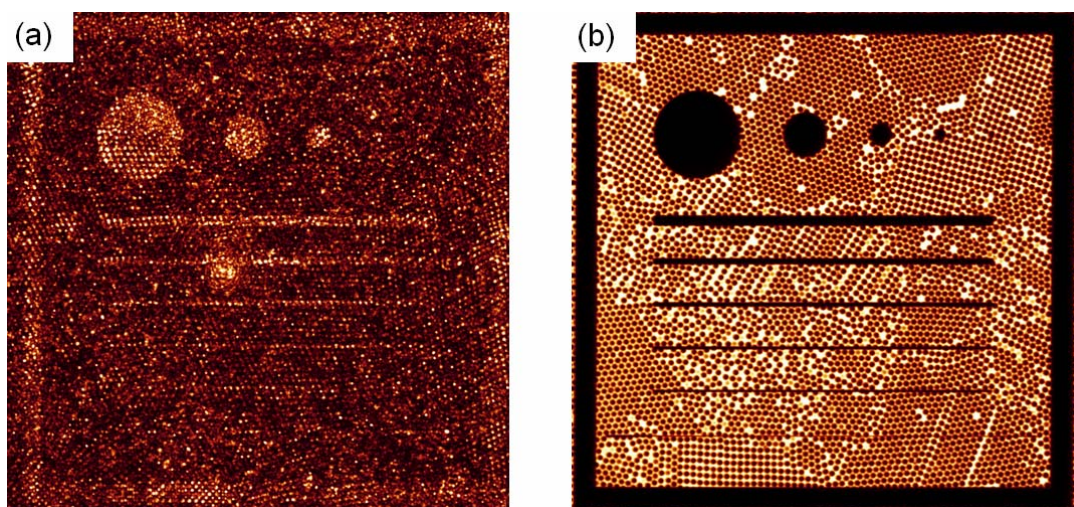


Figure 2.17 (a) Reflectance and (b) fluorescence confocal micrographs taken after TPP of a series of features. Clearly there is a large disparity in the resolution of the colloidal crystal quality between the two micrographs. Colloidal crystal was sedimented from silica microspheres $\sim 1.57 \mu\text{m}$ in diameter.

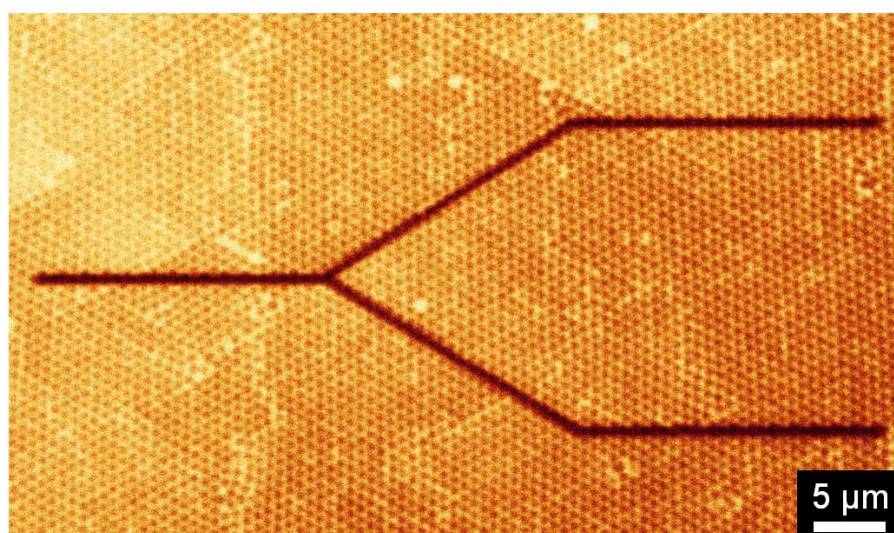


Figure 2.18 In situ fluorescence confocal micrograph taken directly after TPP in the same resin used for polymerization. TPP feature shows up dark because the two-photon exposure also bleaches the fluorescent dye. Polymerization of that region was confirmed via SEM in a later processing step. Note the nice registration of the feature with the underlying lattice, which was not previously possible using in situ reflectance mode imaging (Fig. 2.17).

2.7 Spectroscopy from TPP Features

Optical spectroscopy was collected from a 16-20 layer colloidal crystal containing a 40 μm diameter vertical cylindrical TPP feature running from the bottom to top of the colloidal crystal. This feature is formed by scanning a circular ROI defined in a horizontal slice through the thickness of the crystal (Fig. 2.19a). Spectra are taken from the colloidal crystal as formed (Fig. 2.19a, i) and then after growing a thin silica layer around the colloids via low pressure chemical vapor deposition (CVD) of silicon followed by thermal oxidation (Fig. 2.19a, ii). Spectroscopy is additionally collected from within the 40 μm diameter TPP feature (Fig. 2.19a, iii). The experimental data is compared with simulated spectra calculated for normal incidence using a layered-KKR approach (Fig. 2.19b).[52,53] We previously demonstrated for low index contrast photonic crystals, that it is valid to compare normal incidence spectra calculated using layered-KKR approach to spectra collected experimentally using a low numerical aperture objective on the same micro-spot spectroscopy setup (see Section 1.4).[54] There is good agreement between experiment and theory with respect to the relative trends in both peak position and peak reflectivity. The $\sim 3\%$ discrepancy in the peak position between experiment and theory after CVD is reasonable considering, for example, the error in estimating the filling fraction and refractive index of the silica. The discrepancy for all spectra in the maximum reflectivities between experiment and theory is commonly observed in literature.[55-57] The nonzero background reflectance is due to the silicon substrate used both experimentally and when calculating spectra.

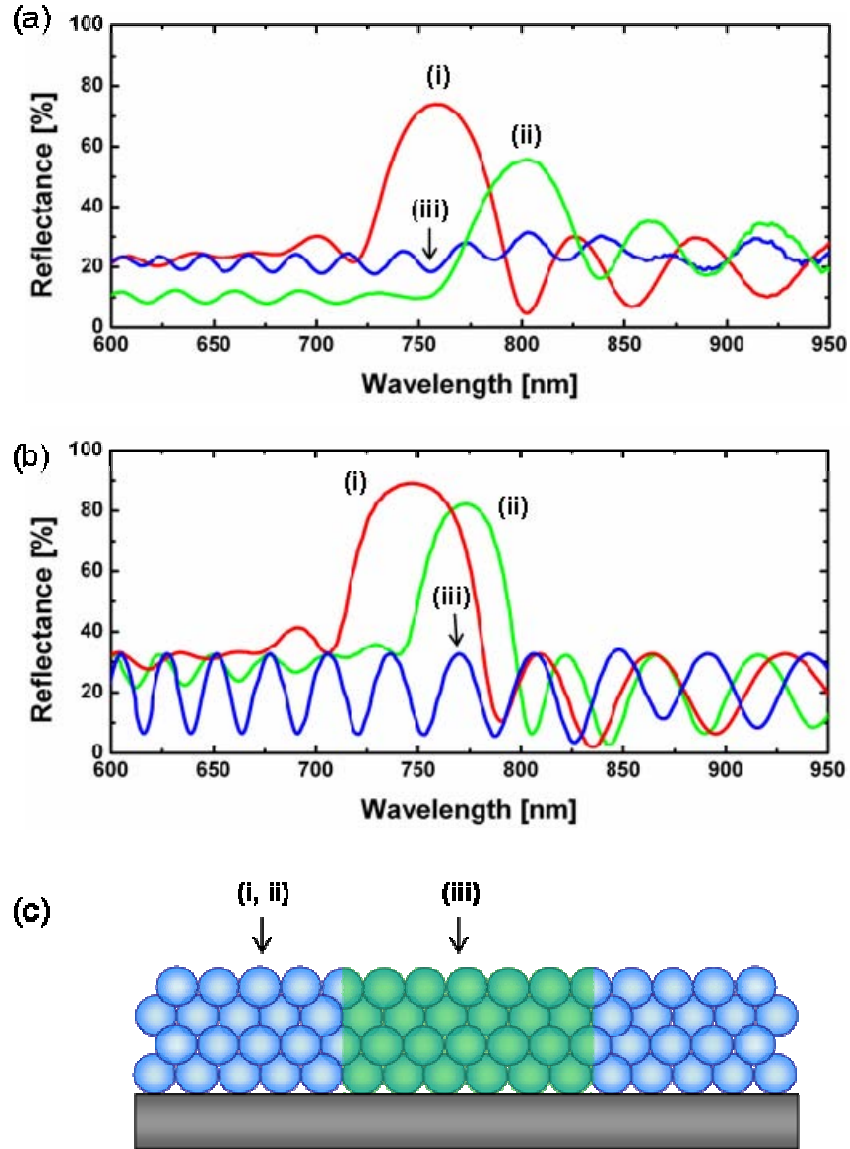


Figure 2.19 (a) Experimental and (b) simulated reflectance from a 16-20 layer colloidal crystal (i) as grown and (ii) after growing a thin layer of silica on the colloids. (a, iii) Reflectance collected from a 40 μm diameter vertical cylindrical feature written via TPP through the thickness of the same colloidal crystal. (b, iii) Simulation done for comparison was calculated for a silica colloidal crystal completely infiltrated with poly(TMPTA); this is appropriate since the experimental data (a, iii) was collected only from within the TPP feature. (c) Schematic of a vertical cross-section through colloidal crystal containing a TPP feature, indicating the regions from which spectroscopy was collected.

The ~70 % absolute reflectivity as grown indicates that the colloidal crystal is of high quality (Fig. 2.19a, i). When a thin silica layer is grown on the colloids (Fig. 2.19, ii), the peak redshifts due to the increase in the overall refractive index of the crystal due to the greater filling fraction of silica. The peak intensity decreases upon growing the silica layer as expected as the filling fraction is increased toward the case of homogeneous silica. A diffraction peak is not apparent in the spectrum collected from the 40 μm diameter TPP feature written within the colloidal crystal on account of the low refractive index contrast between poly(TMPTA) and silica (Fig. 2.19a, iii). This is also apparent in the simulation calculated for a silica colloidal crystal completely infiltrated with poly(TMPTA) (Fig. 2.19b, iii). It is valid to compare the simulated spectra with the experimental data from the TPP feature as the spectrometer enables collection from sampling spots on the order of 10-15 μm .

Optical spectroscopy verifies that the colloidal crystal quality is maintained during the processing steps necessary for TPP (i.e. filling with pre-polymer solution, rinsing away excess monomer, and TPP of features). Spectroscopy also confirmed for the first time the successful polymerization of a uniform, dense polymer feature throughout the thickness of the colloidal crystal.

2.8 Conclusions

In this chapter, a modulated beam rastering technique for the TPP of embedded features within self-assembled photonic crystals was described. This approach utilizes a commercially available laser scanning confocal microscope to rapidly write relatively large area 3D features composed of simple 2D cross-sections, while affording in situ imaging capability. Further, a TPP response diagram was introduced and developed to visualize the polymerization and

damage thresholds for modulated beam rastering, enabling the reliable reproduction of high resolution, damage-free features. TPP response diagrams were used to interrogate the impact of the initiator efficiency and the surrounding environment on the TPP response. It was demonstrated that AF-350 is an efficient initiator for TPP and it was confirmed via electron microscopy that TPP within and outside of a colloidal crystal afford similar TPP response and feature resolution. This facilitates the direct extension to TPP within colloidal crystals, which is relevant as TPP has been identified as an attractive technique for the fabrication of embedded defect structures within self-assembled photonic crystals.[1,34] The incorporation of defects is important as it extends the viability of this class of photonic crystals to include the majority of PBG applications. Fluorescence confocal micrographs of 3D non-self-supporting features embedded within self-assembled photonic crystals were presented. Spectroscopy from a TPP feature written within a self-assembled photonic crystal was presented and compared with simulation. In Chapter 3, the replication of these structures in a high index material capable of imparting a cPBG will be discussed. Chapter 4 will cover spectroscopy from colloidal photonic crystals with embedded defects.

2.9 Experimental

2.9.1 Confocal Instrumentation

Multi-photon polymerization and confocal imaging were performed on a laser scanning confocal microscope (Leica, DMIRBE microscope and SP-2 scanhead) outfitted for multi-photon operation with an electro-optic modulator (Linco, LM0202 5W KD*P) and a Ti:sapphire laser (Spectra Physics Tsunami, ~60 fs pulses, 82 MHz repetition rate) operated at a wavelength of 780 nm (Fig. 2.6). The confocal microscope is maintained in accordance with the guidelines

laid out by Hibbs *et al.*[58] A pulse-dispersion pre-compensation sequence was employed in the path of the laser before coupling to the microscope to offset the positive group velocity dispersion imparted by the optics.[59] The estimated pulsewidth at the objective was ≤ 100 fs. The temporal and spectral pulsewidths and pulseshapes were not measured prior to each experiment; since these parameters affect the efficiency of two-photon processes,[60] this may contribute to experimental variability. To minimize variability, the response diagrams which were directly compared (Fig. 2.10 and 2.12; as well as Fig. 2.13a and 2.13b) were taken during the same sessions.

The 633 nm line of a HeNe laser was used for reflectance confocal imaging during and directly following polymerization and the 514 nm line of an argon ion laser was employed for the fluorescence confocal imaging. All experiments were carried out using a 63x oil-immersion objective (Leica) with a numerical aperture (NA) of 1.32. The scan parameters used for construction of the TPP response diagrams were defined in the microscope software as: 1024 x 1024 scan format (resolution); 400 Hz scan frequency; no beam expander; unidirectional scanning; no line or frame averaging; and 50 slices for a series scan with a depth of 10 μ m. The scan speed is equal to the overall scan dimension multiplied by the scan frequency, where the scan dimension used in constructing the TPP response diagrams was twice the feature (ROI) dimension. The exposure times for the point-by-point exposures were regulated with an electronic shutter. The power in all experiments was modulated via the gain on the EOM.

2.9.2 Power Measurements

Prior to each experiment, an optical power meter (Newport, 1830-C) was used to measure the incident average power for the low setting on the EOM (with the offset optimized) and then

for the high setting as a function of the percent gain of the EOM (from 0 to 100 % at 5 % increments) using the point-bleach software functionality (Fig. 2.7). Due to geometrical constraints, the power meter was unable to collect all of the light emerging from the 63x objective used in the experiments, therefore the power was measured at the exit of a 0.70 NA 20x objective (Leica). This captures relative changes in power, although there may be minor errors in the actual power due to differences in the insertion losses of the two objectives. The 2% error in the power in Figures 2.10 and 2.12 was experimentally estimated to include the noise fluctuations in the power as well as positional dependencies of the power meter. In Figure 2.13, larger error bars account for the greater power fluctuations that day.

2.9.3 *Materials*

The synthesis and characterization of the two-photon properties of the primary dye used in this study, AF-350 (tris[4-(7-benzothiazol-2-yl-9,9-diethylfluoren-2-yl)phenyl]amine), was described elsewhere^[43] and was donated by the U.S. Air Force Research Laboratory. A stock solution of AF-350 in toluene (Fisher Scientific) was prepared at 0.96 wt.-% and used for several months due to its high stability in the solution phase.[43] The monomer used was trimethylolpropane triacrylate (TMPTA) (Aldrich) from which the inhibitor (100 ppm hydroquinone monomethyl ether) was removed prior to use with inhibitor removal beads (Aldrich). Approximately 0.1 wt.-% solutions of AF-350 in TMPTA were made from the stock solution of dye in toluene; the toluene was removed by rotovapping (Büchi, Switzerland). The solutions were freshly prepared before quantitative studies, for example when measuring TPP response diagrams or polymerizing voxels for width versus power measurements. For general feature fabrication, 0.1 wt.-% solutions up to about one month old were used; while some

deviation in the TPP response was observed, it was not appreciable. The solution of 0.1 mM of 9-fluorenone-2-carboxylic acid (Acros) and 0.1 M of triethanolamine (Acros) in TMPTA was prepared according to a literature recipe.^[15] For fluorescence imaging in colloidal crystals, a 10^{-5} M solution of rhodamine 6G (Acros) was prepared in a 2:1 glycerol (Acros) to water mixture for optimal index matching with the colloids. All water was purified with a Milli-Q UV Plus system (Millipore, Billerica, MA).

2.9.4 Colloidal Crystal Preparation

The colloidal crystals used to construct the TPP response diagram and for SEM imaging were prepared according to a modified ultrasonicated flow cell method introduced by Xia *et al.*^[61,62] The key differences from a modified procedure previously published by our group [63] will be explained here. The substrates were 22 mm x 22 mm No. 1 coverslips (Corning, Inc.). After cleaning, the coverslips were placed in an aqueous 0.1 mM potassium hydroxide solution for 30 minutes, after which they were rinsed with deionized water and dried with N₂. The top slide assembly was hydrophobically treated by immersion in a 2 mM solution of n-octadecyltrichlorosilane (Gelest, Inc., Morrisville, PA) in hexanes (Fisher Scientific) for 3 minutes, rinsed with toluene and dried with N₂. Mylar® LBT-2 films (48 gauge) were generously provided by Dupont Teijin Films (Hopewell, VA) and used for spacers—two for each flow cell. The cell was assembled on top of the bottom slide in the following order: Mylar® spacer (no opening), coverslip, Mylar® spacer (with opening), top slide assembly. The colloids used were 0.49 ± 0.03 μm in diameter (Duke Scientific Corporation, Palo Alto, CA).^[64] The colloidal crystals were annealed at 450 °C in air for 1.5 hours to enhance mechanical stability.

For SEM samples of features written in colloidal crystals, there were some alterations to this procedure. First, plastic coverslips (Fisher Scientific, 12-547) were employed for their resistance to the etch treatment used to dissolve the colloids (5 % HF(aq), 30 minutes). The coverslips were not cleaned, but rather treated with oxygen plasma (Plasma-Therm, Unaxis 790 Series) and then immersed in a solution of 2 mM methacryloxypropyltrichlorosilane (Gelest, Inc.) in hexanes for about 5 minutes, rinsed in toluene, and dried with N₂. Acrylating the surface of the polymer coverslips enabled the TPP features to covalently attach to the substrate, preventing them from washing away in the colloid etching step. The colloidal crystals grown on polymer coverslips were not annealed. Due to the flexibility of the polymer coverslips, they could not be used directly adjacent to the objective. Instead a blank glass coverslip was placed on the oil-immersion objective, followed by a drop of monomer solution and then a colloidal crystal grown on a polymer coverslip inverted above that. The monomer solution readily infiltrates the colloidal crystal.

For the colloidal crystals seen in the confocal images in Figures 2.16 and 2.17, $1.57 \pm 0.06 \mu\text{m}$ silica microspheres (Duke Scientific Corporation, Palo Alto, CA) were used since larger colloids are better resolved via confocal microscopy. These colloids were crystallized by sedimentation of the as received solution (2 wt.-% in water) in polydimethylsiloxane (PDMS) cells on 22 mm x 40 mm No. 1 coverglasses (Corning, Inc.). The PDMS cells had an outer dimension of $\sim 3 \text{ cm} \times 3 \text{ cm}$, an inner opening of $\sim 1.3 \times 1.3 \text{ cm}$ and a thickness of $\sim 0.8 \text{ cm}$. To make the PDMS cells, a silicon wafer was placed, polished side up, in a Petri dish and an aluminum bar ($\sim 1.3 \times 1.3 \times 2.5 \text{ cm}$) was centered on top of that. The PDMS precursor used was Sylgard® 184 (Dow Corning Corporation, Midland, MI) which was mixed, degassed, and poured around the assembly in the Petri dish. The PDMS was cured at $\sim 65^\circ\text{C}$ for 4 hours after

which it was allowed to cool and the PDMS cell was cut away from the various components using a utility knife. The PDMS cells were cleaned by sonication in ethanol prior to use and the coverglasses were cleaned in glassware cleaning mixture described previously. The PDMS cells were placed on the clean coverglasses and allowed to seal, after which the assembly was filled with ~1 ml of the colloidal suspension and placed under a crystallization dish for sedimentation and drying.

The colloidal crystal used for spectroscopy was made from colloids with a diameter of approximately 343 nm, synthesized via a modified Stöber recipe.[65] The colloidal crystal was prepared using a modified vertical deposition technique[66] where the silicon substrate (1.25 x 3.75 cm) and deposition vial were both at 45° with respect to gravity. A thin layer of silicon was grown by low pressure chemical vapor deposition and then oxidized, yielding an approximately 10.5 nm layer of silica. This silica layer prevents the colloidal crystal from cracking due to the contraction upon TPP of large features. The colloidal crystals on silicon substrates were inverted for TPP in the same fashion as those samples for SEM.

2.9.5 Microscopy and Spectroscopy of TPP Features

After TPP, the excess monomer solution was removed by thoroughly rinsing in ethanol and drying with N₂. The features written inside colloidal crystals on glass coverslips were then backfilled with the rhodamine solution for single-photon fluorescence confocal imaging. The sample for SEM with features written in a colloidal crystal on a polymer coverslip was etched in a 5% HF(aq) solution for 30 minutes to dissolve the colloids. Gold was evaporated on samples prior to SEM imaging (Hitachi S-4700). Micro-spot spectroscopy[67] of the colloidal crystal and embedded TPP features was taken using a 10x, 0.25 NA objective on an inverted optical

microscope (Axiovert 135, Carl Zeiss, Inc.) with output coupled to a UV-Vis spectrometer (PDA-512, Control Development, Inc., South Bend, IN). Spectra were normalized to a protected silver mirror specified to have $\geq 95\%$ reflectivity over the wavelength range used (Melles Griot, Rochester, NY). The collection spot size is on the order of 10-15 μm . Simulated spectra were calculated using the layered-KKR method.[52,53]

2.10 References

1. W. M. Lee, S. A. Pruzinsky, P. V. Braun, *Adv. Mater.* **2002**, *14*, 271.
2. S. A. Pruzinsky, P. V. Braun, *Adv. Funct. Mater.* **2005**, *15*, 1995.
3. M. Göppert-Mayer, *Ann. Physik* **1931**, *9*, 273.
4. R. J. Collins, D. F. Nelson, A. L. Schawlow, W. Bond, C. G. B. Garrett, W. Kaiser, *Phys. Rev. Lett.* **1960**, *5*, 303.
5. A. Javan, W. R. Bennett, D. R. Herriott, *Phys. Rev. Lett.* **1961**, *6*, 106.
6. T. H. Maiman, *Br. Commun. Electron.* **1960**, *7*, 674.
7. W. Kaiser, C. G. B. Garrett, *Phys. Rev. Lett.* **1961**, *7*, 229.
8. *Selected Papers on Ultrafast Laser Technology*, Vol. MS 44 (Eds: T. R. Gosnell, A. J. Taylor), SPIE Optical Engineering Press, Bellingham, WA, **1991**.
9. W. Denk, J. H. Strickler, W. W. Webb, *Science* **1990**, *248*, 73.
10. J. H. Strickler, W. W. Webb, *Proc. SPIE* **1990**, *1398*, 107.
11. J. N. Gannaway, C. J. R. Sheppard, *Opt. Quant. Electron.* **1978**, *10*, 435.
12. <http://www.loci.wisc.edu/multiphoton/mp.html>, May 1, 2006.
13. T. Tanaka, H. B. Sun, S. Kawata, *Appl. Phys. Lett.* **2002**, *80*, 312.
14. K. Takada, H. B. Sun, S. Kawata, *Appl. Phys. Lett.* **2005**, *86*, 71122.
15. J. D. Pitts, P. J. Campagnola, G. A. Epling, S. L. Goodman, *Macromolecules* **2000**, *33*, 1514.
16. W. H. Zhou, S. M. Kuebler, K. L. Braun, T. Y. Yu, J. K. Cammack, C. K. Ober, J. W. Perry, S. R. Marder, *Science* **2002**, *296*, 1106.

17. T. Y. Yu, C. K. Ober, S. M. Kuebler, W. H. Zhou, S. R. Marder, J. W. Perry, *Adv. Mater.* **2003**, *15*, 517.
18. T. Watanabe, M. Akiyama, K. Totani, S. M. Kuebler, F. Stellacci, W. Wenseleers, K. Braun, S. R. Marder, J. W. Perry, *Adv. Funct. Mater.* **2002**, *12*, 611.
19. B. H. Cumpston, S. P. Ananthavel, S. Barlow, D. L. Dyer, J. E. Ehrlich, L. L. Erskine, A. A. Heikal, S. M. Kuebler, I. Y. S. Lee, D. McCord-Maughon, J. Q. Qin, H. Rockel, M. Rumi, X. L. Wu, S. R. Marder, J. W. Perry, *Nature* **1999**, *398*, 51.
20. Z. Bayindir, Y. Sun, M. J. Naughton, C. N. LaFratta, T. Baldacchini, J. T. Fourkas, J. Stewart, B. E. A. Saleh, M. C. Teich, *Appl. Phys. Lett.* **2005**, *86*, 4105.
21. H. B. Sun, T. Kawakami, Y. Xu, J.-Y. Ye, S. Matuso, H. Misawa, M. Miwa, R. Kaneko, *Opt. Lett.* **2000**, *25*, 1110.
22. H. B. Sun, K. Takada, S. Kawata, *Appl. Phys. Lett.* **2001**, *79*, 3173.
23. J. M. Kim, H. Muramatsu, *Nano Lett.* **2005**, *5*, 309.
24. R. A. Borisov, G. N. Dorojkina, N. I. Koroteev, V. M. Kozenkov, S. A. Magnitskii, D. V. Malakhov, A. V. Tarasishin, A. M. Zheltikov, *Laser Phys.* **1998**, *8*, 1105.
25. R. A. Borisov, G. N. Dorojkina, N. I. Koroteev, V. M. Kozenkov, S. A. Magnitskii, D. V. Malakhov, A. V. Tarasishin, A. M. Zheltikov, *Appl. Phys. B* **1998**, *67*, 765.
26. H. B. Sun, S. Matsuo, H. Misawa, *Appl. Phys. Lett.* **1999**, *74*, 786.
27. M. Straub, M. Gu, *Opt. Lett.* **2002**, *27*, 1824.
28. J. Serbin, A. Egbert, A. Ostendorf, B. N. Chichkov, R. Houbertz, G. Domann, J. Schulz, C. Cronauer, L. Frohlich, M. Popall, *Opt. Lett.* **2003**, *28*, 301.
29. K. Kaneko, H. B. Sun, X. M. Duan, S. Kawata, *Appl. Phys. Lett.* **2003**, *83*, 2091.
30. M. Deubel, G. Von Freymann, M. Wegener, S. Pereira, K. Busch, C. M. Soukoulis, *Nat. Mater.* **2004**, *3*, 444.
31. M. Deubel, M. Wegener, A. Kaso, S. John, *Appl. Phys. Lett.* **2004**, *85*, 1895.
32. J. Serbin, A. Ovsianikov, B. Chichkov, *Opt. Express* **2004**, *12*, 5221.
33. L. H. Nguyen, M. Straub, M. Gu, *Adv. Funct. Mater.* **2005**, *15*, 209.
34. Y. H. Jun, C. A. Leatherdale, D. J. Norris, *Adv. Mater.* **2005**, *17*, 1908.
35. H. B. Sun, A. Nakamura, K. Kaneko, S. Shoji, S. Kawata, *Opt. Lett.* **2005**, *30*, 881.

36. J. Scrimgeour, D. N. Sharp, C. F. Blanford, O. M. Roche, R. G. Denning, A. J. Turberfield, *Adv. Mater.* **2006**, *In Press*.
37. S. Kawata, H. B. Sun, T. Tanaka, K. Takada, *Nature* **2001**, *412*, 697.
38. G. Witzgall, R. Vrijen, E. Yablonovitch, V. Doan, B. J. Schwartz, *Opt. Lett.* **1998**, *23*, 1745.
39. C. Martineau, R. Anemian, C. Andraud, I. Wang, M. Bouriau, P. L. Baldeck, *Chem. Phys. Lett.* **2002**, *362*, 291.
40. Y. Boiko, J. M. Costa, M. Wang, S. Esener, *Opt. Express* **2001**, *8*, 571.
41. W. H. Teh, U. Durig, U. Drechsler, C. G. Smith, H. J. Guntherodt, *J. Appl. Phys.* **2005**, *97*, 54907.
42. C. Martineau, G. Lemerrier, C. Andraud, I. Wang, M. Bouriau, P. L. Baldeck, *Synthetic. Met.* **2003**, *138*, 353.
43. G. S. He, J. Swiatkiewicz, Y. Jiang, P. N. Prasad, B. A. Reinhardt, L. S. Tan, R. Kannan, *J. Phys. Chem. A* **2000**, *104*, 4805.
44. C. Xu, W. W. Webb, *J. Opt. Soc. Am. B* **1996**, *13*, 481.
45. E. S. Wu, J. H. Strickler, W. R. Harrell, W. W. Webb, *Proc. SPIE* **1992**, *1674*, 776.
46. P. J. Campagnola, D. M. Delguidice, G. A. Epling, K. D. Hoffacker, A. R. Howell, J. D. Pitts, S. L. Goodman, *Macromolecules* **2000**, *33*, 1511.
47. S. M. Kuebler, M. Rumi, T. Watanabe, K. Braun, B. H. Cumpston, A. A. Heikal, L. L. Erskine, S. Thayumanavam, S. Barlow, S. R. Marder, J. W. Perry, *J. Photopolym. Sci. Tec.* **2001**, *14*, 657.
48. K. Garsha, *Proc. SPIE* **2004**, *5323*, 279.
49. H. B. Sun, K. Takada, M. S. Kim, K. S. Lee, S. Kawata, *Appl. Phys. Lett.* **2003**, *83*, 1104.
50. G. Odian, *Principles of Polymerization, Third Edition*; John Wiley & Sons, Inc.: New York, NY, **1991**.
51. E. Nelson, P. V. Braun, unpublished work.
52. C. Cuisin, A. Chelnokov, J. M. Lourtioz, D. Decanini, Y. Chen, *J. Vac. Sci. Technol. B* **2000**, *18*, 3505.
53. N. Stefanou, V. Yannopapas, A. Modinos, *Comput. Phys. Commun.* **1998**, *113*, 49.
54. Y. J. Lee, S. A. Pruzinsky, P. V. Braun, *Opt. Lett.* **2005**, *30*, 153.

55. V. N. Astratov, A. M. Adawi, S. Fricker, M. S. Skolnick, D. M. Whittaker, P. N. Pusey, *Phys. Rev. B* **2002**, *66*, 5215.
56. J. F. Galisteo-Lopez, E. Palacios-Lidon, E. Castillo-Martinez, C. Lopez, *Phys. Rev. B* **2003**, *68*, 5109.
57. Y. A. Vlasov, V. N. Astratov, A. V. Baryshev, A. A. Kaplyanskii, O. Z. Karimov, M. F. Limonov, *Phys. Rev. E* **2000**, *61*, 5784.
58. A. Hibbs, G. MacDonald, K. Garsha, in *Handbook of Biological Confocal Microscopy*, (Eds: J. Pawley), Plenum Press, NY (In Press).
59. K. Garsha, *Proc. SPIE* **2003**, *4963*, 134.
60. C. J. Bardeen, V. V. Yakovlev, J. A. Squier, K. R. Wilson, S. D. Carpenter, P. M. Weber, *J. Biomed. Opt.* **1999**, *4*, 362.
61. S. H. Park, D. Qin, Y. Xia, *Adv. Mater.* **1998**, *10*, 1028.
62. Y. Lu, Y. D. Yin, B. Gates, Y. N. Xia, *Langmuir* **2001**, *17*, 6344.
63. Y. J. Lee, S. A. Pruzinsky, P. V. Braun, *Langmuir* **2004**, *20*, 3096.
64. N. A. M. Verhaegh, A. van Blaaderen, *Langmuir* **1994**, *10*, 1427.
65. W. Stober, A. Fink, E. Bohn, *J. Colloid Interfac. Sci.* **1968**, *26*, 62.
66. P. Jiang, J. F. Bertone, K. S. Hwang, V. L. Colvin, *Chem. Mater.* **1999**, *11*, 2132.
67. Y. A. Vlasov, M. Deutsch, D. J. Norris, *Appl. Phys. Lett.* **2000**, *76*, 1627.

CHAPTER 3

HIGH INDEX REPLICATION

3.1 Motivation

An important consideration for any cPBG application is the ability to convert a colloidal photonic crystal to a high refractive index structure which exhibits a cPBG. This is typically accomplished via infiltration with a high index material such as Si at an elevated temperature, followed by removal of the silica, resulting in an inverse opal structure. Here, both the TPP features and colloidal crystal serve as a template for the final structure, a silicon-air inverse opal (which may possess a cPBG) containing embedded air defects (Fig. 3.1).

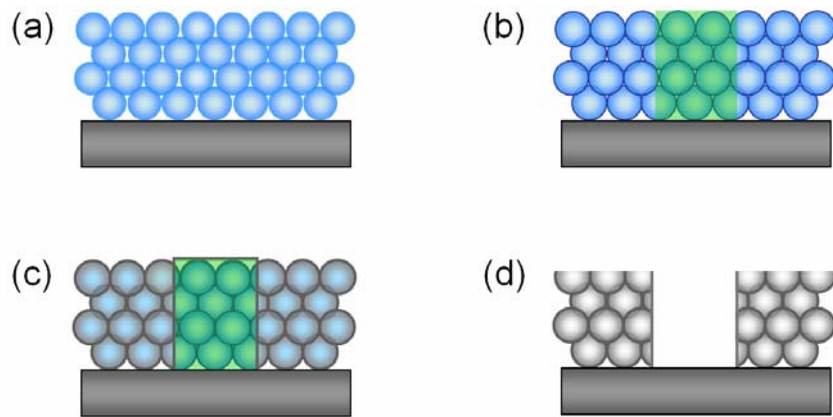


Figure 3.1 Schematic overview of experimental procedure for inverting a silica colloidal crystal with embedded TPP defects in silicon involving: (a) colloidal crystallization, (b) TPP, (c) silicon infiltration, and (d) removal of the silica and polymer template.

For success following this general procedure, it is important that the materials formed through TPP are stable at the requisite high temperatures, for example, at least 250 °C to 350 °C for CVD of Si or Ge. Previously, an inorganic cationic TPP resist was used to deposit a silica hybrid photoresist within a silica colloidal crystal.[1] Here, we demonstrate the inversion in silicon of TPP features written with a robust organic resist.

While Figure 3.1 shows the basic idea of the procedure for inversion, much engineering had to be devoted to get this to work. Additional processing steps were necessary to combat issues that have evaded researchers and have gone unacknowledged in literature.[1] Also, all of the steps in the procedure are interrelated, modifying one step often had a large impact on those to come and many iterations were required to come up with a successful procedure. In this chapter we will discuss in detail the processing steps we used to invert colloidal crystals with embedded TPP defects in silicon (Fig. 3.2). Chapter 4 will cover the microscopy and spectroscopy results obtained from defects embedded in this fashion in silicon inverse opals.

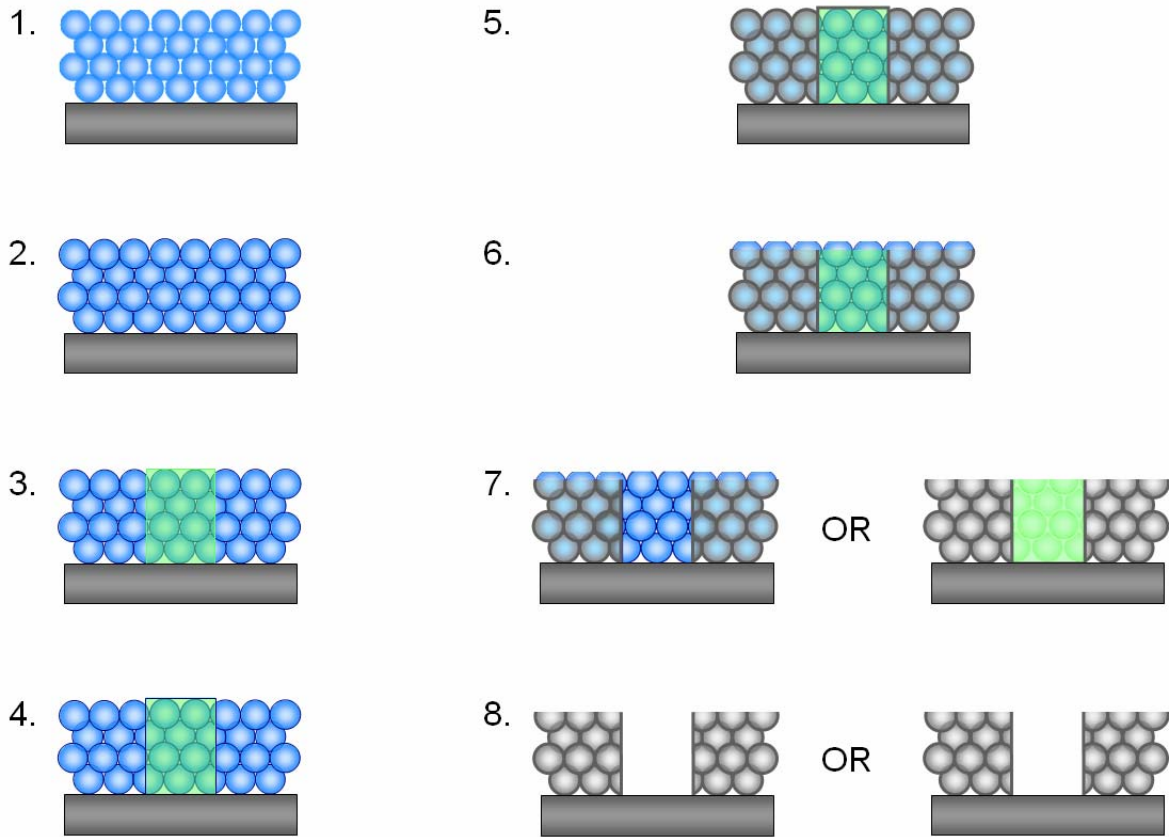


Figure 3.2 Schematic of the expanded procedure: 1. colloidal crystallization, 2. first atomic layer deposition of alumina, 3. TPP, 4. second atomic layer deposition of alumina, 5. chemical vapor deposition of silicon, 6. reactive ion etching of top half-layer of silicon, 7. removal of polymer by burning or wet etch of silica and alumina, 8. wet etch of silica and alumina or removal of polymer by oxygen plasma treatment.

3.2 Calcination of Colloids

Artificial opals were deposited from silica colloids grown via seeded Stöber growth processes,[2,3] using either manual or continuous additions.[4] The microspheres used here had diameters of either 720 nm or 920 nm. Prior to the crystal growth, the silica colloids were calcined at 600 °C for no less than 48 hours. This prevented the cracking of the artificial opals during post-processing at elevated temperatures.[5] During calcination, the sphere diameter decreases by 5% to 10% (Fig. 3.3a).[6] Although other researchers suggested that calcination at 550 °C for 5 hours is sufficient (Fig. 3.3),[5] we have repeatedly observed that even after 24 hours at 600 °C, the spheres continue to shrink (Fig. 3.4).

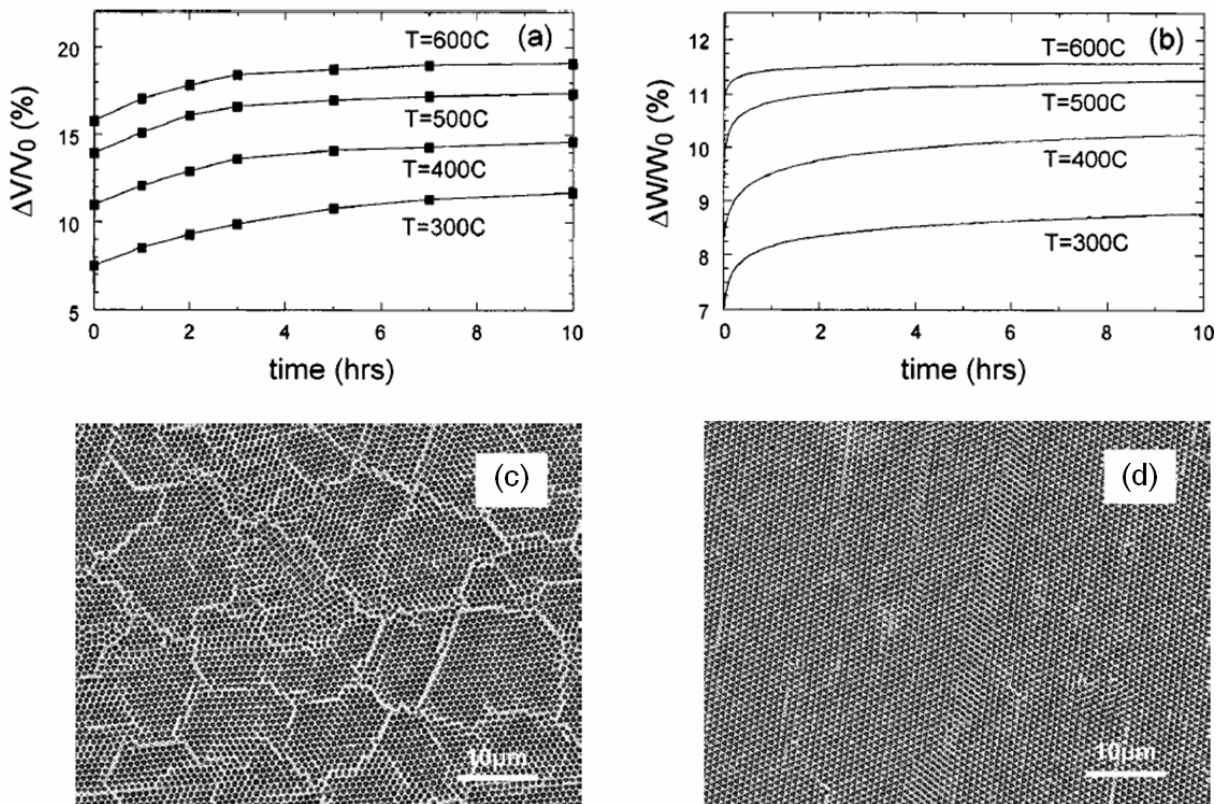


Figure 3.3 (a) Volume and (b) weight change as a function of annealing time and temperature. Inverted silicon-air replicas of colloidal crystals assembled from (c) *non-pre-calcined* and (d) *pre-calcined* (600 °C, 4 h) silica spheres. In pre-calcined opals, Norris *et al.* did not observe cracking during silicon CVD (550 °C, 5 h).[5]

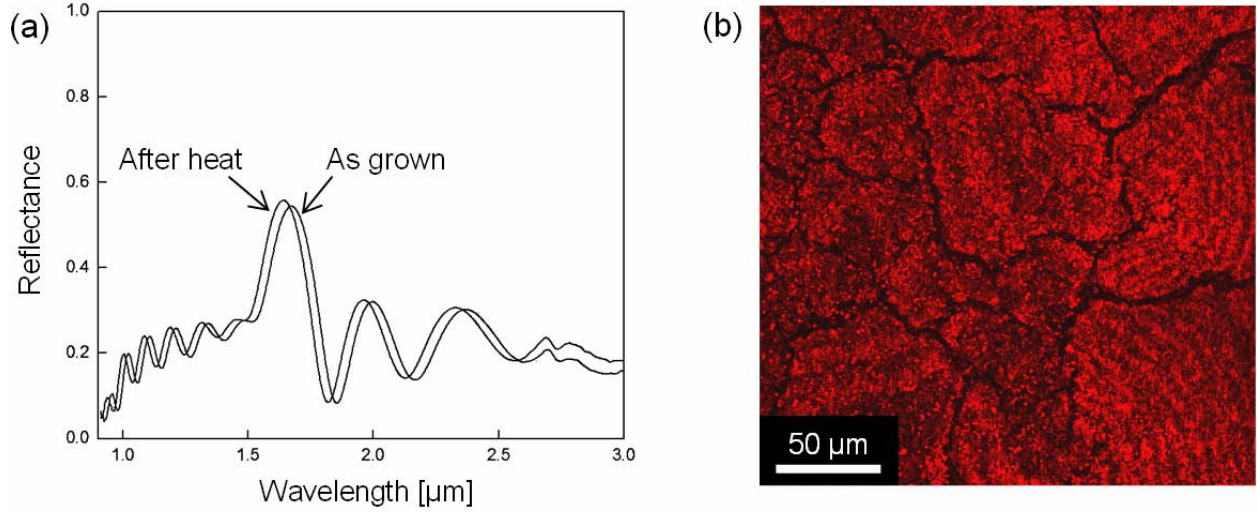


Figure 3.4 (a) Reflectance spectroscopy taken before and after heating (375 °C, ~0.5 h) a colloidal crystal assembled from pre-calcined (600 °C, 12 h) silica particles grown in our lab. The shrinkage upon heating causes the interlayer spacing and therefore Bragg wavelength to decrease. (b) Reflectance confocal micrograph showing cracks that formed upon heating the crystal. Spectroscopy collected from the same spot on a colloidal crystal assembled after calcining the same batch of colloids for another 22 hours at 600 °C overlapped exactly before and after heating, and cracking was not observed.

3.3 Colloidal Crystallization

Despite many research efforts, there still is not a reproducible technique for the growth of high quality artificial opals from silica colloids with sphere diameters over 500 nm. In this work, we employ a modified vertical deposition method[7] which has been adapted to incorporate some variations suggested by Norris *et al.*[8] Here, the introduction of convective flows within the dispersion combats sedimentation of the larger spheres, feeding colloids to the meniscus between the silicon substrate and the alcosol.[8] It has been hypothesized that as the alcosol evaporates, capillary forces and/or hydrodynamic flow drive the ordering of colloids at the meniscus, and over time multilayer colloidal crystals are built up.[9] In comparison with typical,

vertically deposited samples grown from smaller colloids, where the number of layers gradually increases,[7] colloidal crystals grown in this fashion from larger spheres build more rapidly to their maximum number of layers and then gradually get thinner.

Here, 4 ml of a 1.5 vol.-% colloidal suspension in ethanol is dispensed into a 20 ml scintillation vial (Fisher) with a double-side polished silicon substrate (lateral dimensions $\sim 30 \times 12 \text{ mm}^2$, $500 \text{ }\mu\text{m}$ thick). This vial is placed at an angle (about 45°) in a round bottom cork holder on an aluminum block in an incubator (Fisher, Isotemp 125D) (Fig. 3.5). The temperature was set to 42.5°C and 45.5°C for the 730 nm and 930 nm colloids, respectively. The appropriate temperature window was small and occasionally needed to be experimentally adjusted. Increasing the temperature yielded thicker samples, however if the temperature was too high, the sample quality was very poor.

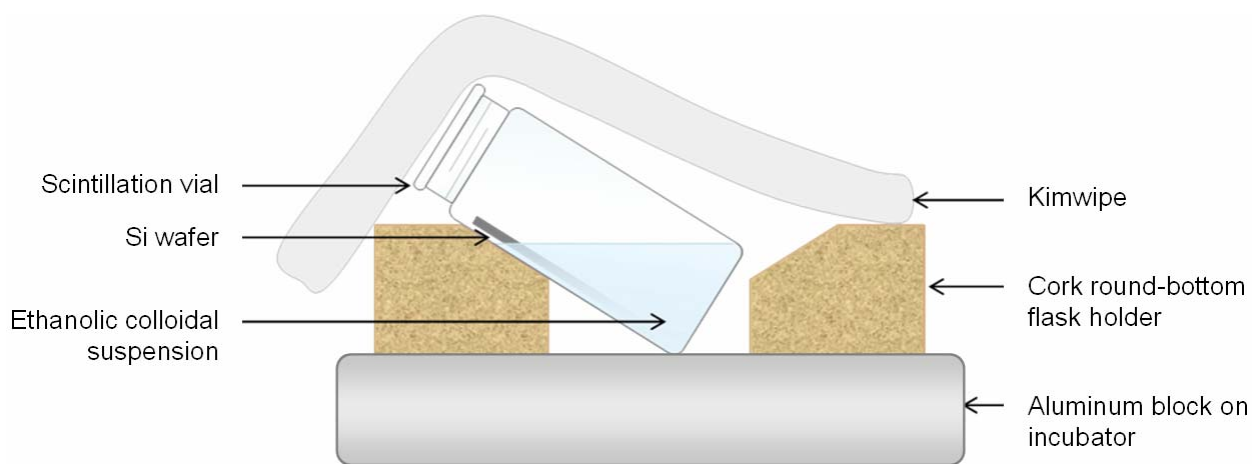


Figure 3.5 Cross-sectional schematic of the modified vertical deposition setup used to obtain colloidal crystals from large silica spheres.

Reflection and transmission spectroscopy were used to interrogate the thickness[7] and quality of the samples (Fig. 3.6, see Section 1.4). Although most of the thin film opals obtained with this method showed excellent optical response, there were a substantial number of samples

that were discarded. Typical high quality samples exhibited reflectivity peaks of ~80-85%, while those with peak reflectivities lower than 70% were not used. Sample thickness also varied significantly between samples. The thickest, high quality samples presented domains of up to 33 layers, however in most cases, samples did not possess domains with greater than 16 layers. We observed variability in the thickness and quality of opals grown from the same batch of microspheres when environmental parameters, like humidity, varied. Isolation of the system is currently being investigated by other researchers in my group.

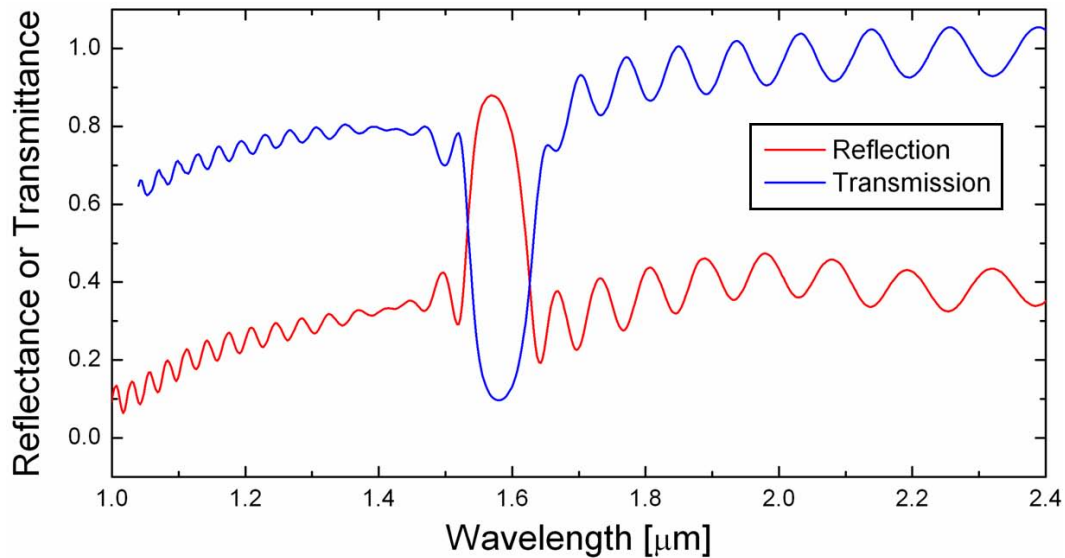


Figure 3.6 Reflection or transmission spectroscopy collected from the same spot a colloidal crystal grown via a modified vertical deposition setup from pre-calcined 720 nm spheres. Data was normalized to a silver mirror or silicon wafer in reflection or transmission mode, respectively.

3.4 Atomic Layer Deposition of Alumina

In order to achieve a silicon-air inverse opal with embedded features and a complete photonic bandgap, it is necessary to start with an array of interpenetrated spheres. The interconnectivity is necessary for removing silica in the final inversion step (see Section 3.9), it

enhances the mechanical stability of the colloidal crystal, which can be important during TPP, and further, calculations show that slightly interpenetrated air spheres may exhibit a larger complete bandgap width in the final silicon-air inverse opal (Fig. 3.7).[10]

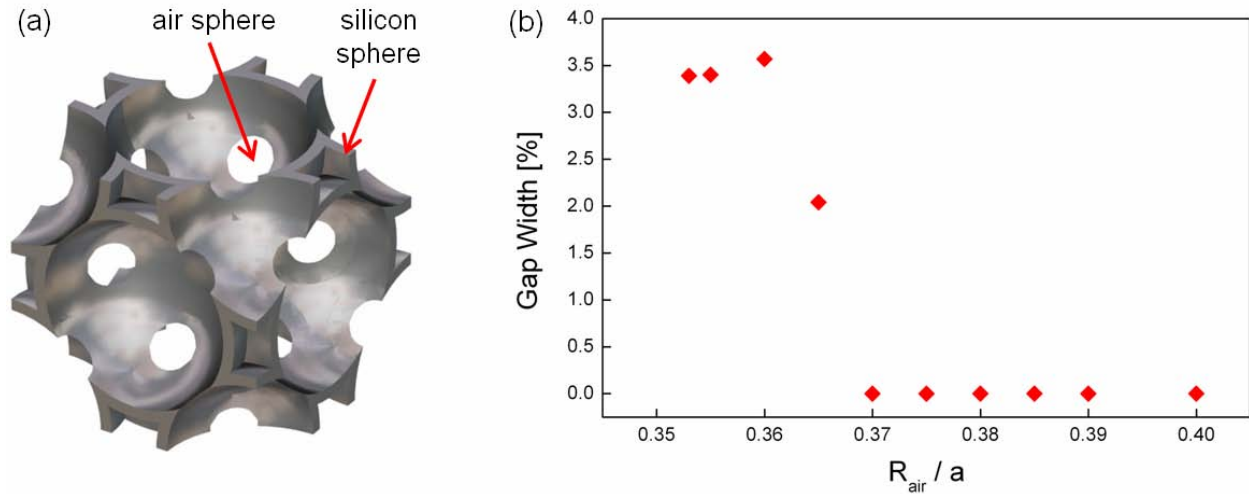


Figure 3.7 (a) Schematic of silicon-air inverse opal and (b) graph of calculated gapwidth[11,12] v. normalized air radius for max theoretical infilling ($R_{Si}/a=0.408$, where trigonal sites close off) with amorphous silicon ($n=3.5$) grown via static CVD. Data courtesy of Dr. Florencio García-Santamaría.

However, the spheres comprising an artificial opal are not perfectly close-packed,[13] let alone interpenetrated. To obtain an interpenetrated array of spheres, sintering might appear to be the simplest approach, however the high temperatures involved (greater than 800 °C) can cause unwanted side effects like cracking and oxidation of the silicon substrate.[14] An advantageous alternative is to grow a thin, conformal oxide layer around the spheres. This film must satisfy several requirements. An appropriate, controllable, conformal growth method needs to exist for the desired material, which must be mechanically and thermally stable, and removable in the final structure. Further, it is required that this material does not absorb at 780 nm and that index matches with the colloids and/or monomer so as not to cause heating or scattering during TPP.

Several materials were tried including one apparently ideal candidate, silica, which was grown either via silica CVD,[15] or silicon CVD followed by oxidation. However, these attempts were unsuccessful, respectively, because the silica grown was not dense and cracked upon heating or because substrate oxidation caused the sample to detach during the final etch step. In the end, the material that satisfied all of the aforementioned conditions was alumina (Al_2O_3) grown by atomic layer deposition (ALD).

A commercial ALD system (Cambridge NanoTech Inc.) was utilized to controllably grow highly conformal, thin Al_2O_3 films within the artificial opals. The precursor chemicals (with nitrogen as the carrier gas) were injected (at a flow rate of 20 sccm) in an alternating fashion through the sample chamber to react and form atomic monolayers. The opening time of the valves for water and trimethylaluminum ($\text{C}_3\text{H}_9\text{Al}$) were set to 0.05 s and 0.10 s, respectively. The sample chamber was maintained at 200 °C and approximately 2 Torr. The process was automatically repeated for 80 to 130 cycles, depending on the requisite oxide layer thickness. In this fashion, the degree of sphere interpenetration was accurately controlled. Again, spectroscopy was used to confirm the success of this step (Fig. 3.8). The peak position correlated well with bandstructure calculations performed assuming that one monolayer of Al_2O_3 (~0.1 nm, $n=1.60$) grew per cycle. As the alumina layer thickness increases, the peak redshifts because the overall effective refractive index of the colloidal crystal increases (see Section 1.4), while the peak intensity decreases since the structure is getting closer to a homogenous material for which, of course, there is no peak.

Occasionally, the desired alumina film thicknesses were obtained in two ALD growths, one before and one after TPP. As mentioned, growing the film before TPP helps prevent cracking during the TPP of large-area features. Though not rigorously confirmed, the second

ALD may improve the edge resolution of air features in the final silicon-air inverse opals. Since the polymer shrinks upon polymerization, the second ALD step may fill in gaps between the polymer and silica spheres at the periphery of the TPP features. Filling these gaps with alumina (which is removed in the final structure) before silicon CVD would prevent them from being filled with silicon during the CVD step to follow. This could be important because if they were filled with silicon, the edges of the features might terminate as silicon spheres rather than fractions thereof, potentially limiting both edge resolution and minimum feature size.

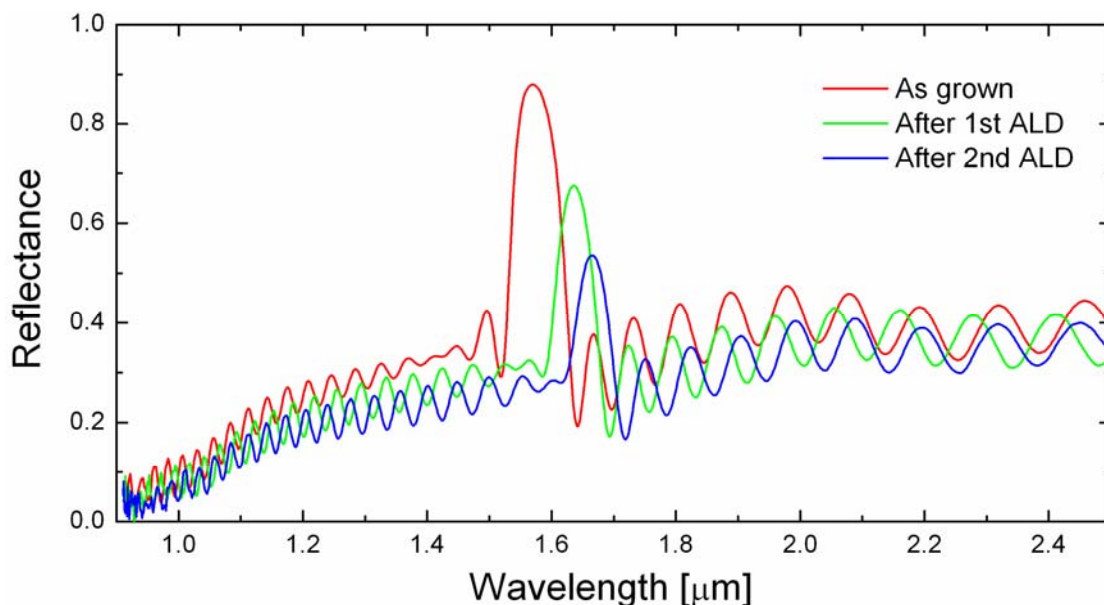


Figure 3.8 Reflection spectroscopy of a colloidal crystal as grown, and after 80 and 130 cycles of ALD on a sample assembled from 720 nm spheres.

3.5 Two-Photon Polymerization

Details regarding the TPP step were covered in depth in Chapter 2. Again, the addition of a fluorescent dye in the monomer solution enabled in situ fluorescence confocal imaging (Fig. 3.9) and facilitated registration of the TPP features with the underlying lattice. This will be critical in the definition of functional defects.

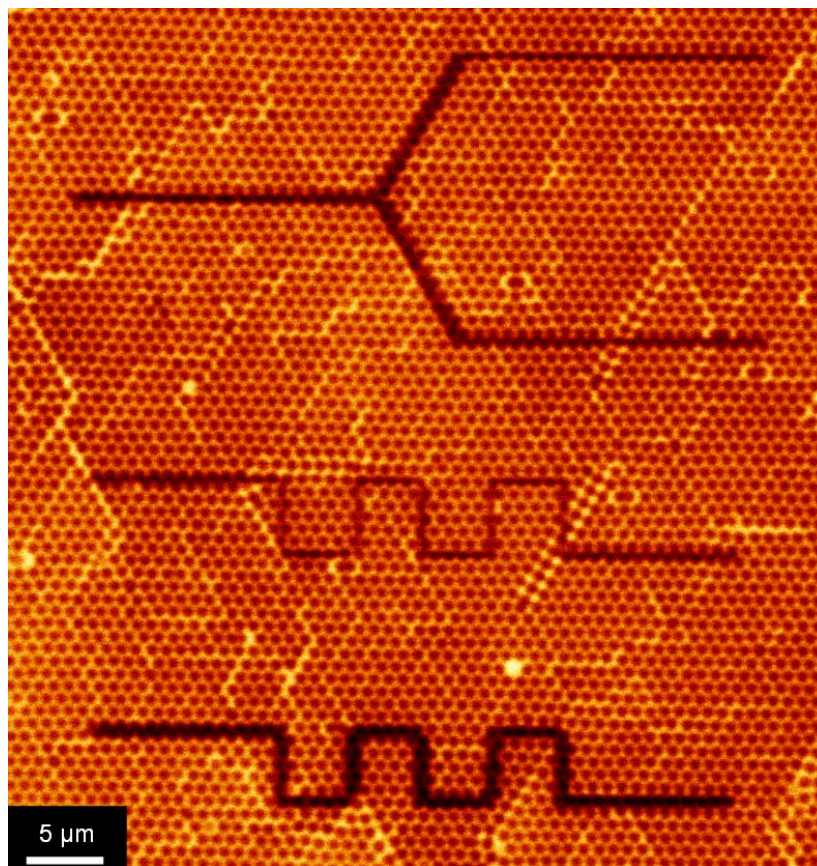


Figure 3.9 In situ fluorescence confocal micrograph taken directly after TPP in the same resin used for polymerization. TPP feature shows up dark because the two-photon exposure also bleaches the fluorescent dye. Polymerization of that region was confirmed via optical microscopy after rinsing away unreacted monomer.

It is also essential that the resultant features are able to withstand the elevated temperatures required for silicon CVD. It was previously commented that this was not possible with an organic resist.[1] However, we are able to grow silicon at 325 °C (see Section 3.6), and thermogravimetric analysis (TGA) reveals that our polymer, poly(TMPTA), does not experience significant weight loss at this temperature (Fig. 3.10a). It is further important that the polymer retain optical transparency if it will be present in the final structure (Fig. 3.10b,c).

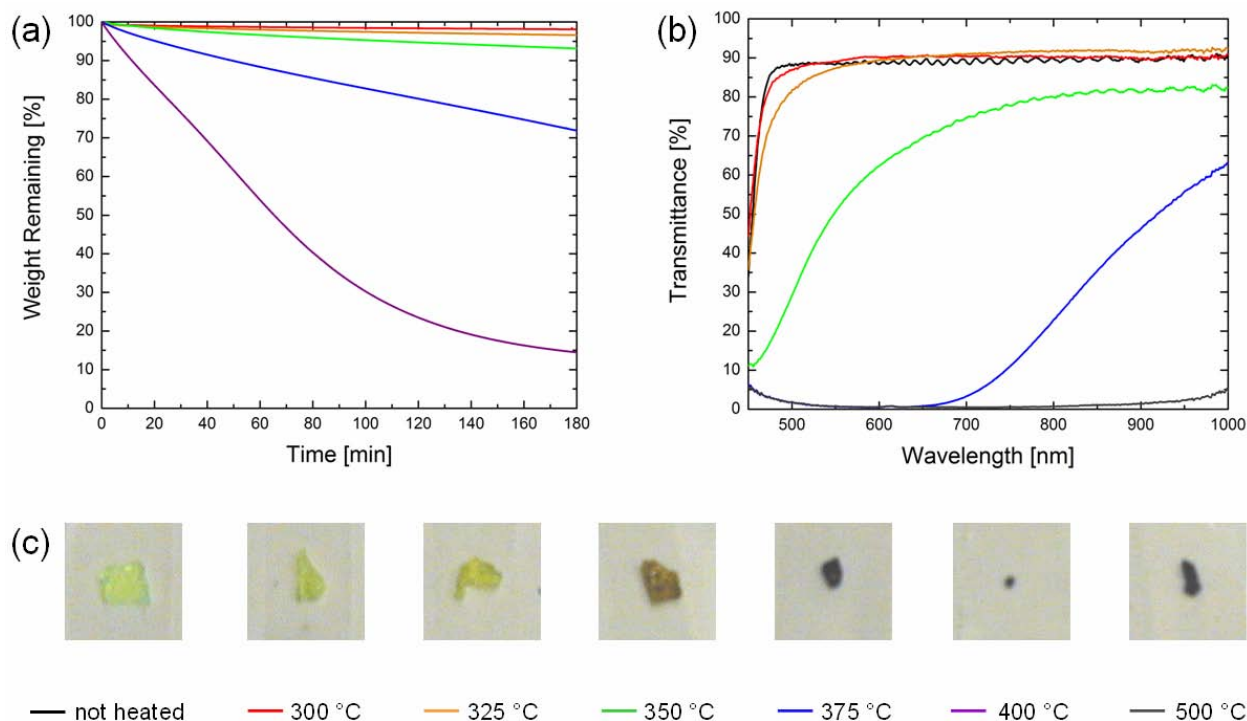


Figure 3.10 (a) TGA results, (b) transmission spectra, and (c) pictures of poly(TMPTA) samples held at an elevated temperature for 3 h in N₂. Undulations in spectra for the samples that were unheated or heated to 350 °C are artifacts due to insufficient lamp warmup.

3.6 Chemical Vapor Deposition of Silicon

Silicon CVD allows the growth of high quality, low roughness, conformal silicon films around the spheres and TPP features within the colloidal crystal.[16,17] Previous recipes for silicon CVD in opals involved operating above the decomposition temperature of our polymer (Fig. 3.10). In order to get reasonable growth rates at 325 °C, the working conditions had to be carefully chosen and optimized. Disilane (Si₂H₆, 98%, Gelest) was selected as the precursor gas as its decomposition temperature is lower than that for silane (SiH₄). A static CVD system, where the reacting gas was confined in a cell together with the sample, was utilized since low pressure CVD systems show negligible growth rates at this temperature.[8] Finally, the pressure of disilane in the sample cell at room temperature was set to approximately 50 mbar. It was

observed that higher pressures did not significantly increase the growth rate, while samples prepared at higher pressures had a tendency to peel off the substrate. The decomposition time controlled the thickness of the silicon film. For samples assembled from the 730 nm spheres, two cycles of 15 hours were performed, while opals made from the 900 nm spheres required an additional cycle (Fig. 3.11). Because this is a static CVD setup, it is necessary to grow the silicon in several cycles rather than one longer run, because the reaction products are not removed from the chamber and eventually the reaction reaches equilibrium.

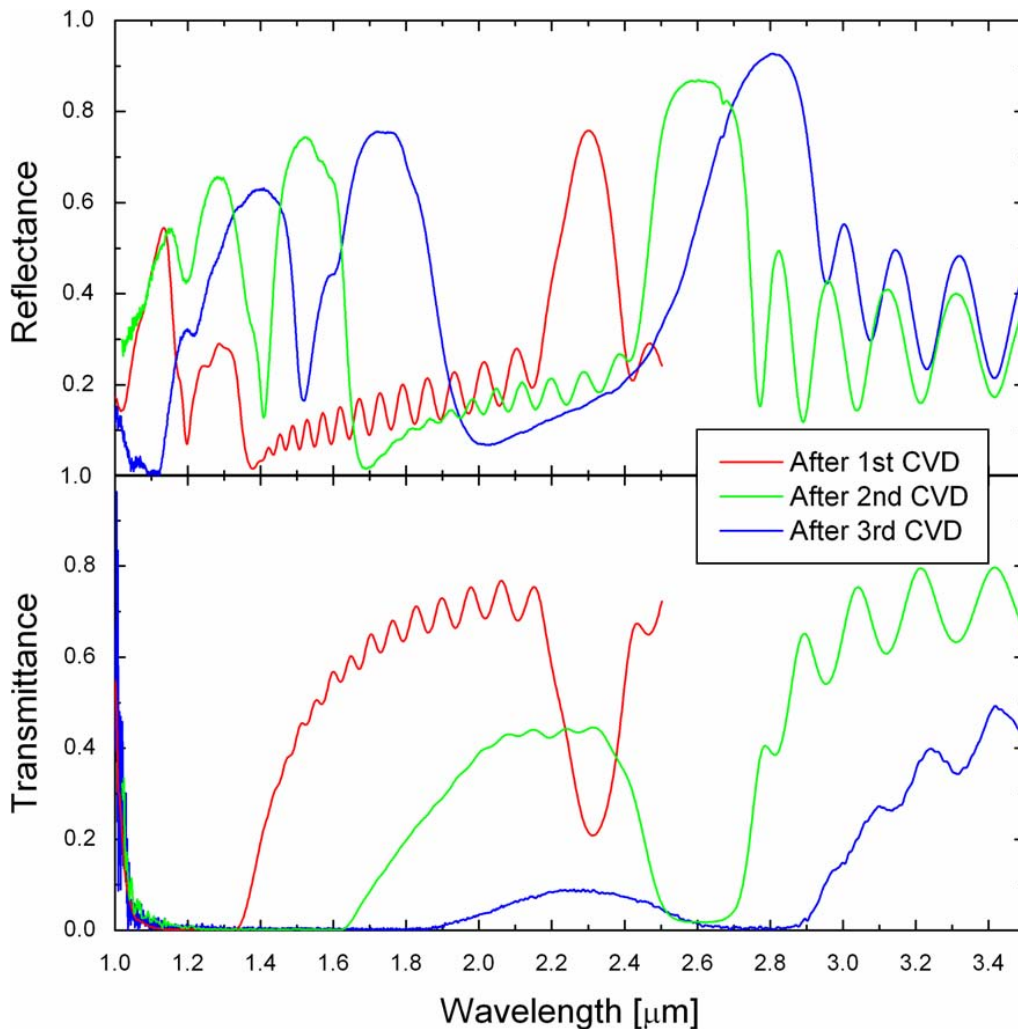


Figure 3.11 Spectroscopy taken from a silicon-silica composite during and after silicon CVD. Data was normalized to a silver mirror or silicon wafer in reflection or transmission mode, respectively. Opal was assembled from 920 nm spheres.

Spectroscopy was again used to monitor the progress of this processing step (Fig. 3.11). Peak positions were correlated with bandstructure calculations to determine the extent of silicon infilling. Structures were filled until the trigonal interstitial sites in the {111} planes closed off ($R_{Si}/a=0.408$). As the silicon filling fraction increased, the effective refractive index and photonic strength of the structure increased, causing the diffraction wavelength and peak reflectance to increase. The background transmittance decreased due to the increased scatter at higher silicon filling fractions.

3.7 Reactive Ion Etching

After silicon CVD, it is necessary to expose the silica colloids in order to remove them via wet etching (see Section 3.9). Here, we used reactive ion etching (RIE) to expose the top layer of silica spheres.[8] The RIE recipe used is selective for silicon versus silica, (Fig. 3.12), so the colloids slow down the etching once they are exposed. Care must be exercised to avoid over-etching, since the first layer of silica colloids is not a perfect etch stop.

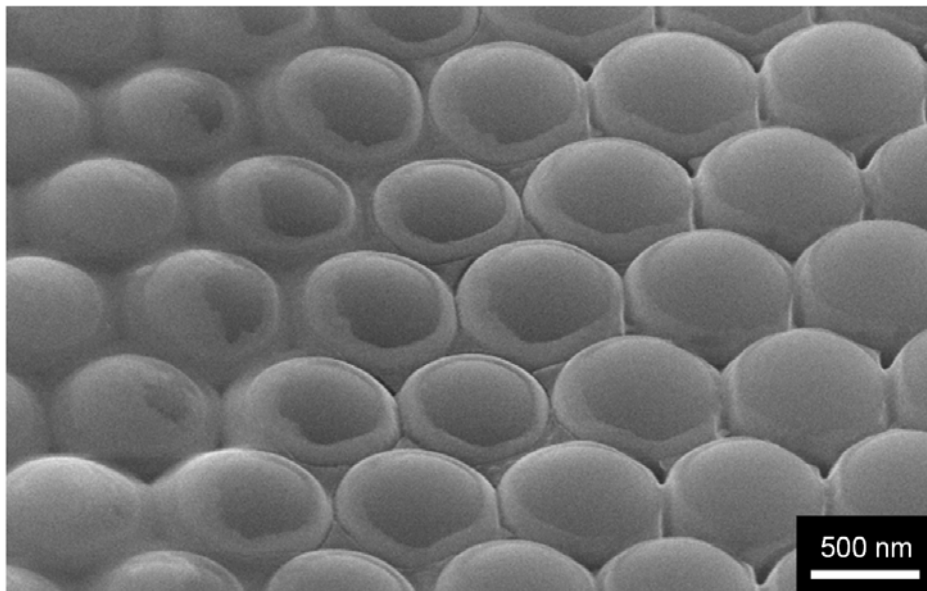


Figure 3.12 SEM micrograph of the top of a silicon-silica composite after RIE, taken at the edge of a region that had been masked off and not exposed to the RIE.

When properly etched, a high-quality surface is achieved in the final, silicon inverse opal (Fig. 3.13). RIE also removes the silicon overlayer from the top of TPP features that extend to the top surface of the photonic crystal, which may facilitate coupling to waveguides and other features. It is important for these TPP features not to protrude much past the surface, because the silicon that grows on the sides of the protruding portions is not removed during RIE, leaving silicon side-walls in the final structure (Fig. 3.14).

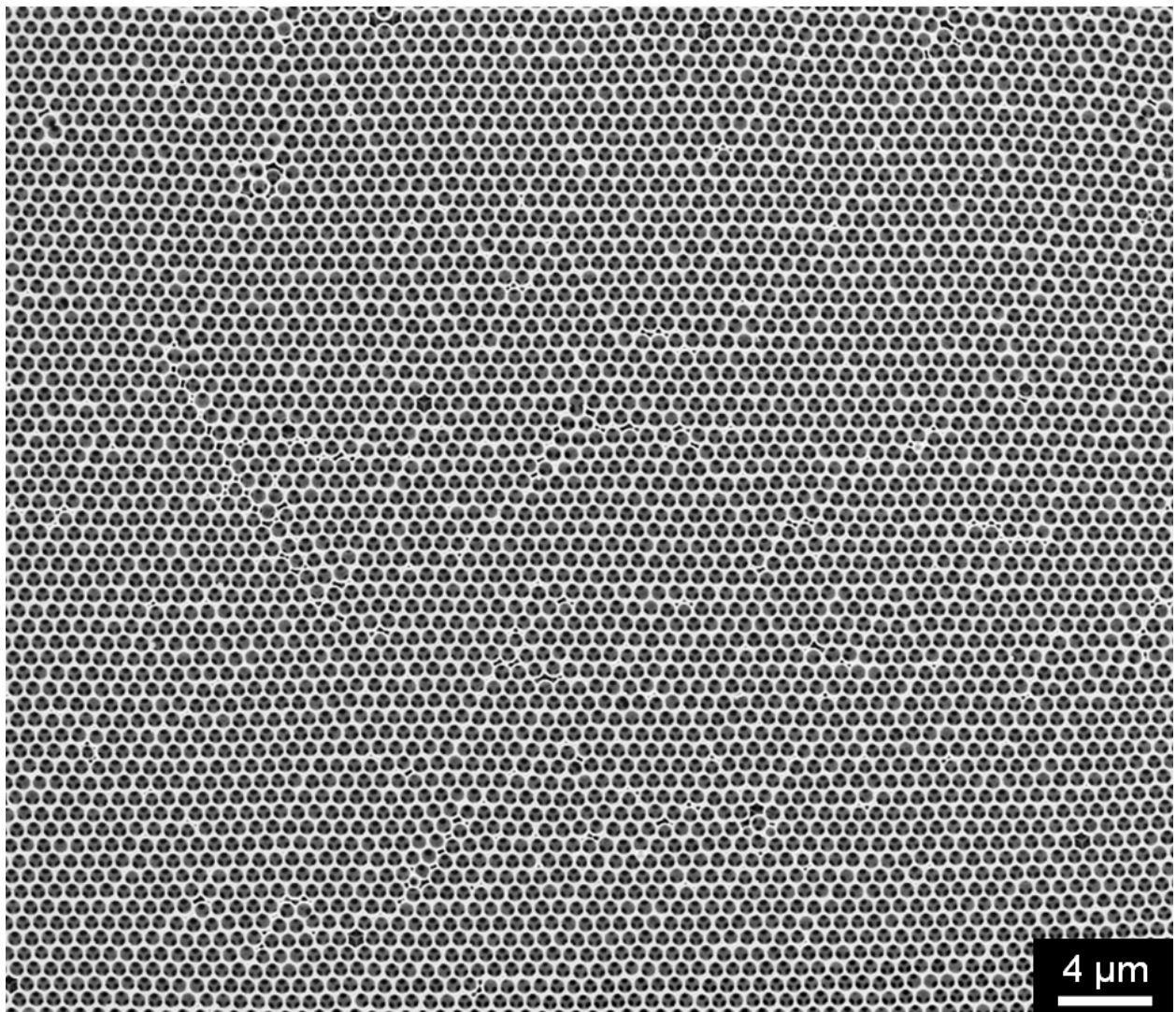


Figure 3.13 SEM micrograph of a high-quality, smooth surface of a silicon inverse opal obtained by reactive ion etching, followed by wet etching to remove the silica. It is possible to see the interconnecting windows to the layer below.

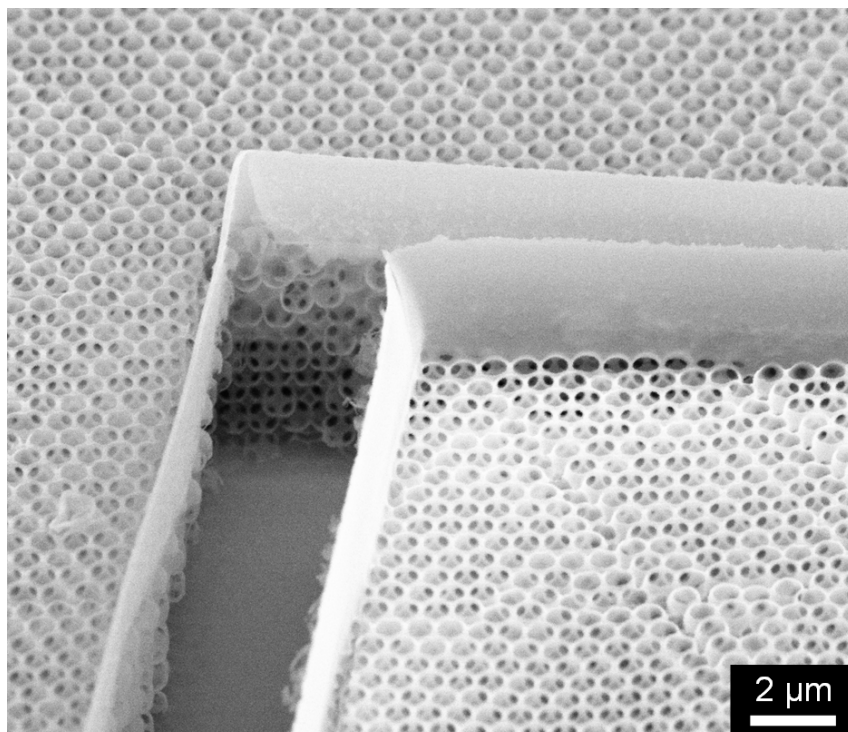


Figure 3.14 SEM micrograph of a silicon inverse opal obtained by inverting a colloidal crystal with a bent TPP feature. The TPP feature had protruded from the top of the sample and the directional RIE procedure only removed the silicon from the top and not sides of the feature. A second ALD cycle was not grown on this sample which may explain the edge roughness of the feature within the photonic crystal.

RIE was performed using a Uniaxis 790 series reactive ion etching system. A power of 70 W, chamber pressure of 100 mTorr, and O_2 and SF_6 gas flow rates of 20 sccm were used. A typical run lasted 1 minute and the DC voltage readout was around 35 to 40 V. Typically, the sample was masked off to only expose a small region to the RIE (Fig. 3.12). This can be accomplished simply by taping off a region of the sample before RIE and then removing the tape after RIE by immersing the taped sample in an appropriate solvent. Alternatively, a thin piece of plastic with a small opening can be placed over the sample during RIE (here, $\sim 50 \mu m$ thick Kapton® was used). The dimensions of the RIE-exposed region were typically on the order of $1 \times 2 \text{ mm}^2$. More details regarding the RIE step, including the importance of using RIE, the

resulting spectroscopy, and the rationale for only exposing a small region to the RIE will be discussed when covering the wet etch of silica (see Section 3.9).

3.8 Removal of Polymer (Optional)

One option is to leave the polymer in the final structure, since it retains optical transparency, even after exposure to 325 °C (Fig. 3.10). This yields for the final structure, a silicon-air inverse opal with the defect region consisting of a polymer-air inverse opal (Fig. 3.2). While the polymer-air inverse structure has a diffraction peak, it does not overlap with that of the silicon-air inverse opal, which may be appropriate for PBG-based applications. However, due to the very limited literature on the design of defects in colloidal photonic crystals,[18] it is not clear whether it would be advantageous to leave the polymer in or remove it, when targeting PBG-based applications.

Here, we chose to leave the polymer in for the samples from which spectroscopy was collected (see Chapter 4), as some issues were encountered when trying to remove the polymer, by burning or plasma etching. While burning was successful in removing large-area features that extend through the crystal, it was not as appropriate for embedded, isolated TPP features. It was found that the polymer had to be burned out before removing the silica and alumina because the final silicon-air inverse opal was not mechanically stable enough to resist cracking upon heating. However, before removing the silica or alumina, the structure is almost completely filled, giving little or no room for the gases evolved upon burning to escape, especially for embedded, isolated features. Therefore, burning was most appropriate for the removal of large-area features that extend through the thickness of the colloidal crystal. For isolated, thin, or complicated features, burning was occasionally appropriate, though debris was sometimes found along the edges of

these features (Fig. 3.15). It is possible this debris was charred polymer that was not successfully removed, or it could be material that had redeposited during overly aggressive ion milling. Burning was done after RIE so that the silicon layer on top of the TPP features was removed, giving a cleaner final product. Samples were burned overnight at 500 °C in air, as TGA showed these conditions were sufficient to burn poly(TMPTA) cleanly. The polymer was removed by burning for those samples inspected that were to be inspected via SEM, as this greatly enhanced the contrast between the defect regions and the surrounding inverse opal.

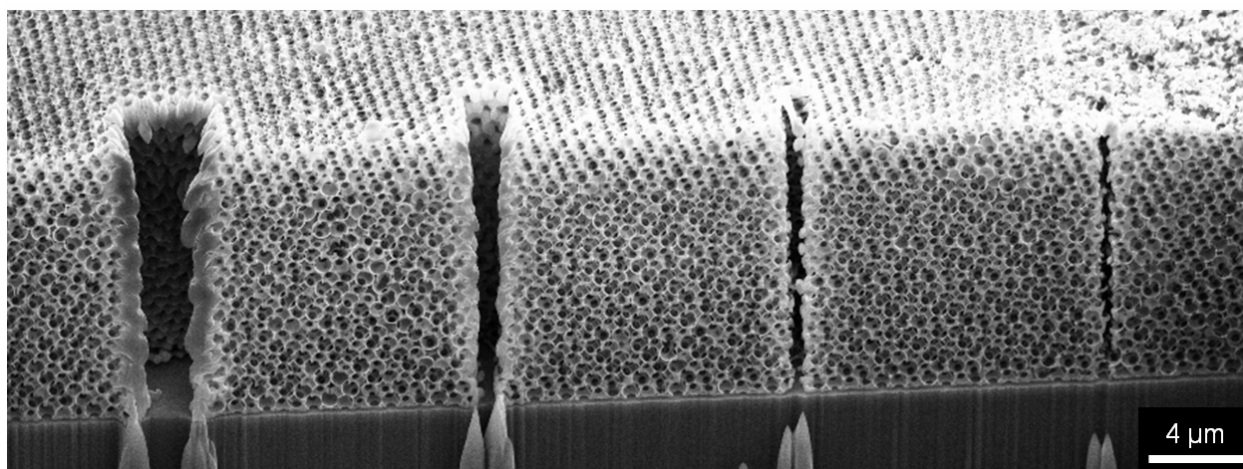


Figure 3.15 FIB cross-sections through a series of defects in a silicon-air inverse opal. Debris can clearly be seen on the walls of the air defects. It is unclear if this is due to insufficient burnout or redeposition during FIB milling or both. Some of the other, similar defects on the same sample were removed cleanly (see Chapter 4).

It may be more desirable to use an oxygen plasma treatment,[19] especially to remove isolated TPP features. This may be done after removing the silica and alumina, enabling the oxygen plasma to access embedded, isolated features. Preliminary attempts were promising, though longer times or higher powers may be necessary for a complete removal of the polymer. It will also be important to verify that the optical properties of the inverse opal are not affected

by the final plasma recipe. Preliminary work was done using a barrel asher (APE 110, LPE Plasma Systems) that was run overnight at a power of 30 W.

3.9 Wet Etch of Silica and Alumina

The silica and alumina can be removed via wet etching using a freshly prepared solution of 5% hydrofluoric acid (HF) in 50% ethanol, 45% water. The ethanol is important if the TPP features have not been removed, as it enables etching within the hydrophobic polymer regions. As previously mentioned, to etch a sample, it is important to have an exposed, interpenetrated network of oxide. We used alumina ALD to improve the interconnectivity (see Section 3.4) and RIE to remove some silicon from the top of the sample and expose the first layer of silica spheres (see Section 3.7). It was determined that both of these steps were necessary in order to successfully etch the silica and alumina throughout the sample. This was surprising, since previously it was sufficient to simply cleave or scratch a sample (without an alumina layer), to give an exposed edge of silica colloids and enable complete etching. The difference, however, was that previous samples had been assembled from *non*-pre-calcined spheres. We discovered that this simple etching procedure was no longer appropriate when the colloids had been pre-calcined before self-assembly (see Section 3.2). It appears the shrinkage and sintering during post-processing of *non*-pre-calcined colloidal crystals improves the silica interconnectivity, enabling etching by simply cleaving to expose a vertical cross-section. When this approach was attempted with a pre-calcined colloidal crystal without alumina, it was only possible to etch the couple layers of spheres exposed at the cleaved edge (Fig 3.16). If the sample was cleaved again after etching and examined via cross-sectional SEM, it was evident that the etching had not propagated into the sample.

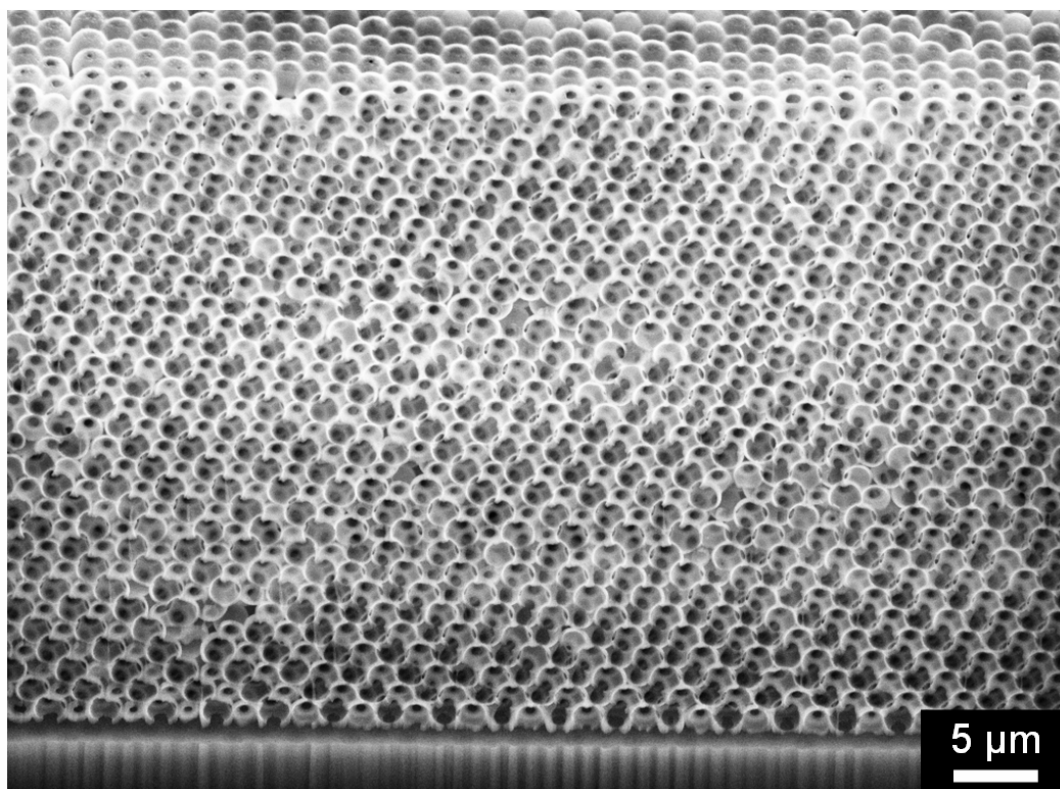


Figure 3.16 SEM micrograph of a scratched then etched edge, cleaned up by focused ion beam milling. When the sample was milled again away from the exposed edge, it was clear that the etching had not actually propagated into the sample.

When trying to etch samples assembled from pre-calcined spheres with an alumina ALD layer by cleaving, several problems with cracking, curling and eventual delamination of the strained silicon inverse opal were encountered (Fig. 3.17). It is possible that the thin alumina layer between the silicon substrate and silicon inverse opal facilitates delamination, as these issues did not arise for previous, *non*-pre-calcined samples that did not have the alumina layer. It is also possible that silicon was grown in previous samples using a different CVD recipe, which may have yielded a less-strained silicon inverse opal.

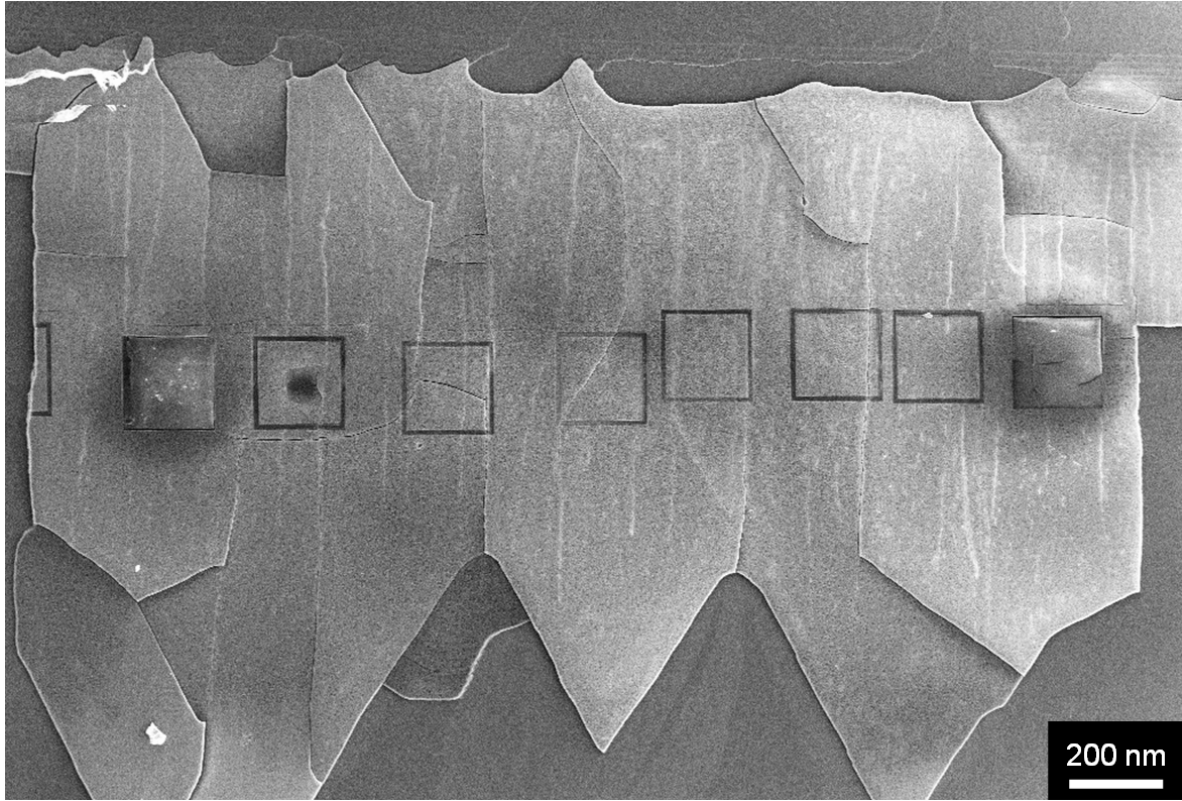


Figure 3.17 SEM micrograph of a silicon inverse opal that has almost finished etching and delaminating from the substrate. The large outlines of boxes are registration marks that enable location embedded features within them.

To solve cracking and liftoff issues, only small regions were selectively etched, using the surrounding silicon-silica-alumina composite (that adheres well to the substrate) to pin down the silicon inverse opal. As etching appears to proceed faster from the top-down (Fig. 3.18), it was possible to simply use a mask to expose only the region to be HF etched during the RIE step (see Section 3.7). The dimensions of the exposed region were on the order of $1 \times 3 \text{ mm}^2$, which was experimentally determined to be small enough to prevent cracking and liftoff during etching for this system.

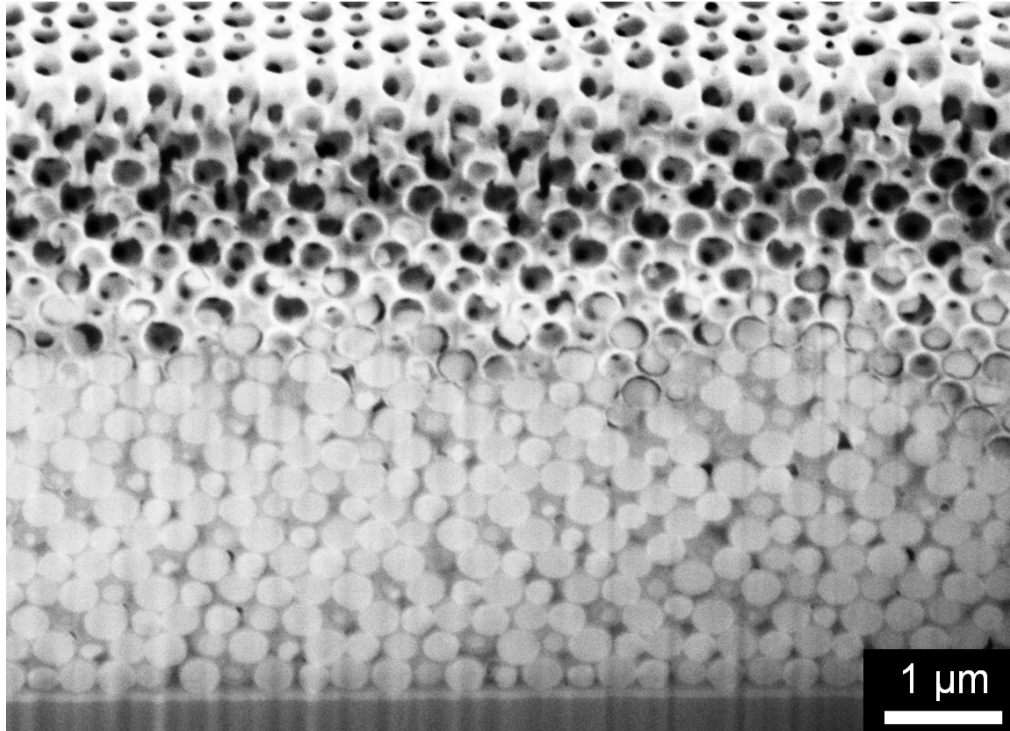


Figure 3.18 Focused ion beam milled cross-section from a partially etched silicon-silica composite in a region that had been exposed with RIE prior to etching.

As HF etching proceeds from the top-down, it was possible to determine the extent of the etch by monitoring the reflectance spectra from the front (top of the photonic crystal) and back (substrate side) of the sample (Fig. 3.19). The reflectance peak was monitored before and after RIE and it was consistently found that the peak reflectance from the front of the crystal decreased after RIE (Fig. 3.19), while the peak from the back, as expected, remained the same. This is understandable as surface truncation plays a major role in coupling to photonic crystals.[20,21] After 30 minutes of etching, the reflectance spectra from the front of the sample has blue-shifted farther than that collected from the back, indicating that the silica and alumina have not yet been completely removed from the bottom of the sample. After 40 minutes, however, the reflection peaks from the front and back of the sample correlate very well and focused ion beam (FIB) milling cross-sections reveal that the sample has been completely etched.

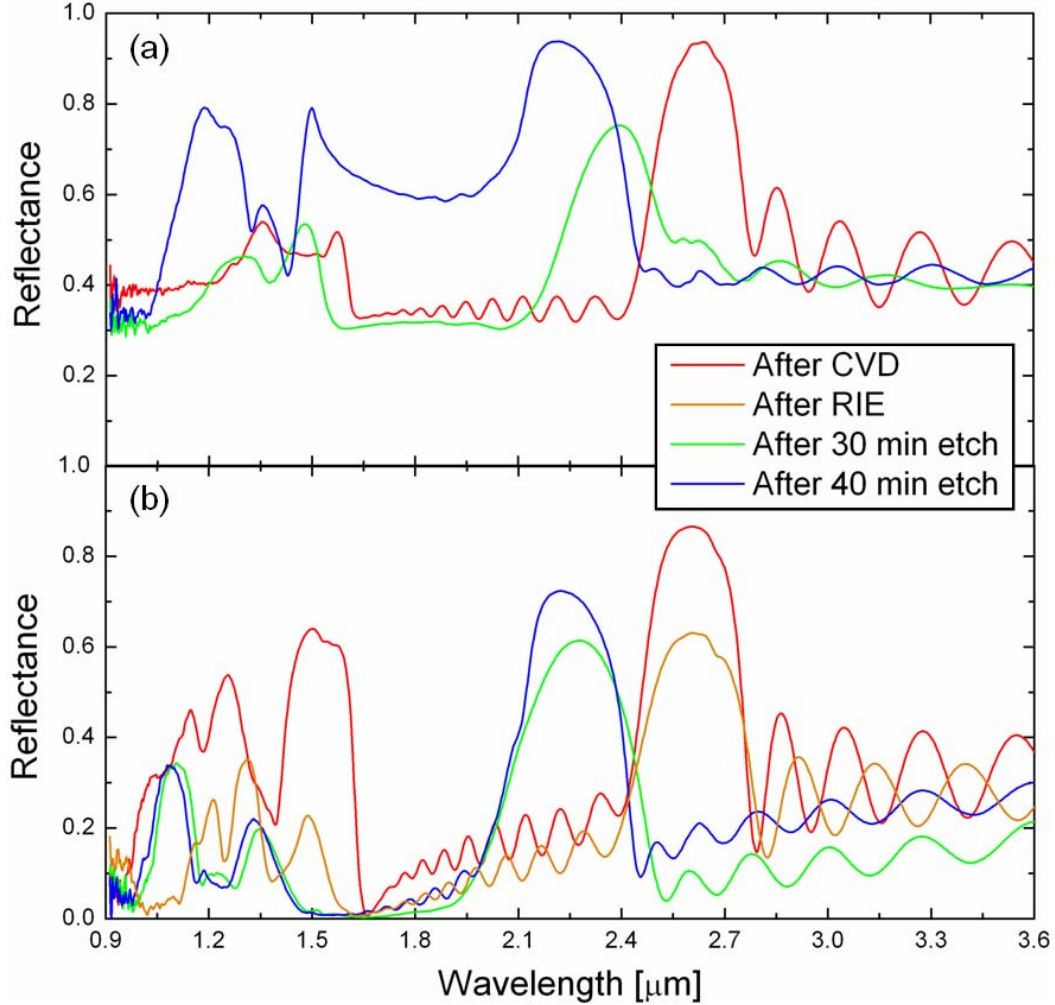


Figure 3.19 Reflectance spectroscopy from the (a) front and (b) back of a photonic crystal assembled from 920 nm spheres after CVD, RIE, and HF etching. All spectra are only normalized to a silver mirror. The reflectance from the silicon substrate is not accounted for, explaining the larger background for spectra collected from the back of the sample.

3.10 Conclusions

In this chapter, a procedure for replicating self-assembled photonic crystals with embedded TPP features in silicon was developed. The ability to incorporate high resolution defects in silicon inverse opals represents a major step forward in providing a platform for the utility of colloidal photonic crystals for cPBG-based applications.

3.11 Experimental

The experimental details relevant to the processing steps discussed in this chapter were included in the appropriate sections. Information on the microscopes and spectrometer used to collect the data will be covered here. Electron micrographs were collected using a conventional SEM (Hitachi S-4700) or a dual-beam FIB microscope (FEI Strata DB-235). When FIB milling a sample we used the si.mtr file with a 5,000-7,000 pA ion aperture for the initial rough cut, followed by a 100-300 pA aperture for the cleaning cross-section. Typical milling times ranged from about 1 to 2 hours per location. Micro-spot spectroscopy[22] was taken typically using a 4x, 0.1 NA objective on a optical microscope (Hyperion 2000, Bruker) with output coupled to an FTIR spectrometer (Vertex 70, Bruker). Reflection spectra were normalized to a protected silver mirror specified to have $\geq 95\%$ reflectivity over the wavelength range typically used (Melles Griot, Rochester, NY). Transmission spectra were normalized to the transmission collected through a spot on the same double-side polished silicon wafer from a region without a colloidal crystal. The collection spot size is on the order of 75-150 μm .

3.12 References

1. Y. H. Jun, C. A. Leatherdale, D. J. Norris, *Adv. Mater.* **2005**, *17*, 1908.
2. W. Stober, A. Fink, E. Bohn, *J. Colloid Interfac. Sci.* **1968**, *26*, 62.
3. F. J. Arriagada, K. Osseo-Asare, *J. Colloid Interfac. Sci.* **1999**, *211*, 210.
4. H. Giesche, *J. Eur. Ceram. Soc.* **1994**, *14*, 205.
5. A. A. Chabanov, Y. Jun, D. J. Norris, *Appl. Phys. Lett.* **2004**, *84*, 3573.
6. F. Garcia-Santamaria, H. Miguez, M. Ibisate, F. Meseguer, C. Lopez, *Langmuir* **2002**, *18*, 1942.
7. P. Jiang, J. F. Bertone, K. S. Hwang, V. L. Colvin, *Chem. Mater.* **1999**, *11*, 2132.

8. Y. A. Vlasov, X. Z. Bo, J. C. Sturm, D. J. Norris, *Nature* **2001**, 414, 289.
9. D. J. Norris, E. G. Arlinghaus, L. L. Meng, R. Heiny, L. E. Scriven, *Adv. Mater.* **2004**, 16, 1393.
10. K. Busch, S. John, *Phys. Rev. E* **1998**, 58, 3896.
11. Band diagrams were calculated using MIT Photonic Bands.
12. S. G. Johnson, J. D. Joannopoulos, *Opt. Express* **2001**, 8, 173.
13. F. Garcia-Santamaria, P. V. Braun, *private communication*.
14. H. Miguez, F. Meseguer, C. Lopez, A. Blanco, J. S. Moya, J. Requena, A. Mifsud, V. Fornes, *Adv. Mater.* **1998**, 10, 480.
15. H. Miguez, N. Tetreault, B. Hatton, S. M. Yang, D. Perovic, G. A. Ozin, *Chem. Commun.* **2002**, 2736.
16. A. Blanco, E. Chomski, S. Grabtchak, M. Ibisate, S. John, S. W. Leonard, C. Lopez, F. Meseguer, H. Miguez, J. P. Mondia, G. A. Ozin, O. Toader, H. M. van Driel, *Nature* **2000**, 405, 437.
17. F. Garcia-Santamaria, M. Ibisate, I. Rodriguez, F. Meseguer, C. Lopez, *Adv. Mater.* **2003**, 15, 788.
18. V. Lousse, S. H. Fan, *Opt. Express* **2006**, 14, 866.
19. N. T  treault, G. von Freymann, M. Deubel, M. Hermatschweiler, F. P  rez-Willard, S. John, M. Wegener, G. A. Ozin, *Adv. Mater.* **2006**, 18, 457.
20. J.-A. Hiller, J. D. Mendelsohn, M. F. Rubner, *Nat. Mater.* **2002**, 1, 59.
21. Y. A. Vlasov, S. J. McNab, *Opt. Lett.* **2006**, 31, 50.
22. Y. A. Vlasov, M. Deutsch, D. J. Norris, *Appl. Phys. Lett.* **2000**, 76, 1627.

CHAPTER 4

CHARACTERIZATION OF EMBEDDED DEFECTS

4.1 Microscopy of Defects in Silicon Inverse Opals

Electron microscopy and focused ion beam milling have been critical to the diagnosis of issues that have arisen in processing these samples (Chapter 3), as well as to the demonstration of the successful replication of embedded TPP features as air defects in silicon-air inverse opals. In Figure 4.1, a TPP feature was written to the top of a colloidal crystal, to enable SEM imaging of the horizontal feature. While a portion of the feature was damaged while handling the somewhat fragile silicon-air inverse opal (Fig. 4.1a), it is clear that this was a high fidelity replication of the initial TPP feature (Fig. 4.1c). Although this feature was written without attempting to minimize the linewidth, the linewidth was less than a colloid diameter (Fig. 4.1d), which may be sufficient to define features of interest to the photonic crystals community.

Features that were defined in vertical cross-sections were imaged after FIB milling (Fig. 4.2). Similar linewidths were observed in the FIB images of these features, however the edges did not appear as clean as in the features written at the top of the photonic crystal (Fig. 4.1). As discussed in Section 3.8, this may be attributed to redeposition during FIB milling and/or the lack of a clean burn when attempting to remove embedded polymer features. More work will need to be done to determine this. Should there be a problem burning out the polymer, it is possible to either leave it in or remove it via oxygen plasma etching. It is also evident upon examination of these micrographs, as well as from observations during in situ imaging on the confocal, that there may be issues generating polymer adjacent to the substrate, something that might be expected due to the high reflectivity of the silicon substrate.

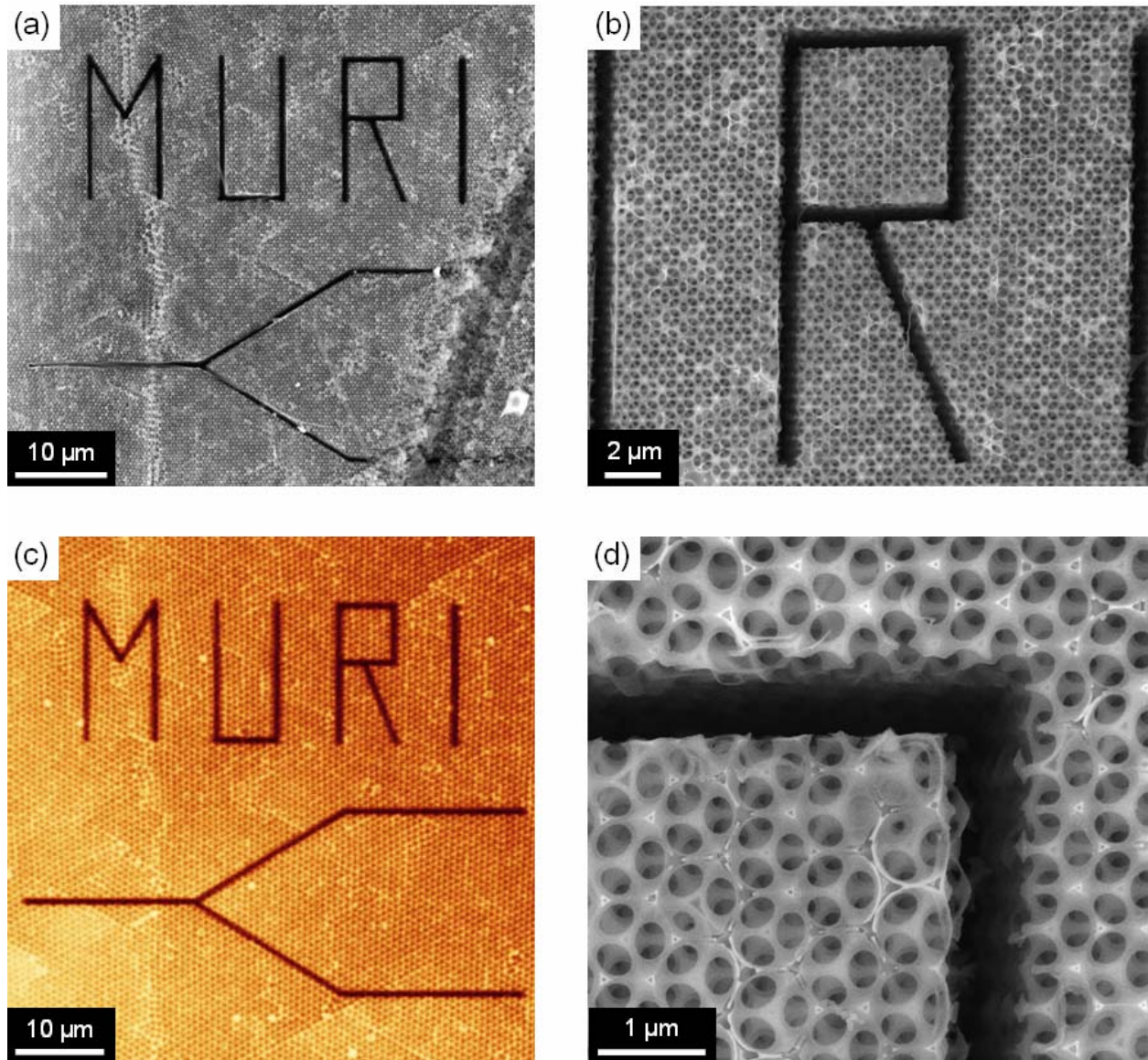


Figure 4.1 (c) In-situ fluorescence laser scanning confocal micrograph showing a TPP feature written horizontally to the top of a colloidal crystal. (a,b,d) SEM micrographs demonstrating the high quality replication of the TPP feature in (c) as an air defect in a silicon-air inverse opal. The large openings that interconnect the top layer with the layer below (d) can be partly attributed to the alumina layer that was grown before silicon CVD and then removed via wet etching. However, in this case, the sample was also overetched. It is also apparent in (a) that the sample was damaged during handling. It was observed that the silicon-air inverse opal is much more fragile and less resistant to scratching than its precursor, the silicon-silica colloidal photonic crystal.

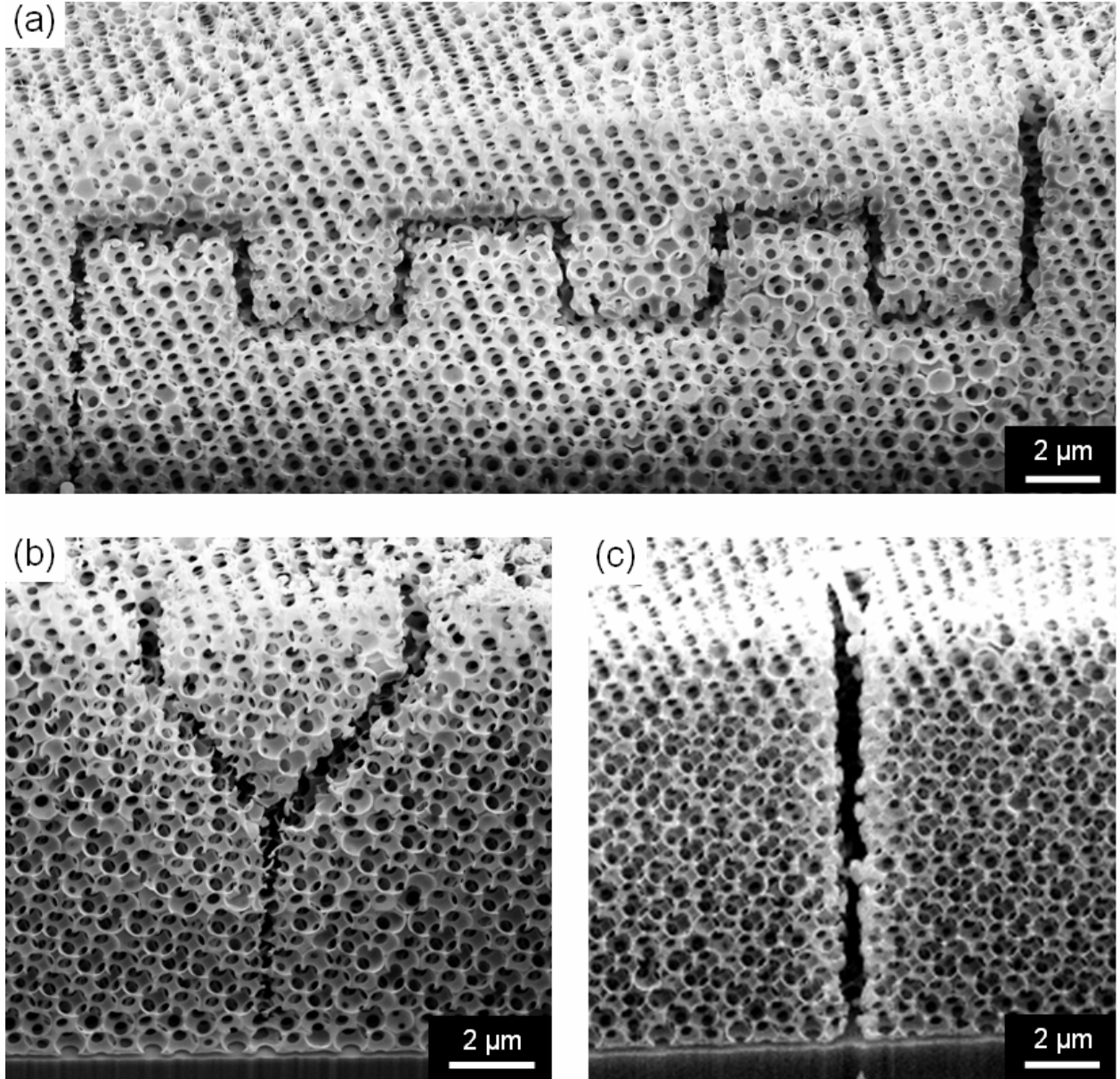


Figure 4.2 FIB cross-sections taken through silicon-air inverse opals with embedded air defects. Here, the TPP features were defined vertically in a colloidal crystal.

4.2 Spectroscopy from Embedded Planar Defects

It has also been interesting to monitor the spectroscopy from planar defects (Fig. 4.3), which are large in their lateral dimensions ($150 \times 150 \mu\text{m}^2$), but only on the order of one to several colloid diameters thick, that are embedded within the photonic crystal. Using multiple

step deposition procedures, embedded planar defects have been previously incorporated in colloidal crystals (see Section 1.10.2).[1-3]

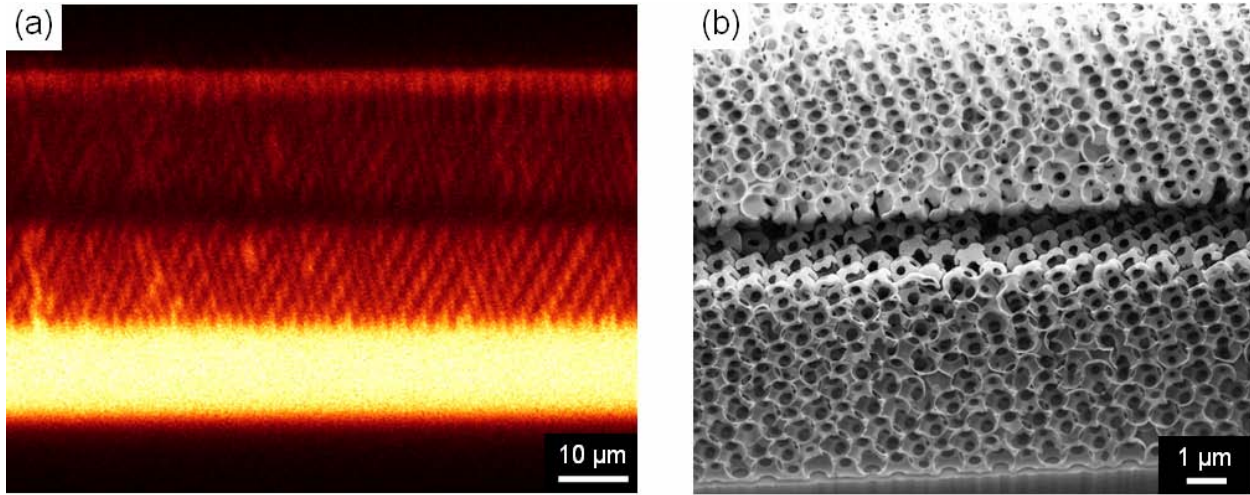


Figure 4.3 (a) Fluorescence confocal and (b) FIB vertical cross-sections through planar defects embedded within colloidal photonic crystals. On the left, the substrate is at the top as the sample was inverted before mounting it on the LSCM for TPP.

Here, TPP was used to write embedded planar defects in silica colloidal crystals (Fig. 4.3a), which were then filled with silicon and inverted (Fig. 4.3b). Micro-spot spectroscopy was used to interrogate the optical properties of these embedded defects throughout all of the processing steps. As expected, a dip in the first order reflectance peak, and a corresponding peak in the first order transmittance dip were observed. This indicates that light of the wavelength corresponding to the notch, is coupling to the embedded planar defect. The wavelength that is supported by the defect depends on its thickness and refractive index. The magnitude of its notch depends on its thickness, as well as the number of layers and the photonic strength of the photonic crystal on either side of the defect. Such trends become apparent upon monitoring the diffraction spectra for defects embedded within samples with different lattice parameters, thicknesses, and photonic strengths (Figs 4.4, 4.5).

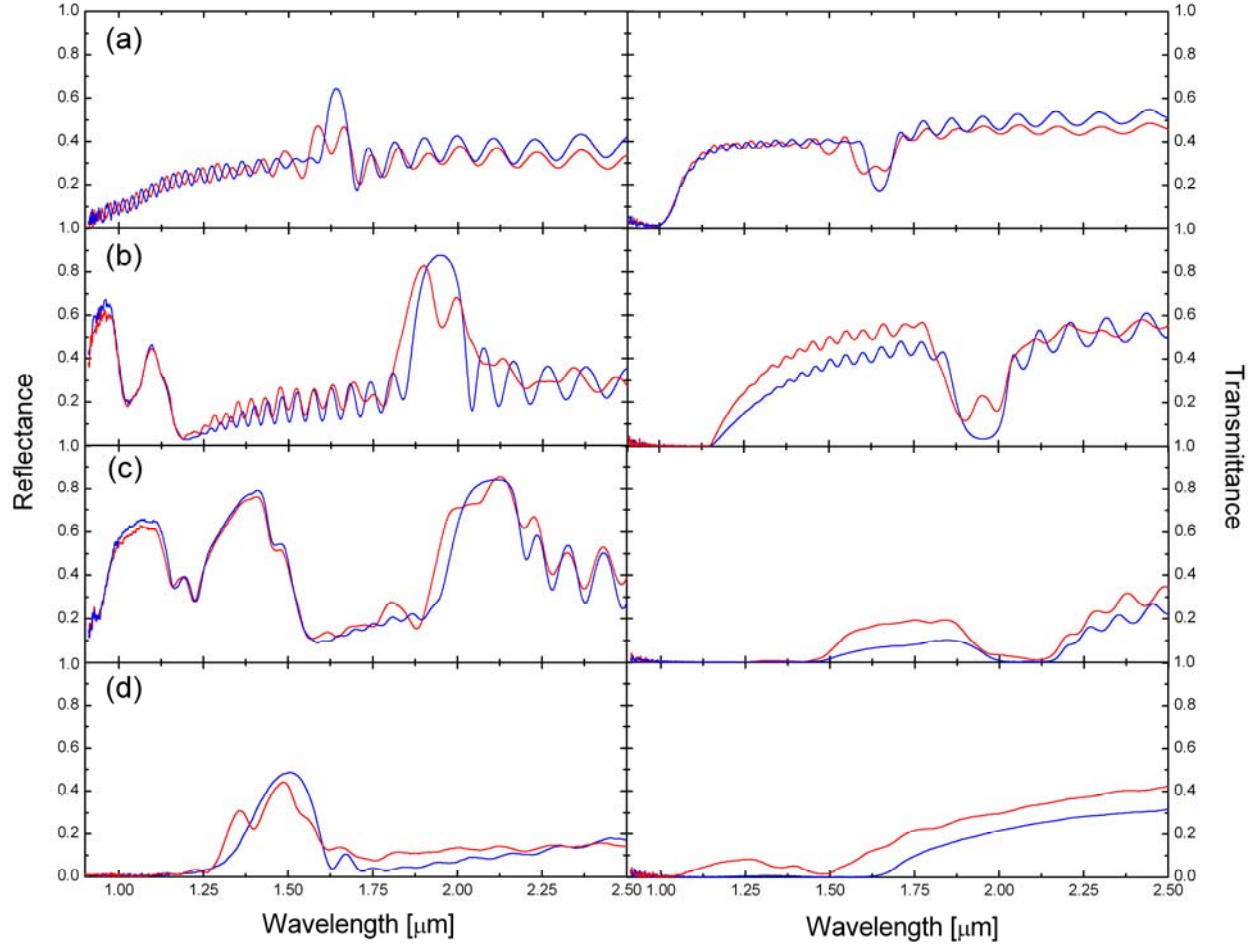


Figure 4.4 Reflection (left) and transmission (right) spectroscopy collected from a colloidal photonic crystal (blue) and a defect embedded within it (red). Spectra were taken (a) directly after TPP of the defect in a colloidal crystal assembled from silica microspheres (~ 720 nm diameter) after ALD of an ~ 13 nm thick alumina layer, (b) after one cycle of silicon CVD, (c) after a second cycle of silicon CVD, and (d) after RIE to expose the silica colloids, burning to remove the polymer, and HF etching to remove the silica and alumina. The sample was over-etched, explaining the low reflectivity for the final silicon-air inverse opal structure. Reflection spectra were normalized to a silver mirror and transmission spectra were normalized to the transmittance through air.

As the photonic strength of the surrounding photonic crystal increases (for example from Fig. 4.4b to c), the relative magnitude of the notch decreases. The higher photonic strength

prevents light from propagating as deep into the photonic crystal, which means that less light couples to the embedded defect and its impact on the resultant spectra is lessened.

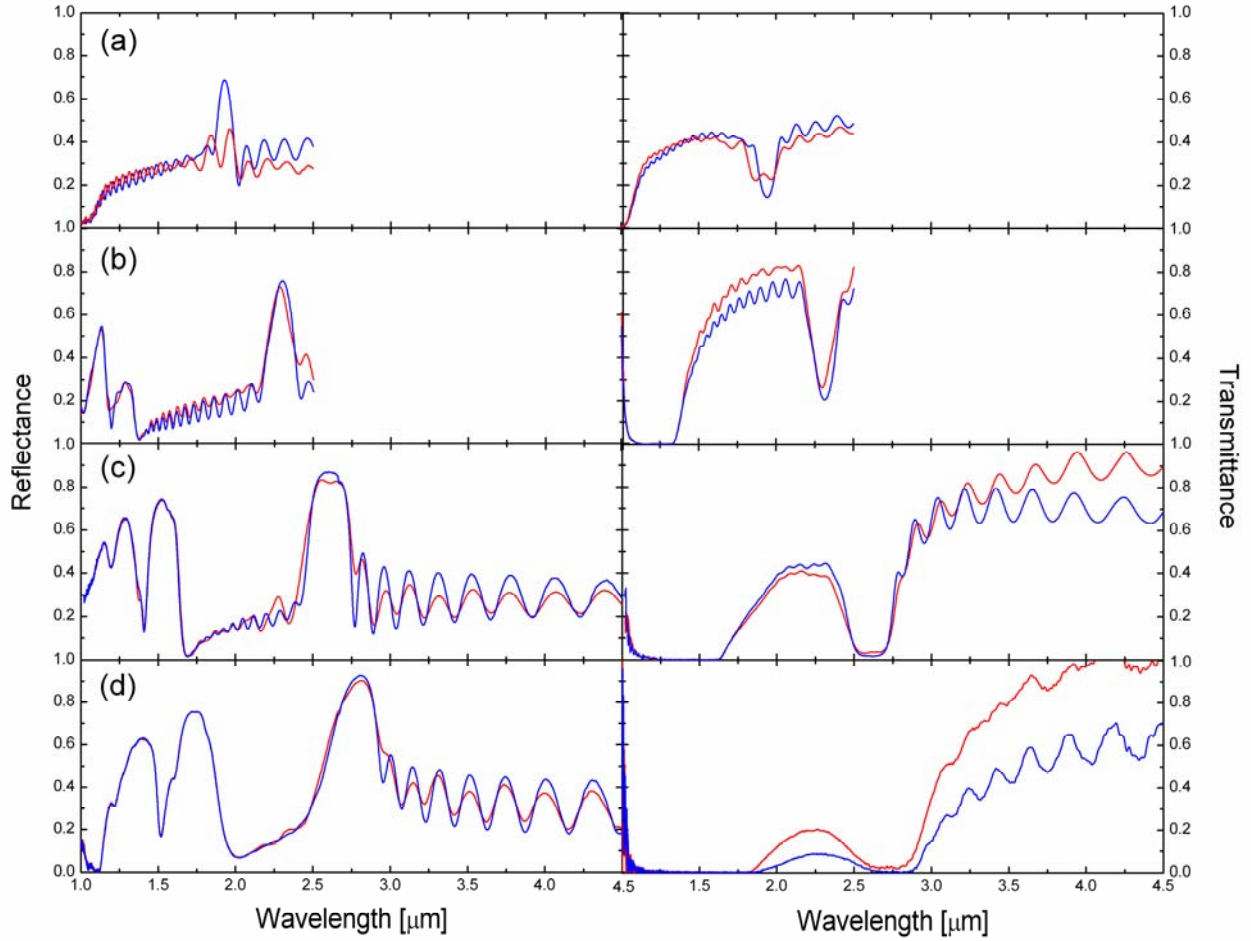


Figure 4.5 Reflection (left) and transmission (right) spectroscopy collected from a colloidal photonic crystal (blue) and a defect embedded within it (red). Spectra were taken (a) directly after TPP of the defect in a colloidal crystal assembled from silica microspheres (~ 920 nm diameter) after ALD of an ~ 8 nm thick alumina layer, (b) after one cycle of silicon CVD, (c) after a second cycle of silicon CVD, and (d) a third cycle of silicon CVD. Reflection spectra were all normalized to a silver mirror. The transmission spectra in (a) were normalized to the transmittance of air, and those in (b,c,d) were normalized to the transmittance through a double-side polished silicon wafer.

4.3 IR Transmission Microscopy Through Defects

IR transmission micrographs confirm the spectroscopy and SEM results. For example, in Figure 4.6a, left and 4.6b, middle, micrographs were collected from regions where embedded planar defects were written. The embedded defects show up brighter than the surrounding photonic crystal region because more light is being transmitted through those areas. As the IR camera is collecting wavelengths from ~ 1.1 to $1.7\ \mu\text{m}$, it is not due to only those wavelengths that are supported by the defect (Fig. 4.4c,d), but is primarily because of the higher background transmittance collected from the embedded planar defect regions when compared with that from the photonic crystal. In the future a notch filter could be used to image only those wavelengths supported by the defect, though as this does not provide much more information than the spectroscopy that can be collected, it is likely not necessary. The thin outline surrounding the embedded planar defects was written at the top of the photonic crystal to enable the defects to be located by eye in reflectance mode on the FTIR microscope.

Defects extending through the photonic crystal were also imaged via IR transmission microscopy (Figs 4.6a, right; 4.6b, left; and 4.6b, right). Since the second order diffraction peak is both below the absorption edge of silicon and is below collection window of the IR camera, this does not demonstrate waveguiding due to a photonic bandgap. Currently in our group, straight and double-bend features are being written through colloidal crystals assembled from larger silica microspheres ($\sim 920\ \text{nm}$ in diameter), to place the second order diffraction peak of the resultant silicon inverse opal around $1.5\ \mu\text{m}$. IR transmission micrographs collected from such features, using a notch filter at the bandgap wavelength, would demonstrate waveguiding in a material capable of possessing a cPBG.

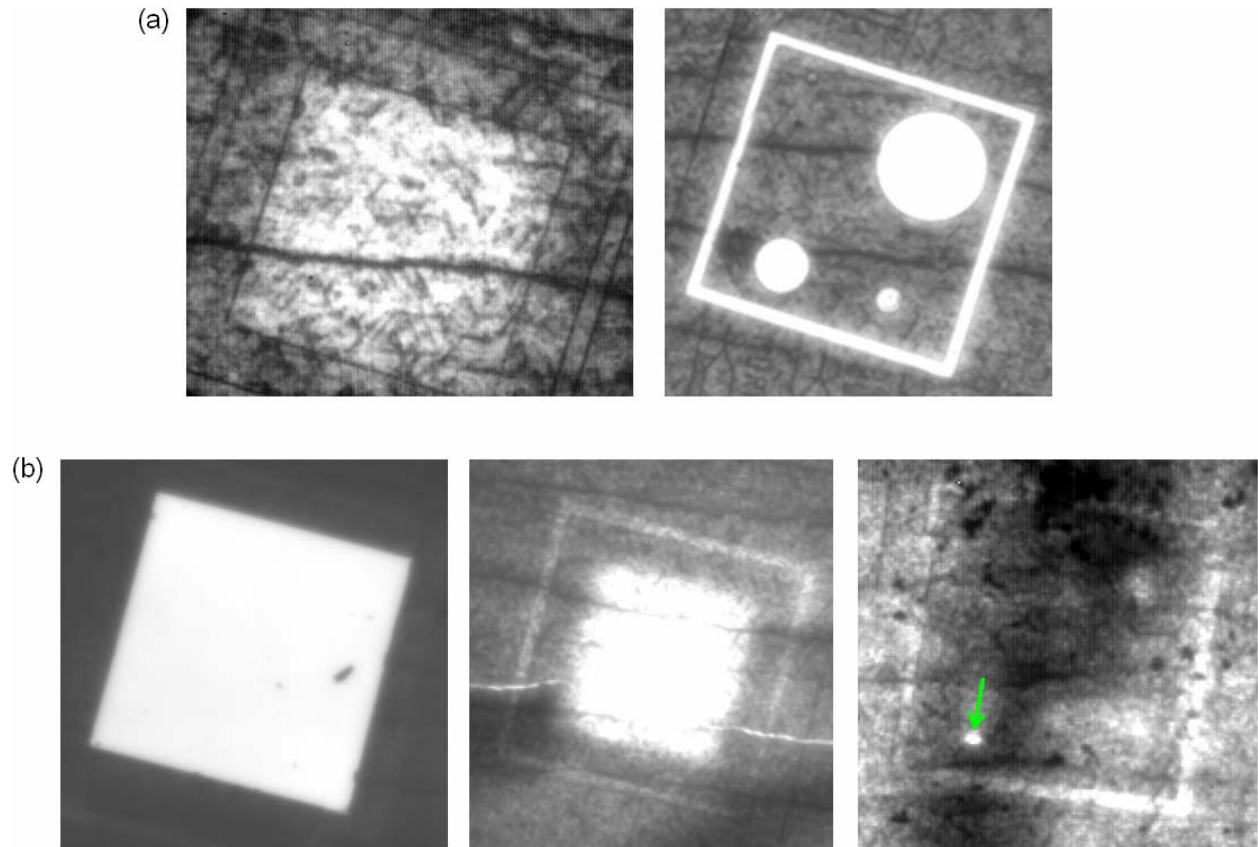


Figure 4.6 IR transmission micrographs collecting light ($\lambda \sim 1.1$ to $1.7 \mu\text{m}$) from defects embedded within (a, left and b, middle) or extending through the thickness of (a) silicon-silica-alumina-polymer composites and (b) silicon air inverse opals. The green arrow (b, right) indicates an air defect that is $4 \times 10 \mu\text{m}^2$ in its cross-sectional area, that extends through the thickness of the silicon-air inverse opal. The colloidal crystal template was assembled from 720 nm diameter spheres.

4.4 Conclusions

SEM and FIB were used to demonstrate the high fidelity replication of high resolution TPP features as air defects in silicon air inverse opals. Further, optical spectroscopy was collected from planar defects embedded within silicon colloidal photonic crystals. Finally, IR transmission micrographs from embedded and through features within silicon photonic crystals were presented.

4.5 References

1. E. Palacios-Lidon, J. F. Galisteo-Lopez, B. H. Juarez, C. Lopez, *Adv. Mater.* 2004, *16*, 341.
2. N. Tetreault, A. Mihi, H. Miguez, I. Rodriguez, G. A. Ozin, F. Meseguer, V. Kitaev, *Adv. Mater.* 2004, *16*, 346.
3. B. Z. Wang, W. Zhao, A. Chen, S. J. Chua, *J. Crystal Growth* 2006, 288, 200.

CHAPTER 5

TPP IN HOLOGRAPHIC PHOTONIC CRYSTALS

Significant components of this section were published as P. V. Braun, S. A. Pruzinsky-Rinne, F. García-Santamaría “Introducing Defects in 3D Photonic Crystals: State of the Art” *Advanced Materials* **2006**, *In Press*.

5.1 Introduction to Holography

The concept of holographic lithography for photonic crystal fabrication was first demonstrated by Berger *et al.* and is deceptively simple.[1] Inherently, it consists of recording the hologram created by the interference of multiple beams of light into a photoresist (Fig. 5.1a). The photoresist used in many studies is SU-8, due to its low intrinsic absorption and capability for forming sub-micron features.[2] Upon exposure, acid is generated to form a latent image of the interference pattern within the photoresist (Fig. 5.1b). During baking, the acid drives a polymerization reaction and after development a 3D polymer network remains (Fig. 5.1c).

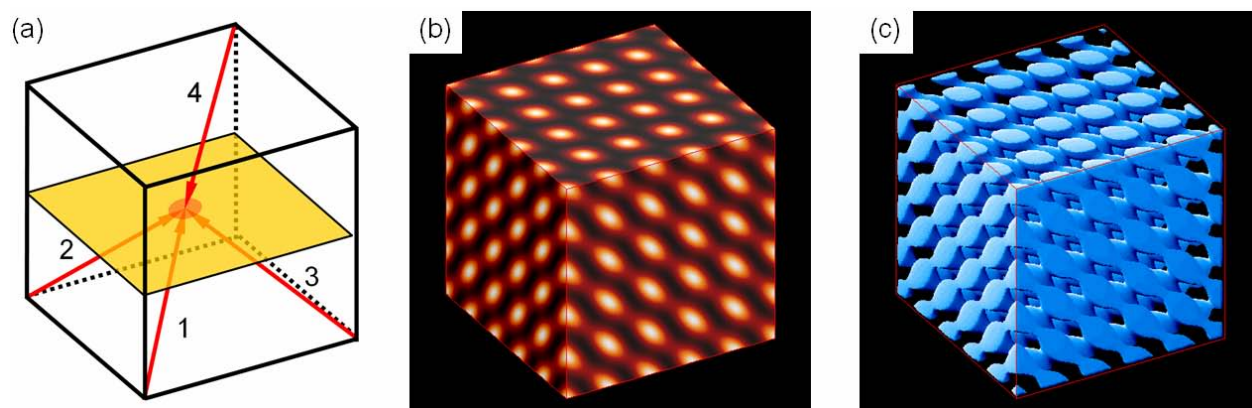


Figure 5.1 (a) Schematic of four beams interfering within a sample, and computer rendering of (b) a latent acid image generated upon exposure, and (c) the resultant 3D polymer network. Images courtesy of James W. Rinne.

5.2 Holographic Photonic Crystals

Holographic lithography is an attractive means for 3D photonic crystal fabrication as it is capable of producing large-area, thick, defect-free, 3D periodic structures (Fig 5.2).[3] Further, it enables the definition of any Bravais lattice and it is a parallel technique, amenable to large scale production. As such, holography has the potential to become a leading 3D photonic crystal fabrication technique.

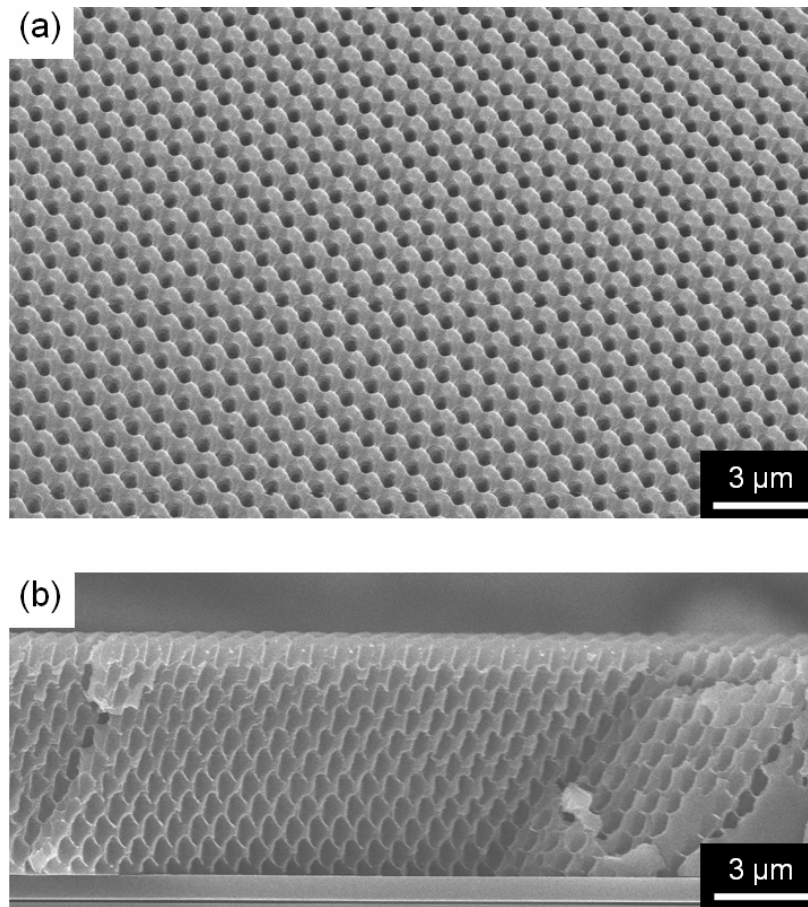


Figure 5.2 SEM images of (a) the top and (b) a cross-section taken from an FCC-like holographic photonic crystal fabricated with a 532 nm laser. Micrographs courtesy of Ying-Chieh Chen.

In holographic lithography, the minimum number of beams required to form a n -dimensional lattice is $n+1$, thus four beams are required to obtain 3D photonic crystals with this

technique. The optical setup (Fig. 5.3) and processing details are quite involved, which explains why there are not many academic research groups working on 3D holographic photonic crystals.

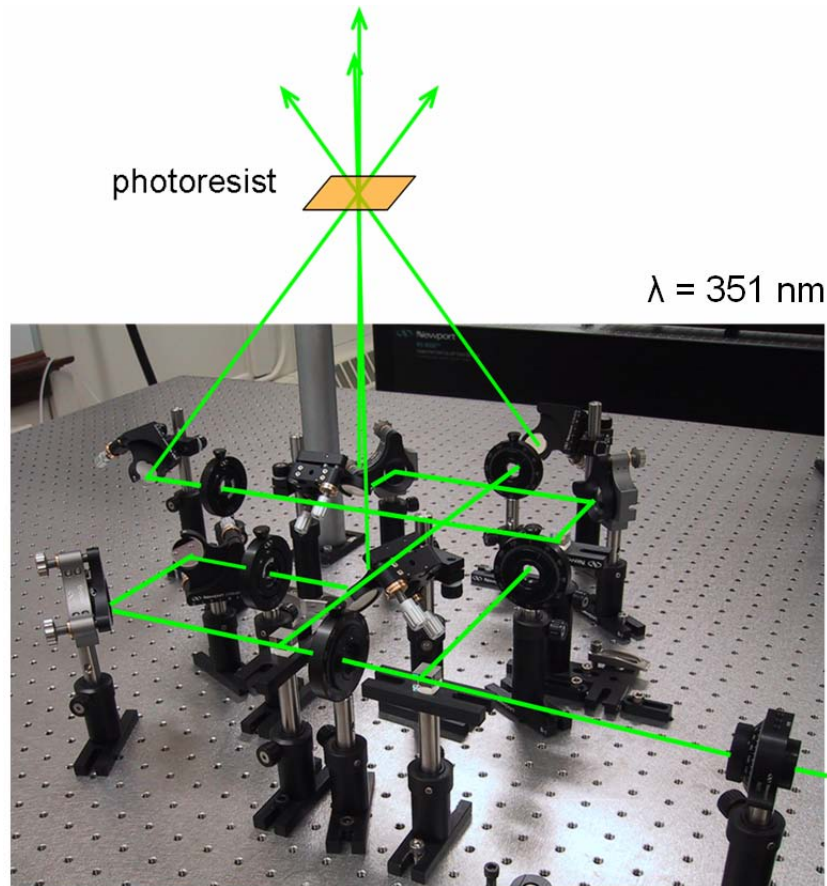


Figure 5.3 Picture of an early optical setup used to obtain 3D holographic photonic crystals. Courtesy of Ying-Chieh Chen.

Further, the optical properties of 3D photonic crystals formed via holography are weaker than expected for reasons that are not obvious. There are only limited reports on the optical response of these structures[4] and although a direct comparison is difficult, to date, it appears that colloidal crystals present better optical properties. The optical response of holographic structures could be improved by better lasers, photoresists, and processing parameters, but these improvements are not trivial. These issues become even more important as the number of interfering beams increase to form more complex structures (e.g. diamond or chiral lattices).[5,6]

An equally significant issue is that the refractive index of common photoresists are too low to open a cPBG regardless of the structure, thus replicating the structures with high refractive index materials is essential. Recent advances in replicating polymeric templates into silicon structures[7,8] indicate possible routes to create structures with enhanced refractive index contrast. Also, very recently, Summers *et al.*[9] demonstrated the use of atomic layer deposition to replicate the structure of a holographic photonic crystal into TiO_2 , a high refractive index material which is transparent in the visible (Fig. 5.4). Finally, since the exposure wavelength is directly proportional to the lattice parameter of the crystal and therefore the spectral region where the structure will exhibit a cPBG, the chemistry of the photo-initiating system may need to be changed to tune the spectral position of the optical features. Although possible, this not a trivial task.[10]

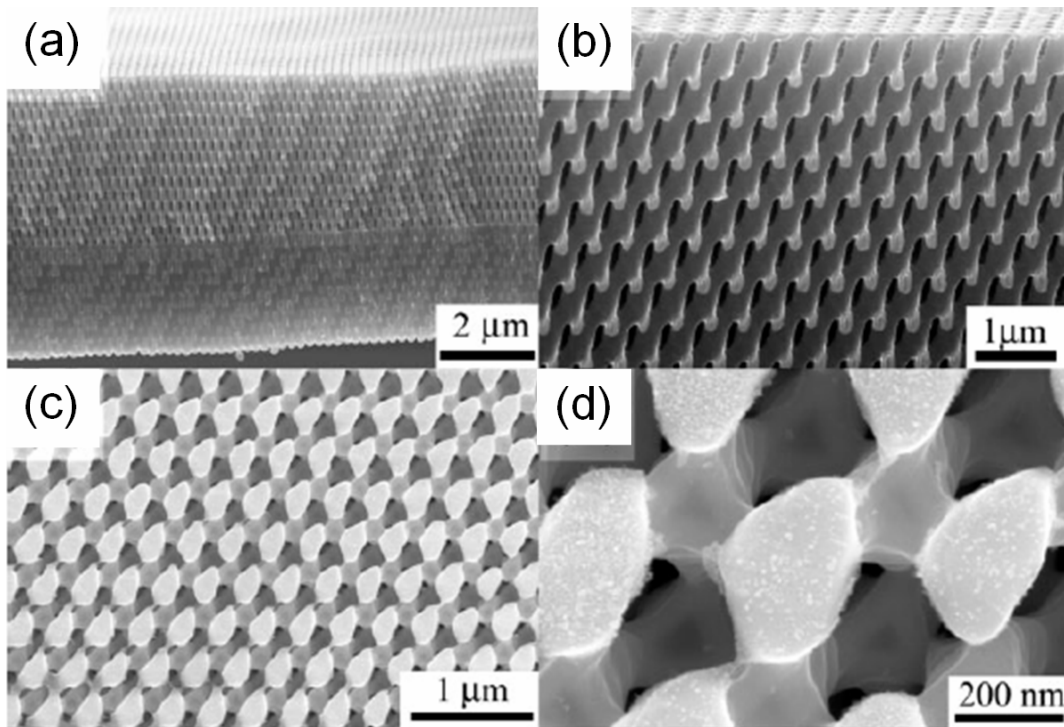


Figure 5.4 SEM images from (a,b) cross-sections and (c,d) the top of an inverted TiO_2 photonic crystal after removing the initial holographic photonic crystal template via an oxygen plasma etch.[9]

5.3 Phase Mask Holographic Lithography

A variant to holographic lithography in which interference is created from a phase mask, as opposed to multiple beam interference, has been developed by Rogers *et al.*[11] The phase mask is first defined in a ‘master’, fabricated by photo-lithography. This master is used to create a PDMS flexible phase mask. The PDMS phase mask is placed in direct contact with the surface of a photoresist (SU-8) and illuminated with ultraviolet light, resulting in a complex 3D intensity distribution within the photoresist (**Fig. 5.5**).

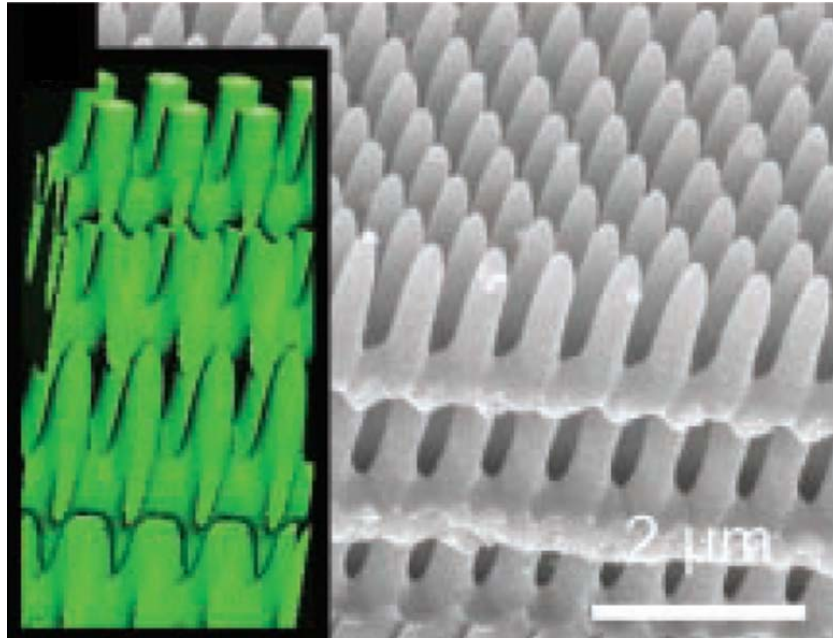


Figure 5.5 SEM of a 3D periodic structure fabricated via phase mask lithography with the corresponding optical intensity distribution calculation as an inset.[11]

The direct contact between the mask and photoresist removes the need for the complicated alignment and vibration control, typically required in conventional multi-beam holographic setups. In addition to its simplicity, cost-effectiveness, and potential for scale-up, phase mask lithography also enables the definition of intrinsic defects. These can be obtained by creating a defect in the original 2D master template.[11]

5.4 Defects in Holographic Photonic Crystals

Preliminary work has also shown that TPP can also be used to incorporate aperiodic defects within photonic crystals defined by multibeam holography.[12,13] In our first attempt, an SU8-based photoresist was exposed to two interfering beams and then baked to crosslink the exposed regions before TPP writing (Fig 5.5a). This introduced a slight index contrast within the resin, enabling visualization of the photonic crystal via reflectance confocal microscopy during the TPP writing. This also facilitated the alignment of TPP features with the underlying photonic crystal lattice (Fig. 5.5b).

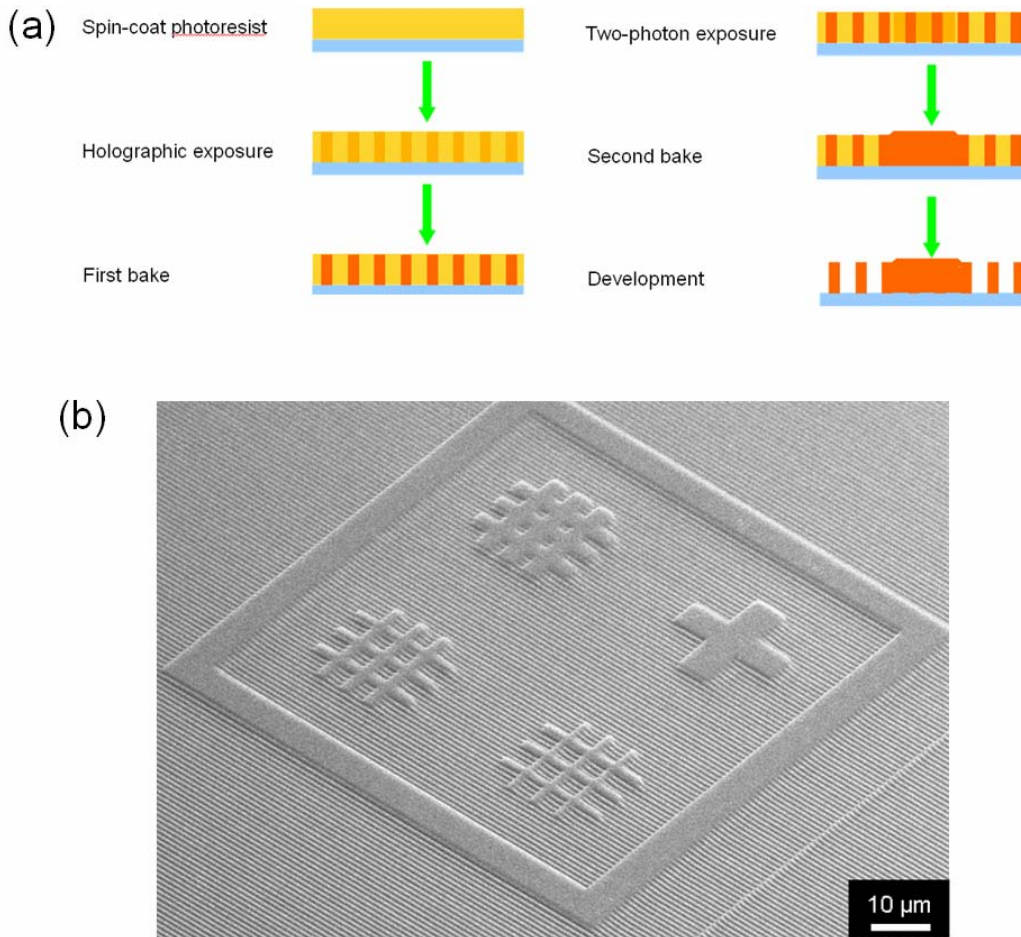


Figure 5.5 (a) Schematic of experimental procedure and (b) SEM micrograph from our first successful attempt to write TPP defects within a 2D photonic crystal. Schematic and SEM courtesy of Ying-Chieh Chen.

Since our initial attempt, Scrimgeour *et al.*[13] have demonstrated TPP in 3D holographic photonic crystals. They added an acid-sensitive dye, coumarin 6, to the SU-8 photoresist so that the latent acid image in the holographic photonic crystal could be visualized via fluorescence confocal microscopy (Fig. 5.6). This is more appealing than reflectance-based imaging as it enables cleaner, 3D imaging of the structure, which was necessary when writing in 3D photonic crystals.

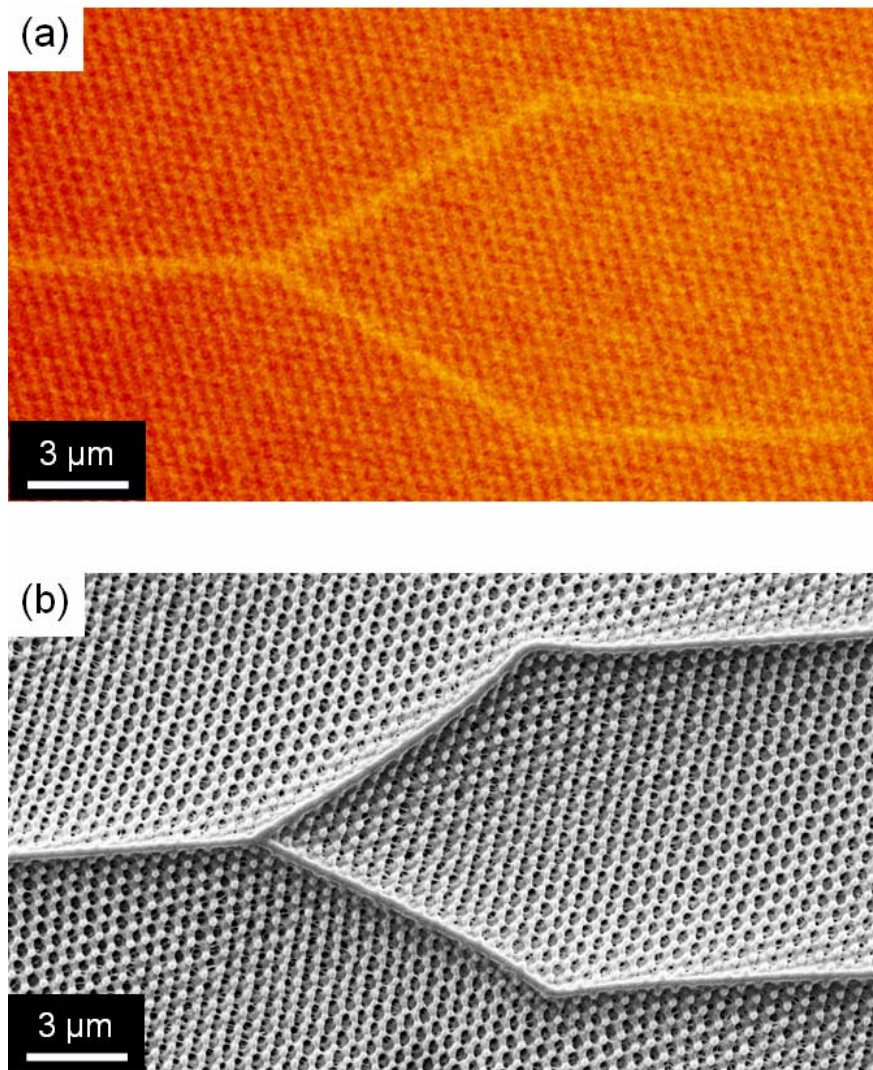


Figure 5.6 (a) Fluorescence confocal and (b) SEM micrographs taken from a TPP feature that was written to the top surface of a 3D holographic photonic crystal.

It is apparent from the SEM images in this chapter that the TPP features protrude from the top of the photonic crystal. This was unexpected, as both the photonic crystal and the TPP feature were written to the top of the photoresist. However, several things are evident upon examining an FIB cross section through a feature written vertically in a photonic crystal (Fig. 5.7). First, the TPP feature is wider than intended, though the fluorescence confocal micrograph taken during TPP of this feature indicated a similar linewidth ($\sim 0.25\ \mu\text{m}$) as in Figure 5.6a. It is possible that the TPP exposure not only generates acid, but also bleaches the coumarin 6. In this case, choosing a TPP exposure dose to match the fluorescence intensity of the feature with that of the surrounding photonic crystal would result in linewidth broadening. It is also evident that the photonic crystal has experienced shrinkage in the vertical dimension compared with the TPP feature. Finally, it should be noted that as this structure is susceptible to damage during FIB milling, it is best to use low milling currents to obtain a cleaner final image than that in Fig. 5.7.

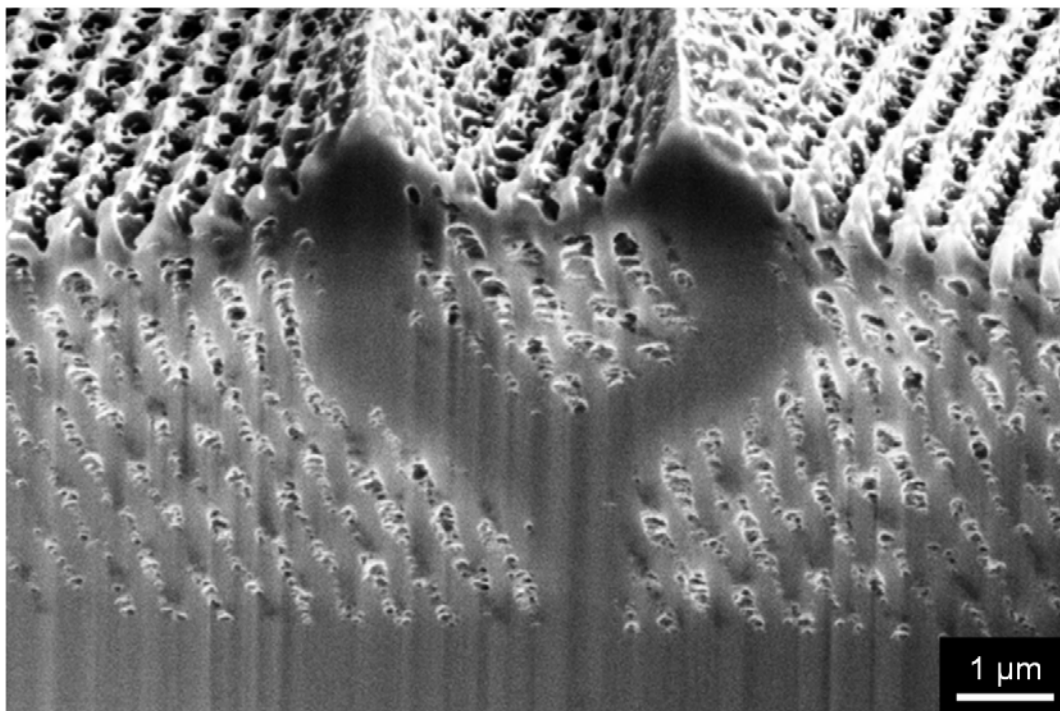


Figure 5.7 FIB cross-section through a y-splitter feature written vertically in a 3D holographic photonic crystal.

5.5 Conclusions and Outlook

While holographic lithography is an attractive 3D photonic crystal fabrication route, better characterization of the optical properties of holographic photonic crystals is needed. It would also be interesting to see a study that discusses the nuances of 3D holographic lithography, for example, the sensitivity of the final structure to vibrations or other sources of experimental error, along with commentary on the reproducibility and reliability of this technique. Finally, though the TPP of defects within holographic photonic crystals has been demonstrated, further development is required.

5.6 Experimental

Holographic photonic crystals are fabricated by the Wiltzius research group with some modifications from that described by Yang et al.[14]. Experimental details for TPP were covered in Chapter 2, and those for SEM and FIB were covered in Chapter 3.

5.7 References

1. V. Berger, O. GauthierLafaye, E. Costard, *J. Appl. Phys.* **1997**, 82, 60.
2. K. Y. Lee, N. LaBianca, S. A. Rishton, S. Zolgharnain, J. D. Gelorme, J. Shaw, T. H. P. Chang, *J. Vac. Sci. Technol. B* **1995**, 13, 3012.
3. M. Campbell, D. N. Sharp, M. T. Harrison, R. G. Denning, A. J. Turberfield, *Nature* **2000**, 404, 53.
4. Y. V. Miklyaev, D. C. Meisel, A. Blanco, G. von Freymann, K. Busch, W. Koch, C. Enkrich, M. Deubel, M. Wegener, *Appl. Phys. Lett.* **2003**, 82, 1284.
5. J. H. Moon, S. Yang, D. J. Pine, S. M. Yang, *Opt. Express* **2005**, 13, 9841.
6. Y. K. Pang, J. C. W. Lee, H. F. Lee, W. Y. Tam, C. T. Chan, P. Sheng, *Opt. Express* **2005**, 13, 7615.
7. G. M. Gratson, F. Garcia-Santamaria, V. Lousse, M. Xu, S. H. Fan, J. A. Lewis, P. V. Braun, *Adv. Mater.* **2006**, *In Press*.

8. N. Tétreault, G. von Freymann, M. Deubel, M. Hermatschweiler, F. Pérez-Willard, S. John, M. Wegener, G. A. Ozin, *Adv. Mater.* **2006**, *18*, 457.
9. J. S. King, E. Graugnard, O. M. Roche, D. N. Sharp, J. Scrimgeour, R. G. Denning, A. J. Turberfield, C. J. Summers, *Adv. Mater.* **2006**, *In Press*.
10. S. Yang, M. Megens, J. Aizenberg, P. Wiltzius, P. M. Chaikin, W. B. Russel, *Chem. Mater.* **2002**, *14*, 2831.
11. S. Jeon, J. U. Park, R. Cirelli, S. Yang, C. E. Heitzman, P. V. Braun, P. J. A. Kenis, J. A. Rogers, *Proc. Natl. Acad. Sci. U. S. A.* **2004**, *101*, 12428.
12. N. D. Lai, W. P. Liang, J. H. Lin, C. C. Hsu, *Opt. Express* **2005**, *13*, 5331.
13. J. Scrimgeour, D. N. Sharp, C. F. Blanford, O. M. Roche, R. G. Denning, A. J. Turberfield, *Adv. Mater.* **2006**, *In Press*.
14. S. Yang, M. Megens, J. Aizenberg, P. Wiltzius, P. M. Chaikin, W. B. Russel, *Chem. Mat.* **2002**, *14*, 2831.

CHAPTER 6

CONCLUSIONS

TPP was adapted for use within colloidal crystals to embed pre-defined, 3D features with submicron resolution. These features act as defects which disrupt the otherwise periodic structure and provide functionality in PBG materials. The controllable incorporation of defects in PBG materials is necessary for the realization of most PBG-based applications. Specific functionalities can be tailored by engineering the defect geometry and placement within the crystal. Therefore, the demonstration of TPP to controllably incorporate embedded defects within self-assembled photonic crystals has extended their viability for PBG-based applications.

Following the initial proof-of-principle demonstration, additional work was performed to improve the reliability of this process. To this end, TPP response diagrams were developed for the modulated beam rastering setup used in this work. These diagrams enabled the visualization of the polymerization and damage thresholds, enabling the reliable definition of high-resolution, damage-free features. TPP response diagrams were also used to determine that AF-350 was an efficient initiator for TPP and that the TPP response for operation within and outside of a colloidal crystal was similar. Further, electron microscopy confirmed that TPP within and outside of a colloidal crystal also afforded similar feature resolution. Also, preliminary work writing TPP features in 3D holographic photonic crystals was presented, although further development is necessary to better match the exposure doses of the TPP and holography, as well as to combat shrinkage of the photoresist upon development.

Another requirement for applications requiring a complete PBG is a high refractive index contrast between the alternating, periodic domains of the PBG material. As assembled, colloidal

photonic crystals do not satisfy this condition and thus are typically used as templates which are infiltrated with a high index material, like silicon. After removing the silica colloidal crystal template, the final silicon-air inverse FCC structure has the ability to exhibit a complete PBG. Therefore, it was also important to replicate the self-assembled photonic crystals with embedded TPP features in silicon. The TPP features and colloidal crystal served as a template for the final structure, a silicon-air inverse opal with embedded air defects. Embedded planar defects in silicon colloidal photonic crystals were optically characterized and high resolution embedded air defects in silicon-air inverse opals were demonstrated, representing a major step forward in providing a platform for the utility of colloidal photonic crystals for PBG-based applications.

APPENDIX A

BRAGG DIFFRACTION

The optical diffraction wavelength for low-index contrast photonic crystals can often be approximated well using Bragg's law

$$m\lambda_2 = 2d_{hkl} \sin \theta_2 \quad (1)$$

where m is the diffracted order, λ_2 is the wavelength of light in the photonic crystal that is diffracted, d_{hkl} is the spacing between the planes giving rise to the diffraction, θ_2 is the angle within the photonic crystal between the propagating light and the diffracting planes (Fig. 1).

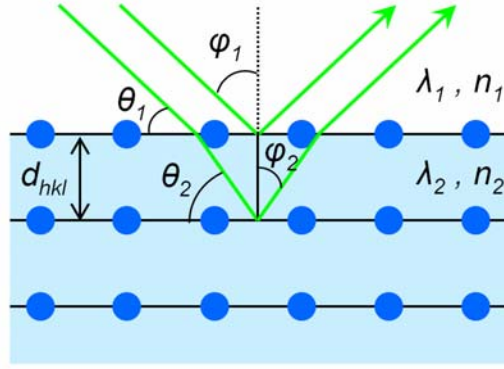


Figure 1. Schematic diagram of Bragg diffraction for low index contrast photonic crystals.

It is convenient to re-express this in terms of the angle and wavelength of incident light in free space, θ_1 and λ_1 , respectively. As the photonic crystals community typically writes Bragg's law in terms of φ_1 instead of θ_1 , we will use $\sin \theta_2 = \cos \varphi_2$ to rewrite equation 1 as

$$m\lambda_2 = 2d \cos \varphi_2 \quad (2)$$

We can then use $v = \nu_2 = \frac{c}{\lambda_1 n_1} = \frac{c}{\lambda_2 n_2}$ to substitute for λ_2 , where ν and n are the frequency and refractive index, respectively, giving

$$m\lambda_1 n_1 = 2d n_2 \cos \varphi_2 \quad (3)$$

The trigonometric identity, $\sin^2 \varphi_2 + \cos^2 \varphi_2 = 1$, then gives

$$m\lambda_1 n_1 = 2d_{hkl} n_1 \left(1 - \sin^2 \varphi_2\right)^{1/2} \quad (4)$$

and Snell's law, $n_1 \sin \varphi_1 = n_2 \sin \varphi_2$, can be used to replace the internal angle, φ_2 , with the more convenient incident angle in free space, φ_1

$$m\lambda_1 n_1 = 2d(n_2^2 - n_1^2 \sin^2 \varphi_1)^{1/2} \quad (5)$$

The first medium is typically air ($n_1=1$), while the second material is a photonic crystal whose effective refractive index is often expressed as the square root of the average dielectric constant, n_{eff} ,

$$n_2 = n_{eff} = \left[\sum_i (n_i^2 \Phi_i) \right]^{1/2} \quad (6)$$

where n_i and Φ_i are the refractive index and volume fraction for each component, i , of the photonic crystal, respectively. This yields the expression for Bragg's law typically applied to low-index contrast photonic crystals

$$m\lambda_1 = 2d_{hkl} \left(n_{eff}^2 - \sin^2 \varphi_1\right)^{1/2} \quad (7)$$

APPENDIX B

POLYMERIZATION THRESHOLD

Significant components of this appendix were published as the supplementary information section for S. A. Pruzinsky, P. V. Braun, “Fabrication and Characterization of Two-Photon Polymerized Features in Colloidal Crystals” *Advanced Functional Materials* **2005**, *15*, 1995-2004.

We begin with the same initial expression as Martineau *et al.*[1] for the absorbed energy density, E_{abs} [J cm⁻³] as a function of the lateral radial distance, r , from the center of the focal point

$$E_{abs}(r) = n_{pulses} N_i \frac{\sigma_{TPA}}{\hbar\omega} \int_{pulse} I^2(r,t) dt \quad (1)$$

where n_{pulses} is the number of laser pulses during the exposure, N_i is the number density of the initiator [cm⁻³], σ_{TPA} is the two-photon cross section of the initiator [cm⁴ s photon⁻¹], $\hbar\omega$ is the energy per photon [J photon⁻¹], and $I(r,t)$ is the local intensity [W cm⁻²]. The equation can alternatively be expressed

$$E_{abs}(r) = \tau_{exp} N_i \frac{\sigma_{TPA}}{\hbar\omega} \langle I^2(r,t) \rangle \quad (2)$$

where τ_{exp} is the exposure time [s] and $\langle I^2(r,t) \rangle$ is the time-averaged value of the local intensity squared [W² cm⁻⁴].

The intensity distribution can be approximated as a Gaussian in order to yield an expression for the absorbed energy density as a function of lateral radial distance, r , from the center of the focal point

$$I(r,t) = I_0(t)e^{-2r^2/\omega_0^2} \quad (3)$$

It is convenient to write an expression for the power, $P(t)$ [W]

$$P(t) = \int_{-\infty}^{\infty} \int_{-\infty}^{\infty} I_0(t)e^{-2(x^2+y^2)/\omega_0^2} dx dy = \frac{\pi}{2} \omega_0^2 I_0(t) \quad (4)$$

The combination of equations 3 and 4 is averaged over time

$$\langle I(r,t) \rangle = \frac{2}{\pi \omega_0^2} \langle P(t) \rangle e^{-2r^2/\omega_0^2} \quad (5)$$

where $\langle P(t) \rangle$ and $\langle I(r,t) \rangle$ are the time-averaged power and local intensity, respectively. The dimensionless second-order temporal coherence, g , is employed to interrelate square of the time-averaged local intensity, $\langle I(r,t) \rangle^2$ and the time-averaged local intensity squared, $\langle I^2(r,t) \rangle$ [2]

$$g = \frac{\langle I^2(r,t) \rangle}{\langle I(r,t) \rangle^2} = \frac{g_p}{\tau_p F} \quad (6)$$

where τ_p is the pulsewidth [s], F is the repetition rate of the laser [s^{-1}], and g_p is a dimensionless quantity which, for a hyperbolic secant squared pulse shape, equals 0.588.[2] The second order temporal coherence is used to re-express equation 2

$$E_{abs}(r) = \tau_{exp} N_i \frac{\sigma_{TPA}}{\hbar \omega} \frac{g_p}{\tau_p F} \langle I(r,t) \rangle^2 \quad (7)$$

Equations 5 and 7 are combined to yield

$$E_{abs}(r) = \tau_{exp} N_i \frac{\sigma_{TPA}}{\hbar \omega} \frac{g_p}{\tau_p F} \frac{4}{\pi^2 \omega_0^4} \langle P(t) \rangle^2 e^{-4r^2/\omega_0^2} \quad (8)$$

The outer surface of a polymerized voxel represents those points for which the total energy density absorbed at the end of the exposure was at the threshold value. Therefore since the threshold energy density, E_{th} , defines the feature width, W , it can be written

$$E_{th} = \tau_{\text{exp}} N_i \frac{\sigma_{TPA}}{\hbar \omega} \frac{g_p}{\tau_p F} \frac{4}{\pi^2 \omega_0^4} \langle P(t) \rangle^2 e^{-W^2/\omega_0^2} \quad (9)$$

The surface where $E_{abs}(r)=E_{th}$ increases in radial distance from the center of the focal point with either increasing incident average power or exposure time. By solving the equation for an infinitesimally small feature ($W = 0$), one can determine the minimum exposure time or minimum power needed to create polymer. In this work, we used a fixed exposure time (1 ms) controlled by an electronic shutter and we adjusted the average power by varying the gain on an electro-optic modulator, so we will solve for $\langle P(t) \rangle_{\text{min}}$, the minimum average power

$$\langle P(t) \rangle_{\text{min}} = \sqrt{\frac{1}{\tau_{\text{exp}} N_i} \frac{\hbar \omega}{\sigma_{TPA}} \frac{\pi^2 \omega_0^4}{4} \frac{\tau_p F}{g_p} E_{th}} \quad (10)$$

By interrelating equations 9 and 10, we can write an expression for the feature width in terms of its corresponding average power and the minimum power required to yield an infinitesimally small feature

$$W = \omega_0 \sqrt{2 \ln \left(\frac{\langle P(t) \rangle}{\langle P(t) \rangle_{\text{min}}} \right)} \quad (11)$$

From fitting a plot of feature width versus incident average power with equation 11, $\langle P(t) \rangle_{\text{min}}$ and ω_0 were determined to be 9.1 mW and 393 nm, respectively. The absorbed energy density for the polymerization threshold, E_{th} , was then calculated to be 3.07 nJ μm^{-3} using equation 12 (a re-arranged form of equation 10)

$$E_{th} = \tau_{\text{exp}} N_i \frac{\sigma_{TPA}}{\hbar \omega} \frac{4}{\pi^2 \omega_0^4} \frac{g_p}{\tau_p F} \langle P(t) \rangle_{\text{min}}^2 \quad (12)$$

These equations assume that the initiator concentration remains constant with time. The validity of this assumption requires that the excited state lifetime for our two-photon sensitive initiator, AF-350, (1.5 ns in THF) is less than the time between pulses (~12 ns) and that AF-350

is highly stable in solution and essentially does not photobleach.[3] Further, it is assumed that the exposure time (1 ms) is significantly less than the radical lifetime (cited at 0.1 to 10 s for typical free radical polymerizations).[4] This typical radical lifetime is sufficiently long to allow radicals generated within the exposed region to diffuse out, however it is assumed that there is enough oxygen in the surrounding unexposed regions these radicals will be quenched. Also, since the oxygen from the surrounding unexposed region can diffuse throughout the entire exposed volume within this time, this should have a uniform impact throughout the voxel and will be included in the observed polymerization threshold. These assumptions appear to be acceptable[1] for use with the point-by-point two-photon polymerization of isolated voxels.

References

1. C. Martineau, G. Lemerrier, C. Andraud, I. Wang, M. Bouriau, P. L. Baldeck, *Synthetic Met.* **2003**, *138*, 353.
2. C. Xu, W. W. Webb, *J. Opt. Soc. Am. B* **1996**, *13*, 481.
3. G. S. He, J. Swiatkiewicz, Y. Jiang, P. N. Prasad, B. A. Reinhardt, L. S. Tan, R. Kannan, *J. Phys. Chem. A* **2000**, *104*, 4805.
4. G. Odian, *Principles of Polymerization, Third Edition*; John Wiley & Sons, Inc.: New York, NY, **1991**.

AUTHOR'S BIOGRAPHY

Stephanie Pruzinsky was born on December 3, 1979 in Westerly, Rhode Island. She graduated from Rensselaer Polytechnic Institute with a B.S. in Materials Science and Engineering. As an undergraduate, she participated in two National Science Foundation summer research programs studying diblock copolymers and self-assembled monolayers at the University of Massachusetts at Amherst and Stanford University, respectively. She has pursued a Ph.D. in Materials Science and Engineering at the University of Illinois at Urbana-Champaign as a National Science Foundation graduate fellow under the supervision of Professor Paul Braun. Upon completion of her degree, Stephanie will begin a postdoctoral fellowship at the Beckman Institute for Advanced Science and Technology at the University of Illinois at Urbana-Champaign, where she will work in the area of biomedical imaging.